Nucleome programming for the foundation of totipotency in mammalian germline development

Masahiro Nagano[1,2,18], Bo Hu[2,3,18], Shihori Yokobayashi[1,2,4], Akitoshi Yamamura[1,2], Fumiya Umemura[1,2], Mariel Coradin[5,6,7], Hiroshi Ohta[1,2], Yukihiro Yabuta[1,2], Yukiko Ishikura[1,2], Ikuhiro Okamoto[1,2], Hiroki Ikeda[4,8,], Naofumi Kawahira[9,10], Yoshiaki Nosaka[1,2], Sakura Shimizu[1,2], Yoji Kojima[1,2,4], Ken Mizuta[1,2], Tomoko Kasahara[1,11], Yusuke Imoto[1], Killian Meehan[1], Roman Stocsits[12], Gordana Wutz[12], Yasuaki Hiraoka[1], Yasuhiro Murakawa[1,11], Takuya Yamamoto[1,4,13], Kikue Tachibana[14,15], Jan-Michel Peters[12], Leonid A Mirny[16], Benjamin A. Garcia[5,6,17], Jacek Majewski[3], Mitinori Saitou[1,2,4]

[1]Institute for the Advanced Study of Human Biology (WPI-ASHBi), [2]Department of Anatomy and Cell Biology, Graduate School of Medicine, Kyoto University, Yoshida-Konoe-cho, Sakyo-ku, Kyoto 606-8501, Japan.
[3]Department of Human Genetics, McGill University, Montreal, Quebec, Canada.
[4]Center for iPS Cell Research and Application (CiRA), Kyoto University, 53 Kawahara-cho, Shogoin, Sakyo-ku, Kyoto 606-8507, Japan.
[5]Department of Biochemistry and Biophysics, [6]Penn Epigenetics Institute, Perelman School of Medicine, University of Pennsylvania, Philadelphia, PA, USA.
[7]Department of Molecular, Cellular, and Developmental Biology, University of Colorado Boulder, Boulder, CO 80309, USA.
[8]Department of Embryology, Nara Medical University, Nara, Japan.
[9]Department of Molecular Cell Developmental Biology, School of Life Science, University of California, Los Angeles, CA, USA.
[10]Laboratory for Developmental Morphogeometry, RIKEN Center for Biosystems Dynamics Research, Kobe, Japan.
[11]RIKEN Center for Integrative Medical Sciences, Yokohama, Kanagawa 230-0045, Japan.
[12]Research Institute of Molecular Pathology, Vienna BioCenter, Vienna, Austria.
[13]Medical-risk Avoidance based on iPS Cells Team, RIKEN Center for Advanced Intelligence Project, Kyoto, Japan.
[14]Institute of Molecular Biotechnology of the Austrian Academy of Sciences, Vienna BioCenter, Vienna, Austria.
[15]Department of Totipotency, Max Planck Institute of Biochemistry, Martinsried, Germany.
[16]Institute for Medical Engineering and Science, and Department of Physics, Massachusetts Institute of Technology, Cambridge, MA, USA.
[17]Department of Biochemistry and Molecular Biophysics, Washington University School of Medicine, 660 S. Euclid Ave., St. Louis, MO 63110-1010, USA.
[18]These authors contributed equally.

Running title: Nucleome Programming for Germ Cells
Key words: germ cells; 3D genome organization; nucleome; epigenetic reprogramming; lamina-associated domains

**Correspondence:* Mitinori Saitou, M.D., Ph.D.
E-mail: saitou@anat2.med.kyoto-u.ac.jp; Tel: +81-75-753-4335; Fax: +81-75-751-7286

ABSTRACT

Germ cells are unique in engendering totipotency, yet the mechanisms underlying this capacity remain elusive. Here, we perform comprehensive and in-depth nucleome analysis of mouse germ-cell development *in vitro*, encompassing pluripotent precursors, primordial germ cells (PGCs) before and after epigenetic reprogramming, and spermatogonia/spermatogonial stem cells (SSCs). Although epigenetic reprogramming, including genome-wide DNA de-methylation, creates broadly open chromatin with abundant enhancer-like signatures, the augmented chromatin insulation safeguards transcriptional fidelity. These insulatory constraints are then erased en masse for spermatogonial development. Notably, despite distinguishing epigenetic programming, including global DNA re-methylation, the PGCs-to-spermatogonia/SSCs development entails further euchromatization. This accompanies substantial erasure of lamina-associated domains (LADs), generating spermatogonia/SSCs with minimal peripheral attachment of chromatin except for pericentromeres—an architecture conserved in primates. Accordingly, faulty nucleome maturation, including persistent insulation and improper euchromatization, leads to impaired spermatogenic potential. Given that PGCs after epigenetic reprogramming serve as oogenic progenitors as well, our findings elucidate a principle for the nucleome programming that creates gametogenic progenitors in both sexes, defining a basis for nuclear totipotency.

INTRODUCTION

Germ cells are the origin of totipotency, which in turn is the foundation for individual development. Mechanisms underlying totipotency have been a focus of intensive investigations, ranging from studies involving somatic-cell nuclear transfer (Gurdon & Wilmut, 2011) to recent efforts exploring the three-dimensional (3D) chromatin organization in zygotes and early embryos (Zheng & Xie, 2019). The latter works involving chromatin conformation capture have revealed a relaxed chromatin configuration in zygotes in part resulting from unique meiotic intermediates, and the progressive maturation of this configuration in early embryos (Alavattam *et al*, 2019; Battulin *et al*, 2015; Du *et al*, 2017; Flyamer *et al*, 2017; Ke *et al*, 2017; Patel *et al*, 2019; Vara *et al*, 2019; Wang *et al*, 2019). On the other hand, the manner by which germ cells elaborate the higher-order chromatin organization during their mitotic development, and the founding states for gametogenesis and totipotency, remain poorly understood. In-depth understanding of genome functions requires investigations of the 3D genome organization complemented by thorough epigenome and transcriptome profiling, an approach known as "nucleome" profiling (Dekker *et al*, 2017). While nucleome profiling has been performed in a few somatic lineages (Bonev *et al*, 2017; Stadhouders *et al*, 2018; Zhang *et al*, 2019), studies applying this approach to germ-cell development are lacking.

In mammals, germ cells arise as primordial germ cells (PGCs) during early embryonic development (Saitou & Hayashi, 2021). PGCs undergo migration and colonize the embryonic gonads, where they differentiate either into spermatogonia/spermatogonial stem cells (SSCs), the source for spermatogenesis, or oocytes with an immediate entry into the first prophase of meiosis (Griswold, 2016; Spiller *et al*, 2017; Wen & Tang, 2019). A key event that characterizes PGCs is epigenetic reprogramming, including de-methylation of genome-wide DNA to the point that it contains almost no DNA methylation, as well as histone-modification remodeling, which creates a facultative "naïve" epigenome (Lee *et al*, 2014; Tang *et al*, 2016). In males, epigenetic reprogramming is followed by the provision of a distinct spermatogenic epigenome, including global DNA re-methylation, for spermatogonia/SSC development, whereas in females, the naïve epigenome serves as a direct precursor for the oogenic meiotic entry (Lee *et al.*, 2014). Thus, male germ-cell development requires at least one additional epigenetic programming step to create spermatogenic progenitors. Here, to explore the principles that create a basis for gametogenic potential, we performed nucleome profiling of an *in vitro* system that faithfully reconstitutes mouse germ-cell development from pluripotent precursors to PGCs before and after epigenetic reprogramming and then to spermatogonia/SSCs (Hayashi *et al*, 2011; Kanatsu-Shinohara *et al*, 2003; Ohta *et al*, 2017; Ohta *et al*, 2021). We show that the *in vitro* system recapitulates not only gene-expression and epigenetic properties, but also 3D genome-organization dynamics

during germ-cell development *in vivo*, lending credence to our analyses using scalable materials to provide a more complete picture of nucleome dynamics with high resolution during germ-cell development. In addition, to delineate the functional significance of appropriate nucleome programming, we analyzed the nucleome of an *in vitro* counterpart of spermatogonia/SSCs with an impaired spermatogenic potential (Ishikura *et al*, 2016).

RESULTS

Mouse germ-cell development *in vitro*

We analyzed the following male cell types (Fig 1A): mouse embryonic stem cells (mESCs) derived from blastocysts (Ying *et al*, 2008), epiblast-like cells (EpiLCs) (Hayashi *et al.*, 2011), mouse PGC-like cells at day 2 of induction (d2 mPGCLCs) (Hayashi *et al.*, 2011), d4 mPGCLCs expanded *in vitro* for 7 days for epigenetic reprogramming (d4c7 mPGCLCs) (Ohta *et al.*, 2017; Ohta *et al.*, 2021), and germline stem cells (GSCs) derived from neonatal spermatogonia (Kanatsu-Shinohara *et al.*, 2003). These cells show gene-expression, epigenetic, and functional properties equivalent to those of their *in vivo* counterparts, i.e., mESCs to epiblast at embryonic day (E) 4.5 with naïve pluripotency (Boroviak *et al*, 2014; Marks *et al*, 2012), EpiLCs to epiblast at ~E6.0 with formative pluripotency (Hayashi *et al.*, 2011), d2 mPGCLCs to mPGCs during their specification at ~E7.0 and before epigenetic reprogramming (Hayashi *et al.*, 2011; Kurimoto *et al*, 2015), d4c7 mPGCLCs to PGCs at E11.5 after epigenetic reprogramming (Ohta *et al.*, 2017; Ohta *et al.*, 2021), and GSCs to spermatogonia/SSCs (Ishikura *et al.*, 2016). Note that PGCs before E11.5 do not show overt sexual differences in gene-expression and epigenetic properties, except X-chromosome reactivation in females (Jameson *et al*, 2012; Ohta *et al.*, 2017). Accordingly, male PGCs bear a capacity to form functional oocytes (Evans *et al*, 1977), and male mPGCLCs take on the oogenic fate and enter into the meiotic prophase in response to appropriate signals at an efficiency comparable to that of female mPGCLCs (Miyauchi *et al*, 2017; Nagaoka *et al*, 2020). Thus, while our present analysis focuses on male germ-cell development, male d4c7 mPGCLCs can be considered to bear an oogenic potential as well. In addition, to evaluate the functional relevance of proper nucleome programming, we analyzed GSC-like cells (GSCLCs) that were derived from d4 mPGCLCs *in vitro* and had an impaired spermatogenic potential (Ishikura *et al.*, 2016) (see the "**Nucleome programming engenders gametogenic potential**" section).

Higher-order genome organization: maturation towards a highly euchromatized state

We first examined the nuclear morphology of the five cell types (mESCs, EpiLCs, d2 mPGCLCs, d4c7 mPGCLCs, and GSCs) stained with DAPI (4',6-diamidino-2-phenylindole) using high-resolution confocal microscopy. Counterintuitive to GSCs' acquisition of a distinct spermatogenic epigenome, including global DNA re-methylation, on the epigenome of naïve PGCs, the areas of high DAPI density (peri-centromeric heterochromatin) (Guenatri *et al*, 2004), the variances of DAPI density (chromatin condensation heterogeneity), and the distances of the DAPI-dense areas from the nuclear periphery (chromosome radial positioning), all exhibited a monotonically decreasing transformation towards GSCs (Fig 1B and C). This indicates that chromatin de-condensation (i.e., euchromatization), as well as

peripheral tethering of centromeres, proceeds progressively beyond the canonical epigenetic reprogramming period. Notably, formative EpiLCs showed more discrete chromatin condensation than naïve mESCs, while mESCs and d4c7 mPGCLCs (latent pluripotency) (Surani *et al*, 2007) exhibited significant differences in chromosome radial positioning (Fig 1B and C). Fluorescence in situ hybridization (FISH) confirmed that, in line with chromatin de-condensation, GSCs bore larger chromosome volumes than mESCs and EpiLCs (Fig 1D, Fig EV1A).

We next analyzed the five cell types by *in situ* Hi-C (~5 kb resolution) with reproducible biological replicates (Fig EV1B, Dataset EV1). Consistent with the morphological observations, 3D genome organization was transformed in an unidirectional manner during germ-cell development: the chromosomal contact profile shifted progressively from the conventional proximal contact-enriched state to a more uniform profile with heightened distal interactions (Fig 1E, Fig EV1C, Appendix Fig S1A), and the compartment score distributions and euchromatin-to-heterochromatin balance exhibited a monotonical increase (Fig 1G, Fig EV1D). Notably, while the vast majority (~33.3% genome-wide) of the A compartment in mESCs remained an A compartment, more than one third (~38.9% genome-wide) of the B compartment in mESCs progressively turned into A, with the largest B-compartment fraction (~7.5% genome-wide) turning into A upon the d4c7 mPGCLC-to-GSC transition. In stark contrast, the compartment scores exhibited a gradual decrease during somatic development, including neuronal, B-cell, and cardiomyocyte differentiation (Fig 1G, Appendix Fig S1B) (Bonev *et al.*, 2017; Stadhouders *et al.*, 2018; Zhang *et al.*, 2019). The brief decrease in the compartment score upon EpiLCs-to-d2 mPGCLCs differentiation (Fig 1G) is consistent with the transient activation of a somatic program during mPGCLC specification (Kurimoto *et al.*, 2015). Accordingly, principal component analysis (PCA) of the compartment scores segregated the germline from somatic development (Appendix Fig S1C). Along with the expansion of the A compartment (Fig 1G, Fig EV1D), euchromatic A-A interactions became less intense, while the reduced B compartment exhibited stronger B-B interactions both within (cis) and between (trans) chromosomes, implying the formation of repressive condensates (Fig 1F).

On a smaller scale, topologically associating domain (TAD) boundaries exhibited a substantial overlap during germ-cell development, with the degree of their conservation being similar to that of somatic lineages (Fig EV1E and F, Appendix Fig S1D). However, inter-TAD interactions involving the simultaneous aggregations of multiple non-neighboring TADs, referred to as “TAD-cliques” (Paulsen *et al*, 2019), became dramatically less prevalent in the A compartments, while they were over-represented in the B compartments in both d4c7 mPGCLCs and GSCs, which was in stark contrast to their opposite/relatively stable behaviors in somatic lineages (Fig 1H and I, Appendix

Fig S1E). Through polymer simulations, we generated representative 3D structures of whole chromosomes (Todd *et al*, 2021), which similarly demonstrated the progressive expansion of chromosome volume during germ-cell development (Fig EV1G, Appendix Fig S1F, Movie EV1).

To examine whether the five cell types recapitulate their *in vivo* counterparts at the 3D genome organization level, we retrieved published Hi-C data of the inner cell mass at ~E4.0, epiblast at E6.5, PGCs at E11.5, and spermatogonia in adults, which were generated from small numbers of samples (Du *et al.*, 2017; Du *et al*, 2020; Luo *et al*, 2020). Remarkably, not only at the transcriptomic and epigenomic level that we reported previously (Hayashi *et al.*, 2011; Ishikura *et al.*, 2016; Ohta *et al.*, 2017), the *in vitro* cell types exhibited a strong concordance with their *in vivo* counterparts at the 3D genome organization level (Fig EV1C and E) (despite the elevated noise of contact matrices from *in vivo* samples), with unsupervised hierarchical clustering (UHC) and PCA using compartment scores consistently placing corresponding cell types next to one another (Fig EV1H and I). Thus, the *in vitro* system faithfully captures the nucleome dynamics of *in vivo* germ-cell development, further empowering our strategy for using scalable *in vitro* materials to delineate a more complete picture of nucleome dynamics during germ-cell development. We conclude that, beyond the canonical epigenetic reprogramming period, higher-order genome organization undergoes a continuous maturation and culminates in a largely euchromatic genome and peripherally positioned centromeres in spermatogonia/SSCs (GSCs). Thus, global DNA methylation and euchromatization are separable events. Moreover, our findings revealed that, despite their profound epigenomic differences, PGCs (d4c7 mPGCLCs) with both oogenic and spermatogenic potential and spermatogonia/SSCs (GSCs) show relatively similar higher-order genome organization.

Epigenome profiling: epigenetic reprogramming for highly open chromatin with enhanced insulation

To explore the mechanism underlying the higher-order genome organization unique to the germ line, we conducted comprehensive epigenome profiling of the five cell types. We performed mass spectrometry (MS) of histones; chromatin immunoprecipitation followed by deep sequencing (ChIP-seq) of 13 different targets, including 9 histone modifications; assay for transposase-accessible chromatin with deep sequencing (ATAC-seq) for open chromatin; and native elongating transcript–cap analysis of gene expression (NET-CAGE) for transcribed *cis* regulatory elements (Dataset EV1). For some assays, we analyzed d4 mPGCLCs, which are in the middle of epigenetic reprogramming, as an intermediate between d2 and d4c7 mPGCLCs and mouse embryonic fibroblasts (MEFs) as a somatic control.

MS revealed dynamic changes in histone-modification levels with high reproducibility

(Fig 2A, Dataset EV2). Consistent with previous observations (Kurimoto *et al.*, 2015; Ohta *et al.*, 2017), histone H3 lysine 9 di-methylation (H3K9me2) was substantially reduced and H3K27 tri-methylation (H3K27me3) was strongly up-regulated in d4c7 mPGCLCs (Fig 2A, Fig EV2A and B). With respect to active modifications, H3K27 acetylation (H3K27ac: active cis-regulatory elements) and H3K18ac were the most abundant in EpiLCs, whereas H3K4 mono-methylation (H3K4me1: poised enhancers), H3K14ac, and H3K23ac were the most adundant in d4c7 mPGCLCs, and, interestingly, H3K4me3 (promoters) was the least prevalent in d4c7 mPGCLCs (Fig 2A). UHC based on H3-modification abundance segregated each cell type with their unique sets of associated H3 modifications (Fig 2B), and PCA demonstrated characteristic transitions of epigenetic properties, with the transition from d2 to d4c7 mPGCLCs representing the epigenetic reprogramming to a latent pluripotency and the transition from d4c7 mPGCLCs to GSCs signifying the acquisition of a spermatogenetic epigenome (Fig 2C). We proceeded to normalize all histone modification ChIP-seq signals with MS-based scaling factors for subsequent analyses (Fig EV2C and D) (Farhangdoost *et al*, 2021).

We first scrutinized the open-chromatin landscape. Consistent with d4c7 mPGCLCs being globally DNA demethylated (~5%) (Fig 1A) (Ohta *et al.*, 2017; Ohta *et al.*, 2021), they exhibited a pervasively open chromatin with coincident up-regulation of H3K4me1, bearing large open domains in a genome-wide manner (Fig 2D and E). Indeed, among a diverse panel of mouse fetal tissues (Gorkin *et al*, 2020), d4c7 mPGCLCs showed the highest degree of openness (Fig EV2E). Consistent with the analysis of the abundance of H3 modifications (Fig 2C), PCA with the most variable open sites (Fig EV2F) and UHC revealed that d4c7 mPGCLCs share open sites for pluripotency with mESCs and those for germ-cell identity with GSCs: the former (clusters 1, 2, 4) being enriched in transcription-factor (TF)-binding sites for POU5F1, NANOG, SOX2, ZIC2/3, and KLF3/12, and the latter (clusters 3, 7) in those for DMRTs (Fig EV2G, Dataset EV3).

Despite their genome-wide DNA demethylation, PGCs and d4c7 mPGCLCs do not exhibit transcriptional hyperactivity or promiscuousness (Ohta *et al.*, 2017; Ohta *et al.*, 2021; Seisenberger *et al*, 2012). To explore higher-order regulatory mechanisms, we identified enhancer-promoter (E-P) pairs using the activity-by-contact model by integrating ATAC-seq, H3K27ac, and Hi-C data (Fig EV3A) (Fulco *et al*, 2019). Notably, d4c7 mPGCLCs showed a reduced number and range of active E-P pairs as compared to the other cell types (Fig 2F, Fig EV3B). Furthermore, NET-CAGE revealed an under-representation of E-P co-transcription in d4c7 mPGCLCs (Fig EV3C). d4c7 mPGCLCs were also predicted to bear the largest numbers of insulating TAD boundaries (Fig 2G and Fig EV3D), showed the smallest genomic separation (Fig 2H) and exhibited the broadest compartment profile (Fig EV3E), in agreement with the notion that heightened insulation can mask smaller compartments (Schwarzer *et al*, 2017). While CTCF and RAD21, a key component of cohesin, exhibited comparable

enrichment at TAD boundaries across the five cell types (Fig EV3F) (we discuss the CTCF depletion in GSCs below), ATAC-seq revealed that d4c7 mPGCLCs uniquely exhibited lower chromatin information content around regions with co-localized CTCF/RAD21 bindings (Fig EV3G), suggesting that d4c7 mPGCLCs bore a shorter CTCF/RAD21 residence time (D'Oliveira Albanus *et al*, 2021). Taken together, these findings support the idea that, due to a reduced residence time of the loop extrusion machinery with no major changes in global binding sites, d4c7 mPGCLCs bear shorter chromatin loops and enhanced insulation (Fig EV3H and I). Additionally, E13.5 male PGCs *in vivo* also demonstrate similarly enhanced insulation (Fig EV3J and K). We conclude that PGCs with a naïve epigenome bear a highly open chromatin, but undergo enhanced insulation to ensure their transcriptional integrity.

Insulation erasure for spermatogonia development and oogenesis

We next classified ATAC-seq peaks (open sites) based on their combinatorial epigenetic states. Building on the Ensembl Regulatory Build and ENCODE's registry of candidate Cis-Regulatory Elements (cCREs), we applied uniform manifold approximation and projection (UMAP) in combination with hierarchical density-based spatial clustering of applications with noise (HDBSCAN) in a semi-supervised manner through iterative sub-clustering (Tables EV4 and EV5). This framework classified the open sites into 19 distinct sets (Fig 3A), which we grouped into 6 broader categories (Fig 3B, Fig EV4A). While d4c7 mPGCLCs showed the largest number of enhancer elements (clusters 5, 6, 15, 18) (Fig 3B and C), GSCs exhibited a relatively large number (~ >10,000) of non-promoter bivalent open sites (clusters 8, 9, 10, 13). Additionally, we uncovered a set of open sites with unique trivalency of H3K4me3, H3K27ac and H3K9me3 that were enriched in EpiLCs (cluster 19) (Fig 3B) and overlapped not only with the promoter of long interspersed nuclear elements 1 (LINE1) but also with the binding site of YY1 (Fig EV4B, Dataset EV5), underscoring the capacity of our epigenetic compendium for uncovering biologically distinct regulatory regions. A vast majority of enhancers were cell-type specific, whereas most CTCF bindings were conserved upon each cell-fate transition until d4c7 mPGCLCs; strikingly, however, a majority of CTCF-bound sites in d4c7 mPGCLCs were lost in GSCs (Fig 3C) (see below).

We performed the same analyses for promoters (Fig EV4D-F, Dataset EV4). In accord with our previous finding (Kurimoto *et al.*, 2015), EpiLCs bore the largest number of bivalent promoters (Fig EV4F). Evaluation of the promoter-promoter (P-P) interactions revealed that active as well as bivalent promoters exhibited significantly enriched interactions in all cell types, but to lesser extents in d4c7 mPGCLCs bearing elevated insulation (Fig 2G, Fig EV4G).

We next explored the depletion of CTCF binding upon d4c7 mPGCLCs-to-GSCs

transition (Fig 3C). In GSCs, decreased CTCF protein expression accompanied a dramatic reduction in the number of CTCF peaks (Fig 3D-F). In particular, CTCF was depleted from relatively weak binding sites (Fig 3E and F). These CTCF-depleted sites exhibited elevated DNA methylation as well as enrichment of H3K9me2/me3 and H3K36me2/me3, whereas CTCF peaks enriched in GSCs showed divergent patterns (Fig 3G, Fig EV4H). Importantly, despite relatively weak bindings, CTCF depletion from such sites resulted in a reduction in insulation (Fig 3G), leading to a rewiring of neighboring cis-regulatory interactions as exemplified for *Ddx4*, a key gene up-regulated upon d4c7 mPGCLCs-to-GSCs transition, whose promoter strengthened its long-range interaction with a distal enhancer (Fig 3H, Fig EV4I). We then systematically identified E-P pairs straddling CTCF sites depleted in GSCs and ranked the target genes according to coordinated expression up-regulation and increased E-P interactions (Fig EV4J). Genes with coordinated activation were enriched in gene ontology (GO) functional terms such as "homologous chromosome pairing at meiosis," and "piRNA metabolic process," and included *Ddx4*, *Mael*, *Piwil2*, *Piwil4*, *Zbtb16*, *Sycp1*, *Syce3*, *Mei4*, and *Prdm9* (Fig 3I, Dataset EV6) [these genes are referred to as "germline genes" (Borgel *et al*, 2010) ; also, see below], indicating a critical role of the insulation erasure in spermatogonia development and the acquisition of meiotic competence.

To explore whether insulation erasure may also occur upon oogenesis, we re-analyzed published Hi-C data for E11.5 PGCs (d4c7 mPGCLC counterparts) and E13.5 germ cells initiating their male or female differentiation (Du *et al.*, 2017; Du *et al.*, 2020). We found that a majority of E13.5 male germ cells were still in the mitotic phase and bear similar properties to E11.5 PGCs, whereas most E13.5 female germ cells were in the leptotene stage of the meiotic prophase (Nagaoka *et al.*, 2020; Western *et al*, 2008). Consistent with our comprehensive analyses (Fig 2 and 3), the point of fastest decline in the chromosomal cis-contact decay rate, an index for TAD width (Polovnikov *et al*, 2022), occurred at the smallest genomic separation in E11.5 PGCs and d4c7 mPGCLCs (Fig 2H, Fig EV3J and K), suggesting that, similar to d4c7 mPGCLCs, E11.5 PGCs bear enhanced insulation. Notably, while the fastest point of decline of E13.5 male germ cells was in a range comparable to E11.5 PGCs and d4c7 mPGCLCs, that in E13.5 female germ cells occurred at a much longer distance, suggesting a rapid weakening of insulation upon the initiation of oogenesis. We conclude that insulation erasure occurs both for spermatogonia development and oogenesis, with the latter having an earlier onset.

Mechanism for euchromatization: dynamics of LADs, pericentromeric heterochromatin, and H3K9 methylation

We next explored potential mechanisms for the progressive euchromatization unique to germ-cell development (Fig 1G). While the five cell types exhibited relatively

conserved correlations between their compartment scores and epigenetic modification profiles, there nevertheless existed cell-type specific variations (Fig 4A). We noted that the binding profiles of lamin B1, which forms the nuclear lamina and tethers chromosomes to create lamina-associated domains (LADs) (Guelen *et al*, 2008), were the strongest predictor for compartment-score differences between mESCs and GSCs (Fig 4B), and the LADs changed dramatically with a sweeping reduction across regions that undergo euchromatinization in GSCs (Fig 4C). Consequently, among a number of other cell types (Peric-Hupkes *et al*, 2010; Poleshko *et al*, 2017; Robson *et al*, 2016; Yattah *et al*, 2020), GSCs bore the smallest genomic coverage of LADs (~10%) (Fig 4D), a vast majority of which were a subset of constitutive LADs found across all other cell types (Fig 4E and F). Indeed, GSCs exhibited low lamin B1 levels and enrichments (Fig 4G and H). Thus, GSCs constitute a cell type with minimal LADs.

While LADs were prominent toward the distal ends of long arms in mESCs and EpiLCs, they became more uniformly distributed in d2/d4c7 mPGCLCs with a reduction in their coverage in d4c7 mPGCLCs, and they eventually become depleted around the distal ends of long (q) arms in GSCs, where they were only retained towards the opposing (p/short) end, i.e., around centromeres of the telocentric mouse chromosomes (Fig 4C, I, and J). This is consistent with the progression of nuclear peripheral association of DAPI-dense areas along germ-cell development (Fig 1B and C). Accordingly, DNA FISH for major satellite repeats, a pericentromere marker, revealed that while such regions were localized mainly within the nuclear interior in EpiLCs, they were predominantly positioned around the nuclear periphery in GSCs (Fig 4L).

To explore whether the peripherally positioned centromeres and extensive euchromatization in other chromosomal regions in GSCs are a conserved feature in mouse spermatogonia *in vivo* and in other mammals such as primates, we re-analyzed relevant published datasets (Du *et al.*, 2020; Wang *et al.*, 2019). The distributions of chromosome-wide compartment-score differences between GSCs and EpiLCs were very similar to those between spermatogonia and fibroblasts in both mice and rhesus monkeys, with spermatogonia showing the lowest compartment score around centromeres and widespread euchromatization across other regions (note that rhesus monkeys bear metacentric chromosomes) (Fig EV5A and B). We conclude that higher-order genome organization in GSCs is conserved in spermatogonia *in vivo* and, through evolution, in monkeys.

As a mechanism that gives rise to the minimal LADs, we noted significant changes in the abundance and distributions of H3K9me2/me3, hallmarks of chromatin anchored to the nuclear lamina (Bian *et al*, 2013; Chen *et al*, 2014; Harr *et al*, 2015). The abundance of both H3K9me2/me3 increased progressively from mESCs to d2 mPGCLCs, and then decreased dramatically in d4c7 mPGCLCs (Fig 2A). While the

low abundance of H3K9me2 persisted in GSCs, the abundance of H3K9me3 increased in GSCs to the highest level among the five cell types (Fig 2A). The distributions of H3K9me2 were widespread across the chromosomes and well conserved among the five cell types except in d4c7 mPGCLCs, which, unlike the other cell types, retained H3K9me2 at a relatively high level around the pericentromeres (Fig 4K). On the other hand, in all cell types, H3K9me3 showed a unique and conserved distribution with a characteristic enrichment around the pericentromeres, with GSCs bearing broader/expanded H3K9me3 domains that bridge several peaks present in other cell types (Fig 4K, 5A and B). Notably, consistent with the increased B-B interactions, the broad H3K9me3 domains in GSCs exhibited elevated intra- as well as inter-domain aggregations (Fig 5C).

LADs consistently showed positive correlations with both H3K9me2/me3, except in GSCs, which had minimal LADs showing a positive correlation only with H3K9me3 (Fig 5D). IF analysis verified that GSCs showed a nuclear peripheral enrichment of H3K9me3 but not me2, while EpiLCs bore peripheral H3K9me2 but not me3 enrichment (Fig 5E). Interestingly, regions constitutively enriched with H3K9me3 across all five cell types, i.e., putative nucleation sites for H3K9me3 expansion in GSCs, were enriched with evolutionarily young transposable elements (TEs) including ERVK, ERV1 and LINE1 (Fig 5F, Fig EV5C, Dataset EV5). Accordingly, the densities of these TEs were highly predictive of the minimal LADs in GSCs (Fig 5G, Fig EV5D). Thus, minimal LADs in GSCs are the regions that show consistent attachment to the nuclear lamina across all cell types, likely contributing to the continued repression of evolutionarily young TEs and the maintenance of genome fidelity. Collectively, these results indicate that, during germ-cell development, LADs progressively remodel toward a minimal state, positionally shifting from the distal ends of long arms predominantly associated with H3K9me2 to the opposite ends of the chromosomes, the centromeres. These pericentromeric regions, with newfound peripheral attachment in GSCs, are predominantly associated with H3K9me3 and are populated with evolutionarily young TEs, enabling extensive euchromatization on the opposing chromosome arm (long/q arm).

Next, to gain insights into the mechanisms underlying H3K9 methylome dynamics, we examined the expression of major H3K9 methyltransferases (K9MTases). At the transcriptional level, *Suv39h1* and *h2*, which are responsible for the H3K9 methylation in the peri-centromeric heterochromatin and other B compartment regions (Fukuda *et al*, 2021), showed progressive up-regulation, whereas *Setdb1*, *Ehmt1* (*Glp1*), and *Ehmt2* (*G9a*), which are involved in the H3K9 methylation in both A and B compartments (Fukuda *et al.*, 2021), were gradually repressed until d4c7 mPGCLCs and then up-regulated in GSCs (Fig 5H). At the protein level, SETDB1, EHMT1 and EHMT2 were repressed until d4c7 mPGCLCs and remained at a low level in GSCs as well (we

were not able to determine the SUV39H1/H2 levels due to the lack of appropriate antibodies) (Fig 5I). These findings are consistent with the dynamics of the H3K9me2/me3 levels and distributions, suggesting that the H3K9 methylome is regulated at least in part by the differential expression of K9MTases.

Additionally, we explored the impact of the global remodeling of H3K9me3 on gene expression. In particular, we noted that during the d2-to-d4c7 mPGCLC transition, 728 promoters showed H3K9me3 down-regulation (Fig 5J), and they were enriched with GO terms such as "multi-organism reproductive process," "sexual reproduction," and "gamete generation," and included *Dazl*, *Ddx4*, *Sycp1*, *Sohlh2*, and *Mael* (Fig 5J, Table S6). These genes, which included many subject to insulation erasure upon spermatogonia development (Fig 3I and J), are referred to as "germline genes" (Borgel *et al.*, 2010), and are known to be repressed by DNA methylation in somatic cells and by H3K27me3 and H3K9me2 in mPGCLCs (Borgel *et al.*, 2010; Kurimoto *et al.*, 2015). Furthermore, a recent report has shown that the germline genes were repressed in EpiLCs with H3K9me3 imposed by *Setdb1* (Mochizuki *et al*, 2021). In good agreement, the transcriptional start sites (TSSs) of germline genes repressed by *Setdb1* up-regulated H3K9me3 in EpiLCs and, more prominently, in d2 mPGCLCs, and lost it in d4c7 mPGCLCs (Fig 5K and L). The TSSs of germline genes defined in another study (Kurimoto *et al.*, 2015) exhibited a comparable reduction of H3K9me3 during d2-to-d4c7 mPGCLC transition (Fig 5M). Thus, the germline genes are endowed with multiple layers of mechanisms, including higher-order genome organization involving the insulation by CTCF and compound repressive epigenetic modifications, to prevent their activation in somatic cells, and such mechanisms are exempted in a stepwise manner—i.e., erasure of DNA and H3K9 methylation occurs first and then release from H3K27me3/H2AK119u1 and CTCF insulation ensues—during germ-cell development.

Heterochromatin compaction excludes H3K36me2 to create PMDs and Y-chromosome hypomethylation

A unique epigenetic characteristic of male germ cells (pro-spermatogonia, spermatogonia and spermatozoa) is the presence of large partially methylated domains (PMDs) in intergenic regions (Kubo *et al*, 2015). PMDs can be defined as broad genomic domains with a comparatively lower methylation level than the rest of the genome and typically cover a substantial fraction of the genome (Lister *et al*, 2009). They were first identified in a human cultured cell line (Lister *et al.*, 2009) and subsequently found to be prevalent in cancers, aged cells, and tissues such as placenta (Hansen *et al*, 2011; Hon *et al*, 2012; Schroeder *et al*, 2013). While evidence suggests that PMDs arise from an imperfect maintenance of methylation during mitosis (Salhab *et al*, 2018), the mechanism that engenders PMDs in mitotically arrested pro-spermatogonia and their subsequent maintenance in male germ cells remains unclear.

We found that GSCs bore PMDs larger than 140 Mb in total, a majority (~86%) of which were overlapped with those in spermatogonia (Fig 6A) (Kubo *et al.*, 2015). The PMDs in GSCs consisted almost entirely of B compartments and were enriched with heterochromatic modifications such as H3K9me3, while depleted of active modifications including H3K36me2, H3K27ac and H3K4me1/3 (Appendix Fig S2). The epigenomic profiles revealed that the epigenome of d4c7 mPGCLCs exhibited the greatest predictive power for PMDs in GSCs (greater than that of the epigenome of GSCs themselves) (Fig 6B), and among individual epigenetic markers, H3K9me2/me3 and lamin B1 in d4c7 mPGCLCs were the strongest negative predictors (Fig 6C), suggesting that the constitutive heterochromatin in d4c7 mPGCLCs contributes to the subsequent formation of PMDs. Accordingly, we found that H3K36me2, which is catalyzed by NSD1 and serves as a recruiter of the androgenetic DNA methylome (Shirane *et al*, 2020), showed a specific depletion in the B compartments and the regions retaining H3K9me3, but not H3K27me3, in d4c7 mPGCLCs (Fig 6D-F), resulting in an exquisite concordance of H3K36me2 with the A compartments and a near-complete exclusion from LADs in d4c7 mPGCLCs (Fig 6G). We found that the TADs involved in larger-sized TAD cliques in d4c7 mPGCLCs exhibited the greatest H3K9me3 enrichment (Fig 6H). Given that the heterochromatic TAD-cliques become dominant in d4c7 mPGCLCs and GSCs (Fig 1H and I), these findings suggest that an increased aggregation of constitutive heterochromatin in d4c7 mPGCLCs may exclude the recruitment of NSD1 and hence the deposition of H3K36me2, leading to the formation of PMDs in GSCs.

In this regard, we noted that, as compared to the autosomes and the X chromosomes, the Y chromosomes, which bear a highly repetitive structure (Soh *et al*, 2014), were the most enriched with H3K9me3 in all five cell types, and interestingly, exhibited a progressive enrichment of lamin B1 during germ-cell development, with the Y chromosomes in GSCs showing the highest lamin B1 enrichment level (Fig 6I). In addition, we found that the Y chromosome in GSCs was hypo-methylated across almost its entire length, with ~75% of it identified as falling within PMDs—a much greater proportion than in autosomes (4%) or the X chromosome (21%) (Fig 6J, L, and M). Indeed, by alternatively mapping directly to the consensus repeat sequences of the Y chromosome, we found that all repetitive units demonstrate reduced methylation levels in GSCs as compared to EpiLCs (Appendix Fig S3A and B). Consistent with the de-condensation of chromatin in GSCs (Fig 1B-D), the Y chromosomes in GSCs exhibited loose structures and were associated with the nuclear periphery with a lower sphericity (Fig 6K), indicating greater surface contact with the nuclear lamina through chromosome elongation. Thus, the Y chromosome in GSCs achieves chromosome-wide hypomethylation likely via a convergent mechanism with PMDs in autosomes. Together, these results lead us to conclude that the unique 3D epigenomic

character of the progenitors (d4c7 mPGCLCs) serves as a blueprint for the formation of PMDs in male germ cells.

Nucleome programming engenders gametogenic potential

To delineate the functional significance of a proper nucleome for gametogenesis, we performed nucleome analyses (morphology; *in situ* Hi-C; MS; ChIP-seq for 13 targets; ATAC-seq; and NET-CAGE) of GSC-like cells (GSCLCs), which were derived from d4 mPGCLCs with their differentiation into spermatogonia-like cells in reconstituted testes followed by expansion under a GSC derivation condition (Ishikura *et al.*, 2016) (Fig 7A). GSCLCs derived under this condition bore a morphology, transcriptome, and DNA methylome similar to those of GSCs, but showed a severely impaired capacity for spermatogenesis for unclear reasons (Ishikura *et al.*, 2016) (Appendix Fig S4A). We hypothesized that aberrant nucleome programming during the derivation of GSCLCs might underlie their impaired function.

GSCLCs were similar to GSCs in terms of the areas of high DAPI density and the distances of the DAPI-dense areas from the nuclear periphery, but showed greater variances of DAPI density than GSCs (Fig 7B and C), indicating that GSCLCs bear a more heterogeneous chromatin de-condensation. *In situ* Hi-C revealed that, compared to GSCs, GSCLCs exhibited a depletion in long-range interactions, indicative of incomplete chromatin uniformalization (Fig 7D, Appendix Fig S4B), and notably, failed to acquire the positively skewed compartment score distribution characteristic of GSCs (Fig 7E). A multi-scale model dividing the genome into the eight subcompartments with distinct epigenetic properties (Liu *et al*, 2021) revealed that major difference between GSCLCs and GSCs were localized to intermediate compartments, with GSCLCs bearing fewer and more intermediate A and B sub-compartments, respectively (Fig 7F and G, Appendix Fig S4C).

Accordingly, MS revealed that GSCLCs bore an elevated level of H3K27me3 and H3K9me2, which are associated with a state intermediate between compartments A and B (Johnstone *et al*, 2020) (Fig 7H). The regions with higher H3K27me3 in GSCLCs were enriched in promoters and CpG islands (CGIs) (Appendix Fig S4D, Dataset EV6), which were, importantly, associated with pathways such as “male meiotic nuclear division,” and “recombinatorial repair,” and included *Ddx4*, *Dmrt1*, *Dmc1*, *Stag3*, and *Spo11* (Fig 7I and J, Dataset EV6). These genes bore higher levels of H3K27me3 on their gene bodies as well (Fig 7I, Appendix Fig S4E). In contrast, the regions with higher levels of H3K9me2 in GSCs were enriched in enhancers and distal active regulatory elements (Appendix Fig S4F and G), and were associated with pathways such as “response to ciliary neurotrophic factor,” “rod bipolar cell differentiation,” and “adrenal cortex formation” (Appendix Fig S4H, Dataset EV6).

Moreover, GSCLCs bore a larger number of the CTCF-binding peaks coinciding with insufficient accumulation of H3K9me3 (Fig 7K, Appendix Fig S4I and J), and indeed GSCLCs developed higher intra-TAD interaction strength compared to GSCs (Fig 7L), indicating that the chromatin of GSCLCs is more insulated than that of GSCs. In a megabase-scale domain encompassing *Ddx4*, the insulating CTCF peak separating the *Ddx4* promoter from one of its potential enhancers was removed only partially in GSCLCs, resulting in a reduced activation as evidenced by the comparatively lower H3K36me3 levels on *Ddx4* (Fig 7M). Collectively, these results lead us to conclude that GSCLCs exhibit aberrant nucleome programming, including insulation erasure and epigenome programming, with partial retention of the properties of d4c7 mPGCLCs, resulting in their impaired spermatogenic potential.

DISCUSSION

Germ-cell development lays the groundwork for nuclear totipotency, creating sexually dimorphic haploid gametes, the oocytes and the spermatozoa, which unite to form totipotent zygotes. PGCs bear naïve epigenome after epigenetic reprogramming and can serve as a direct precursor for oocyte differentiation; they can also acquire a distinct spermatogenic epigenome, including global DNA re-methylation, to differentiate into spermatogonia/SSCs, a direct precursor for spermatozoa differentiation (Lee *et al.*, 2014). PGCs and spermatogonia/SSCs therefore exhibit dimorphic epigenomic properties and have been thought to represent highly distinct cellular states. Contrary to this notion, our nucleome analyses have uncovered a smooth and unidirectional maturation of higher-order genome organization from pluripotent precursors (mESCs/EpiLCs) to PGCs (d2/d4/d4c7 mPGCLCs) and then to spermatogonia/SSCs (GSCs), involving progressive euchromatization and radial chromosomal re-positioning (Fig 1 and 8). This finding delineates a common nuclear-architectural foundation towards gamete generation in both sexes, a coordination not found in somatic lineages. This widespread euchromatization might underlie the potential of GSCs to de-differentiate into pluripotent stem cells, albeit at a low frequency (Kanatsu-Shinohara *et al*, 2004). Thus, germ-cell development entails mechanisms that create and preserve a broadly euchromatic genome, while simultaneously accommodating essential epigenetic orchestrations. Our findings also demonstrate that global DNA methylation and euchromatization are dissociable events.

As a key mechanism for global euchromatization, we have shown that germ-cell development distinctly down-regulates H3K9me2, an aggregative force for heterochromatin formation (Poleshko *et al*, 2019), and progressively restricts LADs to around centromeres (Fig 2 and 4). These events would be mediated at least in part through the repression of SETDB1 and EHMT1, K9MTases acting in both the A and B compartments (Fukuda *et al.*, 2021), as well as lamin B1 itself. On the other hand, germ cells up-regulate *Suv39h1* and *h2*, K9MTases specific to the B compartment and particularly for pericentromeric regions. This results in an expansion of H3K9me3 into broad domains in GSCs with an appreciable increase in both local and distal compaction among such domains (Fig 5), consistent with the notion of a critical threshold of H3K9me3 domain width for phase separation to take place via HP1 (Sanulli *et al*, 2019). This compaction would also contribute to the formation of PMDs, and most remarkably, those on the Y chromosome, likely by physically excluding spermatogenesis-associated NSD1 and preventing H3K36me2 depositions (Fig 6). Thus, typical LADs mediated by H3K9me2, which are seen in pluripotent precursors as well as in most somatic lineages, are progressively re-organized into a minimal state marked by H3K9me3 during germ-cell development. Importantly, the positional preference of H3K9me3-associated minimal LADs is in part attributable to the density of evolutionarily young TEs that are enriched near centromeres (Fig 5, Fig

EV5), indicating a critical role of inherent genomic properties in shaping the fundamental nuclear architecture. In good agreement with this concept, cell-type specific LADs have been reported to be enriched in such TEs (Keough *et al*, 2021). The involvement of H3K9 demethylases and the interplay among associated machineries for LAD formation warrant further investigation.

Despite adopting a highly permissive epigenome with abundant enhancer-like open sites, d4c7 mPGCLCs strengthened their chromatin insulation to thwart spurious distal activation, which, combined with a mechanism to ensure low H3K4me3 levels, would prevent the pervasive poised enhancers from realizing their potential (Fig 2 and 3). Thus, epigenetic reprogramming creates PGCs that have almost no DNA methylation and a highly open epigenome, but that are protected by elevated H3K27me3 (Ohta *et al.*, 2017) and CTCF insulation against hyper-transcription. As to a possible mechanism for the enhanced insulation, we revealed a reduced residence time of the loop extrusion machinery at TAD boundaries in d4c7 mPGCLCs (Fig EV3H-J). Such a reduction in residence time could be achieved through multiple mechanisms, including the use of variant cohesin complexes and modulating the balance between cohesin loading/release factors (Cuadrado *et al*, 2019; Wutz *et al*, 2017). Clarification of these potential mechanisms warrants future investigation.

On the other hand, such protective mechanisms must be at least partly disentangled upon male and female germ-cell specification to eventually achieve full activation of the gametogenic program. Accordingly, a failure of such unraveling and a partial retention/aberrant development of the PGC-like nucleome together contributed to the limited spermatogenic capacities of GSCLCs (Fig 6, Appendix Fig S4). In the original GSCLC induction strategy, d4 mPGCLCs, which are in the middle of epigenetic reprogramming and bear ~50% genome-wide DNA methylation, were aggregated with embryonic testicular somatic cells for differentiation into spermatogonia-like cells (Ishikura *et al.*, 2016). We speculate that precocious testicular sex-determining signals on mPGCLCs might be a reason for mis-organized nucleome in the originally reported GSCLCs. In good agreement with this speculation, we have recently succeeded in deriving fully functional GSCLCs using d4c5 mPGCLCs, which have an almost fully complete epigenetic reprogramming, as starting materials for aggregation culture with embryonic testicular somatic cells (Ishikura *et al*, 2021). The nucleome analysis of these newly established GSCLCs would be important to confirm this hypothesis.

The nucleome programming for germ-cell development that we have delineated herein, which involves progressive euchromatization with peripheral centromere positioning, is reminiscent of climbing up the Waddington's landscape of epigenesis (Fig 8), and we propose that it constitutes at least part of the mechanism for creating nuclear totipotency, including meiotic potential. Elucidation of the nucleome programming during

germ-cell development in other mammals, including humans, will be crucial for a more comprehensive understanding of nuclear totipotency and its evolutionary divergence. The rich datasets we have assembled would be invaluable as a benchmark for mammalian *in vitro* gametogenesis studies (Saitou & Hayashi, 2021) and for future studies aiming to identify unifying principles for the acquisition of unique cellular identities across lineages. Further, they could contribute to the development of powerful computational frameworks, which in turn could help integrate time-series multi-omics datasets and unveil hidden insights.

ACKNOWLEDGMENTS

We thank the members of our laboratory for their helpful input on this study. We are grateful to Y. Nagai, N. Konishi, E. Tsutsumi, and M. Kawasaki of the Saitou Laboratory, to the DNAFORM genetic analysis department for NET-CAGE library preparation and sequencing, to the Single-Cell Genome Information Analysis Core (SignAC) in ASHBi for their technical assistance and help with all the other sequencing experiments, to R. Maeda of the Tachibana Laboratory for helpful suggestions for ChIP-seq, to S. Nagaoka and K. Kurimoto of the Kurimoto Laboratory and G. Bourque of the Bourque Laboratory for thoughtful discussions on the data analysis, and to C. Horth from the Majewski Laboratory for her assistance with histone extraction. This work was supported in part by a Grant-in-Aid for Specially Promoted Research from JSPS (17H06098, 22H04920), a JST-ERATO Grant (JPMJER1104), a Grant from HFSP (RGP0057/2018), Grants from the Pythias Fund and Open Philanthropy Project to M.S., JSPS KAKENHI Grants (JP18H02613, JP20H05387) to S.Y., and NIH grants (CA196539, NS111997) to B.A.G. M.N. is a fellow of the Takeda Science Foundation. B.H. is supported by studentship awards from the Canadian Institutes of Health Research and the Fonds de recherche du Québec – Santé.

AUTHOR CONTRIBUTIONS

M.N., B.H., S.Y., and M.S. conceived the project and designed experiments. M.N. performed all cell cultures and inductions with assistance from H.O., Y.Ishikura. and Y.N. M.N. performed immunofluorescence and its analysis with assistance from H.O., N.K. and K.M. M.N. and F.U. performed western blot and its analysis with assistance from Y.N., S.S., and Y.K. M.N. performed FISH with assistance from I.O. M.N. performed histone extraction and M.C. performed mass spectrometry under the supervision of B.A.G. M.N. and A.Y. performed ChIP-seq with assistance from S.Y. and T.Y. M.N. performed ATAC-seq with assistance from S.Y., H.I., and T.Y. M.N. performed in situ Hi-C with assistance from S.Y., R.S., G.W., K.T., J-M.P., and L.A.M. M.N. performed NET-CAGE with assistance from T.K. under the supervision of Y.M. M.N. and B.H. performed all data analysis with assistance from Y.Y. and J.M. B.H. performed polymer simulation and analysis with assistance from Y.Imoto., K.M., and Y.H. M.N., B.H., and M.S. wrote the manuscript with input from all co-authors. S.Y., J.M., and M.S. supervised the project.

DISCLOSURE AND COMPETING INTERESTS STATEMENT

M.S. is an EMBO Associate Member.

MATERIALS AND METHODS

Methods and Protocols

Culture of mESCs

The BDF1-2-1 mouse mESCs bearing *Blimp1-mVenus* and *Stella-ECFP* (BVSC) transgenes (Ohta *et al.*, 2021) were cultured as described previously (Hayashi *et al.*, 2011). Briefly, mESCs were maintained in N2B27 medium supplemented with PD0325901 (0.4 uM) (Stemgent, 04-2006), CHIR99021 (3 uM) (Bio Vision, 4423), and leukemia inhibitory factor (LIF) (1000 U/ml) (Merck Millipore, ESG1107) on a 12-well plate coated with poly-L-ornithine (0.01%) (Sigma, P3655) and laminin (10 ng/ml) (BD Biosciences, 354232). In this study, all cells were cultured at 37°C under an atmosphere of 5% CO2 in air.

Induction of EpiLCs and mPGCLCs

Induction of EpiLCs and PGCLCs was performed as described previously (Hayashi *et al.*, 2011) with minor modifications. Briefly, the EpiLCs were induced by plating 8×10^4 mESCs on a well of a 12-well plate coated with human plasma fibronectin (16.7 mg/ml) (Merck Millipore, FC010) in N2B27 medium containing activin A (20 ng/ml) (Peprotech, 120-14), bFGF (12 ng/ml, 13256029) (Invitrogen), and KSR (1%) (Gibco, 10828028). mPGCLCs were induced from d2 EpiLCs (2 days after induction) under a floating condition in wells of a low-cell-binding U-bottom 96-well plate in GMEM medium (Thermo Fisher Scientific, 11710035) containing 15% KSR (Gibco, 10828028), 0.1 mM NEAA (Thermo Fisher Scientific, 11140-050), 1 mM sodium pyruvate (Thermo Fisher Scientific, 11360-070), 0.1 mM β-mercaptoethanol (Thermo Fisher Scientific, 21985023), 100 U/ml penicillin, 0.1 mg/ml streptomycin (Thermo Fisher Scientific, 15140148) and 2 mM L-glutamin (Thermo Fisher Scientific, 25030149) supplemented with BMP4 (500 ng/ml) (RSD, 314BP01M), LIF (1000 U/ml) (Merck Millipore, ESG1107), SCF (100 ng/ml) (RSD, 455MC), and EGF (50 ng/ml) (RSD, 2028EG).

Expansion culture of mPGCLCs

The expansion culture of mPGCLCs was performed as previously described (Ohta *et al.*, 2021). Briefly, following incubation in TrypLE™ Express (Gibco, 12604-021) for 10 min, the aggregates of d4 mPGCLCs (PGCLCs induced for 4 days) were dissociated into single cells by rigorous pipetting. Subsequently, BV-positive cells were sorted with a FACSAria III cell sorter. Purified d4 mPGCLCs were cultured on m220-5 cells as the feeder cells in GMEM (Gibco, 11710035) containing 10% KSR (Gibco, 10828028), 0.1 mM NEAA (Thermo Fisher Scientific, 11140-050), 1 mM sodium pyruvate (Thermo Fisher Scientific, 11360-070), 0.1 mM β-mercaptoethanol (Thermo Fisher Scientific, 21985023), 100 U/ml penicillin, 0.1 mg/ml streptomycin (Thermo Fisher Scientific, 15140148), 2 mM L-glutamin (Thermo Fisher Scientific, 25030149), 2.5% FBS (Hyclone, SH30910.03), SCF (100 ng/ml) (RSD, 455MC), 10 mM forskolin (Sigma,

F3917), 10 uM rolipram (Abcam, AB120029), and 5 uM CsA (Sigma, 30024). Half of the culture medium was changed every two days.

Culture of GSCs and GSCLCs

GSCs and GSCLCs bearing *Acrosin-EGFP* and beta-*Actin-EGFP* (AAG) transgenes (Ohta *et al*, 2000) were cultured as described previously (Ishikura *et al.*, 2016). Briefly, cells were cultured in Stempro-34 SFM supplemented with Stempro Supplement (Gibco, 10639011), with 0.1 mM β-mercaptoethanol (Thermo Fisher Scientific, 21985023), 1% FBS (Hyclone, SH30910.03), 1×MEM vitamin solution (Thermo Fisher Scientific, 11120052), 5.0 mg/ml AlbMAXI (Gibco, 11020062), 0.1 mM NEAA (Thermo Fisher Scientific, 11140-050), 1 mM sodium pyruvate (Thermo Fisher Scientific, 11360-070), 0.1 mM β-mercaptoethanol (Thermo Fisher Scientific, 21985023), 100 U/ml penicillin, 0.1 mg/ml streptomycin (Thermo Fisher Scientific, 15140148), 2 mM L-glutamin (Thermo Fisher Scientific, 25030149), 1×Insulin-Transferrin-Selenium (ITS-G) (Gibco, 41400045), 10 ng/ml bFGF (Invitrogen, 13256029), 20 ng/ml GDNF rat recombinant (RSD, 512GF), 20 ng/ml EGF (RSD, 2028EG), and 1000 U/ml LIF (Merck Millipore, ESG1107) in a well of a 6-well plate on mouse embryonic fibroblast cells (MEFs) as feeder cells. Half of the medium was replaced every two or three days.

Immunofluorescence staining

The following primary antibodies were used at the indicated dilutions: rabbit anti-Laminb1 (1/1000; Abcam ab16048); mouse anti-H3K9me2 (1/500; MBL, MABI0317); mouse anti-H3K9me3 (1/500; MBL, MABI0318); and mouse anti-H3K27me3 (1/500; Merk, 07-449).

The following secondary antibodies from Thermo Fisher Scientific were used at a 1/500 dilution: Alexa Fluor 568 goat anti-rabbit IgG; Alexa Fluor 488 goat anti-rabbit IgG; and Alexa Fluor 568 goat anti-mouse IgG.

Immunofluorescence (IF) staining was performed as previously described (Ohta *et al.*, 2017) with minor modifications. Briefly, cells were fixed in 4% PFA (paraformaldehyde) (Nacalai Tesque, 26126-25) for 30 min at RT. After fixation, cells were washed in PBS three times and then permeabilized in 1% Triton-X100/PBS for 5 min on ice. Then, they were washed in PBS three times and incubated in 1% BSA (Sigma, A4503-10G)/PBS for 1 h. The cells were incubated with primary antibodies in 1% BSA/PBS overnight. After incubation with primary antibodies, the cells were washed in PBS three times and then incubated for 2 h with secondary antibodies and DAPI (1 mg/ml) (Wako, 342-07431) at RT. Then, they were washed three times in PBS and mounted in VECTOR SHIELD (Vector Laboratories, H-1000-10). Images were captured with a confocal microscope (LSM780 or LSM980 with Airyscan2; Zeiss).

Probe preparation for DNA-FISH against major satellite repeats

The probe against major satellite repeats was generated as previously described (Anton *et al*, 2014) with some modifications. DNA fragments were amplified with forward (5'-GCGAGAAAACTGAAAATCAC-3') and reverse (5'-TCAAGTCGTCAAGTGGATG-3') primers using mouse genomic DNA as a template, and purified using a QIA quick PCR purification kit (QIAGEN, 28104). 500 ng of the PCR product was labeled with Orange-dUTP (Abbott, 02N33-050) using a Nick translation kit (Roche, 10976776001).

DNA-FISH

DNA-FISH was performed as described previously (Okamoto *et al*, 2005). Briefly, cells were cultured in a film-bottom dish (Matsunami Glass, FD10300) and fixed in 3% PFA/PBS (Nacalai Tesque, 26126-25) for 10 min at RT. After a brief wash in PBS, cells were permeabilized in 0.5% Triton-X100 in PBS for 5 min on ice and stored in 70% ethanol at −30°C by the day of use. Then, the DNA was denatured in 50% FA (formamide) (Nacalai Tesque, 16228-05)/2×SSC pH 7.4 (Sigma, S6639) for 40 min at 80°C and dehydrated through an ice-cold ethanol series. Hybridization with probes was performed at 37°C overnight. After incubation, the samples were washed in 50% FA/2×SSC followed by 2×SSC. The samples were counterstained with DAPI (1 mg/ml) (Wako, 342-07431), and mounted and viewed under a confocal microscope (Zeiss LSM980 with Airyscan2). Images were analyzed using Imaris 9.1.2 software (Bitplane).

Western blot analysis

The following primary antibodies were used at the indicated dilutions: rabbit anti-Lamin b1 (1/1000; Abcam ab16048); mouse anti-H3K9me2 (1/500; MBL, MABI0317); mouse anti-H3K9me3 (1/500; MBL, MABI0318); and mouse anti-H3K27me3 (1/500; MBL, MABI0323); rabbit anti-H3 (1/10000; CST, #9715); rabbit anti-CTCF (1/500; CST, #3418); mouse anti-G9a (1/500; R&D, PP-A8620A-00); mouse anti-GLP (1/500; R&D, PP-B0422-00); rabbit anti-Setdb1 (1/1000; Proteintech, 11231-1-AP); mouse anti-α-tubulin (1/5000; Merk, T9026); and mouse anti-β-actin (1/5000; MBL, M177-3).

The following secondary antibodies from Merk were used at the indicated dilutions: goat anti-rabbit IgG conjugated with peroxidase (1/8000); and sheep anti-mouse IgG conjugated with peroxidase (1/10000).

Western blot was performed as previously described (Hayashi *et al.*, 2011) with slight modifications. Briefly, cells were lysed by RIPA buffers (Santa Cruz, SC-24948). After incubation for 30 min at 4°C with rotation, the lysates were sonicated by Bioruptor using 10 cycles of 30 s on/30 s off. Then, the lysates were spun down at 14000 rpm for 15 min at 4°C and the supernatant was collected. A BCA assay was performed using a Pierce™ BCA Protein Assay Kit (Thermo Fisher Scientific, 23227) to measure the

protein concentration. For western blot, 4.5 mg of whole cell lysate or 2.25 mg of chromatin fraction was loaded onto each lane. After addition of 4×Laemmli buffer (Bio-Rad, #1610747), the sample was run by SDS-PAGE, followed by blotting to PVDF membrane (pore size: 0.45 mm) (Millipore, IPVH00010) in CAPS buffer (10 mM CAPS-NaOH pH 11, 5% methanol). After blotting, the membrane was incubated for 1 h in 0.1% Tween-20/PBS (PBST) with 1% skim milk (BD Bioscience, 232100). After blocking, the membrane was incubated overnight with the primary antibodies in 0.1% PBST with 1% skim milk. The membrane was washed in 0.1% PBST, followed by incubation for 2 h with the secondary antibodies in the 0.1% PBST with 1% skim milk. After washing in 0.1% PBST three times, secondary antibodies were detected by Chemilumi One Super (Nacalai Tesque, 02230-14) using Fusion solo 4S (Vilber). Quantification analysis of the signal intensity was performed in ImageJ v2.1.0 (NIH). Target protein signals were normalized by the loading control.

Chromatin fraction isolation

Chromatin fractionation was performed as previously described (Wutz *et al.*, 2017). In brief, cells were resuspended in extraction buffer (20 mM Tris-HCl pH 7.5, 100 mM NaCl, 5 mM $MgCl_2$, 2 mM NaF, 10% glycerol, 0.2% NP-40, 20 mM β-glycerophosphate, 0.5 mM DTT, and protease inhibitor cocktail (Roche, 11873580001)). The chromatin pellet was fractionated by centrifugation at 2000 g for 5 min and washed in the same buffer three times. Then, the chromatin pellet was resuspended in RIPA buffer (Santa Cruz, SC-24948) and processed along with the whole cell lysate by a downstream BCA assay (Thermo Fisher Scientific, 23227) followed by western blot.

Visualization and analysis of nuclei by DAPI staining

All cells except d2 mPGCLCs were cultured in a film-bottom dish (Matsunami Glass, FD10300). d2 mPGCLCs were attached on a slide glass (MATSUNAMI, S9901-9905) using Cyto Spin 4 (Thermo Fisher Scientific) as previously described (Ohta *et al.*, 2017). Cells were fixed in 4% PFA (Nacalai Tesque, 26126-25) at RT for 30 min and washed in PBS three times. For permeabilization, cells were incubated on ice in 0.5% TritonX-100/PBS for 5 min. Then, cells were incubated in DAPI solution (1 mg/ml) (Wako, 342-07431) for 8 min, mounted and viewed under a fluorescence microscope. Confocal z-series images with an interval of 0.14 μm were captured by Zeiss LSM980 with Airyscan2 using a 405 nm wavelength and a 63×objective oil-immersion lens. For DAPI-staining analysis, cells were attached to slides using Cyto Spin 4 (Thermo Fisher Scientific) as previously described (Ohta *et al.*, 2017) in order to avoid the effect of differences in their colony shapes. DAPI-staining and image acquisition were performed as described above. Acquired images were processed as follows. The nuclear mask, nuclear rim, and DAPI dense regions were defined in each z-slice using ImageJ custom script as previously described (Miura, 2020). Then, the slice showing the maximum

diameter was decided for each cell as a representative slice, and the representative slice ±5 slices for each cell (i.e., 11 slices/cell) were used in the downstream analysis. Approximately 20–30 cells were analyzed in each cell type. The parameters presented in the Figures were calculated using R custom script.

Histone extraction for mass spectrometry

Frozen cell pellets containing 3 million cells were lysed in nuclear isolation buffer (15 mM Tris pH 7.5, 60 mM KCl, 15 mM NaCl, 5 mM $MgCl_2$, 1 mM $CaCl_2$, 250 mM sucrose, 10 mM sodium butyrate, 0.1% v/v b-mercaptoethanol (Nacalai Tesque, 21438-82), commercial phosphatase and protease inhibitor cocktail tablets (Roche, 4906837001; Thermo Fisher Scientific, A32955)) containing 0.3% NP-40 alternative on ice for 5 min. Nuclei were washed in the same solution without NP-40 twice and the pellet was slowly resuspended while vortexing in chilled 0.4 N H_2SO_4, followed by 3 h of rotation at 4°C. After centrifugation, the supernatants were collected and proteins were precipitated in 20% TCA overnight at 4°C, washed once with 0.1% HCl (v/v) acetone and then twice with acetone only, and resuspended in deionized water. Acid-extracted histones (20–50 μg) were resuspended in 100 mM ammonium bicarbonate pH 8, derivatized using propionic anhydride and digested with trypsin as previously described (Sidoli *et al*, 2016). After the second round of propionylation, the resulting histone peptides were desalted using C18 Stage Tips, dried using a centrifugal evaporator and reconstituted using 0.1% formic acid in preparation for liquid chromatography-mass spectrometry (LC–MS) analysis.

LC/LC-MS

Nanoflow liquid chromatography was performed using a Thermo Fisher Scientific Dionex UltiMate 3000 LC system equipped with a 300mm ID x 0.5-cm trap column (Thermo) and a 75 mm ID x 20-cm analytical column packed in-house using Reprosil-Pur C18-AQ (3 mm; Dr. Maisch). Buffer A was 0.1% formic acid and Buffer B was 0.1% formic acid in 80% acetonitrile. Peptides were resolved using a two-step linear gradient from 5% B to 33% B over 45 min, then from 33% B to 90% B over 10 min at a flow rate of 300 nL min^{-1}. The HPLC was coupled online to an Orbitrap QE-HF mass spectrometer operating in the positive mode using a Nanospray Flex Ion Source (Thermo Fisher Scientific) at 2.3 kV. Two full mass spectrometry scans (m/z 300–1,100) were acquired in the Orbitrap Fusion mass analyzer with a resolution of 120,000 (at 200 m/z) every 8 data-independent acquisition tandem mass spectrometry (MS/MS) events, using isolation windows of 50 m/z each (for example, 300–350, 350–400, 650–700). MS/MS spectra were acquired in the ion trap operating in normal mode. Fragmentation was performed using collision-induced dissociation in the ion trap mass analyzer with a normalized collision energy of 35. The automatic gain control target and maximum injection time were 5×10^5 and 50 ms for the full mass spectrometry scan, and 3×10^4 and 50 ms for the MS/MS scan, respectively. Raw files were analyzed using

EpiProfile 2.0 (Yuan *et al*, 2018). The area for each modification state of a peptide was normalized against the total signal for that peptide to give the relative abundance of the histone modification.

ChIP-seq library preparation and sequencing

The ChIP-seq library preparation was performed as previously described (Lee *et al*, 2006) with minor modifications. We used harvested mESCs and EpiLCs, and FACS-sorted BV-positive cells for d2 mPGCLCs and d4c7 mPGCLCs samples, and FACS-sorted AAG-positive cells for GSCs and GSCLCs samples. Briefly, the harvested cells were crosslinked with 1% formaldehyde (Thermo Fisher Scientific, 28906)/PBS for 10 min at RT and quenched with 125 mM glycine. Crosslinked cells were lysed consecutively using LB1 (50 mM HEPES-KOH pH 7.5, 1 mM EDTA, 140 mM NaCl, 10% glycerol, 0.5% NP-40, 0.25% Triton-100, protease inhibitors (Roche, 11873580001)), LB2 (10 mM Tris-HCl pH 8.0, 1 mM EDTA, 0.5 mM EGTA, 200 mM NaCl, protease inhibitors), and LB3 (50 mM Tris-HCl pH 8.0, 1 mM EDTA, 0.5 mM EGTA, 100 mM NaCl, 0.1% Na-deoxycholate, 0.5% N-lauroylsarcosine, protease inhibitors) and then sonicated by a picoruptor to achieve a mean DNA fragment size of around 200–400 bp. Sonicated chromatin was incubated with Dynabeads M-280 Sheep anti-Mouse IgG beads (Thermo Fisher Scientific, DB11201) or Dynabeads ProteinA beads (Thermo Fisher Scientific, DB10001) for 35 min at 4°C for preclear. Precleared chromatin was then incubated with antibodies that were preincubated with the appropriate Dynabeads in 0.5% BSA (Gibco, 15260-037) in PBS as follows: a chromatin equivalent of 5×10^5 cells with anti-H3K4me1 (rabbit monoclonal, CST, #5326, 5 µl), anti-H3K9me2 (mouse monoclonal, MBL, MABI0317, 5 µl), anti-H3K27me3 (mouse monoclonal, MBL, MABI0323, 5 µl); 1×10^6 cells with anti-H3K4me3 (mouse monoclonal, MBL, MABI0304, 5 µl), anti-H3K9me3 (mouse monoclonal, MBL, MABI0318, 5 µl), anti-H3K36me2 (rabbit monoclonal, CST, #2901, 5 µl), anti-H2AK119ub1 (rabbit monoclonal, #8240, 10 µl), anti-H3K36me3 (rabbit polyclonal, Active Motif, 61101, 2 µl); 1.5×10^6 cells with anti-H3K27ac (mouse monoclonal, MBL, MABI0309, 5 µl); 2×10^6 cells with anti-CTCF (rabbit monoclonal, CST, #3418, 5 µl), anti-Laminb1 (rabbit polyclonal, Proteintech, 12987-1-AP, 10 µl); 4×10^6 cells with anti-Ring1b (rabbit monoclonal, CST, #5694, 10 µl); and 4.5×10^6 cells with anti-Rad21 (rabbit monoclonal, ab992, 5 µl).

After incubation for 6 h at 4°C, the beads were washed 4 times in wash buffer 1 (20 mM Tris-HCl pH 8.0, 2 mM EDTA, 150 mM NaCl, 1% TritonX-100, 0.1% SDS), 2 times in wash buffer 2 (20 mM Tris-HCl pH 8.0, 2 mM EDTA, 500 mM NaCl, 1% TritonX-100, 0.1% SDS), and 2 times in wash buffer 3 (10 mM Tris-HCl pH 8.0, 1 mM EDTA, 250 mM LiCl, 1% Na-Deoxycolate, 1% NP-40). Then, the washed beads were eluted in 10 mM Tris-HCl pH 8.0, 5 mM EDTA, 300 mM NaCl, and 1% SDS, and crosslinks were reversed overnight at 65°C. Input samples were treated in a similar

manner. The following day, the IP and Input samples were incubated with RNaseA (Thermo Fisher Scientific, EN0531) and proteinase K (Thermo Fisher Scientific, AM2546). IP or Input DNA was purified using a QIA quick PCR purification kit (QIAGEN, 28104).

ChIP-seq libraries were prepared using a KAPA Hyper Prep Kit (KAPA, KK8504) following the manufacturer's guidelines. An adaptor kit (Fastgene, FG-NGSAD24) was used for the sample indexes. The average size and concentration of libraries were analyzed using LabChIP GX (PerkinElmer) and a KAPA library Quantification kit (KAPA, KK4824), respectively. Libraries were sequenced as 75 bp single-end reads on an Illumina NextSeq 500/550 platform with a NextSeq 500/550 High Output kit (75 cycles) (Illumina, 20024906).

ATAC-seq library preparation and sequencing

The ATAC-seq experiment was performed as described previously (Buenrostro *et al*, 2013; Corces *et al*, 2017) with minor modifications. We used FACs-sorted viable cells for mESCs and EpiLCs; FACS-sorted BV-positive cells for d2 mPGCLCs, d4 mPGCLCs, and d4c7 mPGCLCs; and FACS-sorted AAG-positive cells for GSCs and GSCLCs. 50,000 cells were permeabilized in cold lysis buffer 1 (10 mM Tris-HCl pH8.0, 10 mM NaCl, 3 mM $MgCl_2$, 0.1% NP-40, 0.1% Tween20, 0.1% Digitonin (Promega, G9441)) for 3 min followed by addition of 1 ml of cold lysis buffer 2 (10 mM Tris-HCl pH8.0, 10 mM NaCl, 3 mM $MgCl_2$, 0.1% Tween20). Nuclei were centrifuged and resuspended with 50 ml of transposase reaction mixture (25 ul of 2×TD buffer (Illumina, 20034197), 2.5 ml of Transposase (Illumina, 20034197), 16.5 ml of PBS, 0.5 ml of Digitonin, and 0.5 ml of Tween-20, 5 ul of DDW). After incubation at 37°C for 30 min, the tagged DNA was purified using a Minelute PCR purification kit (QIAGEN, 28004). The purified DNA was amplified for 8 cycles by a PCR reaction (NEB, M0541S) followed by size selection using AMPure XP beads (Corning, MAG-PCR-CL-250) to remove primer dimers. Libraries were sequenced as 2×75bp paired-end reads on an Illumina NextSeq 500/550 platform with a NextSeq 500/550 Mid Output Kit (150 cycles) (Illumina, 20024904) or NextSeq 500/550 High Output Kit (150 cycles, 20024907) (Illumina).

In situ Hi-C library preparation and sequencing

In situ Hi-C library preparation was performed as described previously (Belaghzal *et al*, 2017; Rao *et al*, 2014) with minor modifications. We used the whole harvested cells for mESCs and EpiLCs; FACS-sorted BV-positive cells for d2 mPGCLCs and d4c7 mPGCLCs; and FACS-sorted AAG-positive cells for GSCs and GSCLCs. 2.5×10^6 cells were used for one replicate. The cells were fixed by 1% formaldehyde (Sigma, 252549)/HBSS and lysed in lysis buffer (10 mM Tris-HCl pH 8.0, 10 mM NaCl, 0.2% NP-40) for 30 min on ice with frequent inversion. The cells were digested by 500 U of

DpnII (NEB, R0543L) overnight at 37°C. Following biotin filling (Thermo Fisher Scientific, 19524-016; NEB, M0210S), proximity ligation (Thermo Fisher Scientific, 15224090) and reverse crosslinking, DNA was purified by ethanol precipitation and sheared to 200-400 bp fragments using a Covaris E220 sonicator (Covaris) at 4°C (10% Duty Factor, 200 cycles/burst, 175 W Peak Incident Power, 110 s). Ligation fragments containing biotin were immobilized on MyOne Streptavidin T1 beads (Thermo Fisher Scientific, 65001) followed by library preparation using a NEB library preparation kit (NEB, E7645S; NEB, E7335S) according to the manufacturer's guidelines. The libraries were amplified in 8 cycles and DNA fragments of 300–800 bp were selected using AMPure XP beads (Corning, MAG-PCR-CL-250). Libraries were sequenced as 2×100bp paired-end reads on an Illumina NovaSeq 6000 platform with a NovaSeq 6000 S1 Reagent Kit (200 cycles) (Illumina, 20012864).

NET-CAGE library preparation and sequencing

NET-CAGE library preparation was performed as described previously (Hirabayashi *et al*, 2019) with minor modifications. For extraction of nascent RNA, cells were first lysed with 1400 µl of Buffer A, which is Nuclei EZ Lysis Buffer (Sigma, NUC101-1KT) supplemented with 25 µM α-amanitin (Wako, 1022961), 1×cOmplete Protease Inhibitor Cocktail (Roche, 4693116001) and SUPERase•IN RNase Inhibitor (20 units; Thermo Fisher Scientific, AM2694), and then incubated on ice for 10 min and centrifuged at 800 g for 5 min at 4°C followed by washing once with the same buffer. Washed pellets were resuspended in 200 µl of Buffer B, containing 1% NP-40, 20 mM HEPES pH 7.5, 300 mM NaCl, 2 M urea, 0.2 mM EDTA, 1 mM dithiothreitol (DTT) (Promega, P1171), 25 µM α-amanitin, 1×cOmplete Protease Inhibitor Cocktail and SUPERase•IN RNase Inhibitor (20 units), and incubated for 10 min on ice. The suspension was centrifuged at 3,000g for 2 min at 4°C. After removing the supernatant, the nuclear insoluble fraction was washed once with 100 µl of Buffer B. DNase I solution (50 µl) containing DNase I (10 units; Thermo Fisher Scientific, 89836), 1×DNase I Buffer (Thermo Fisher Scientific) and SUPERase•IN RNase Inhibitor (20 units) was added to the pellets. The samples were incubated for 30 min at 37°C while being pipetted up and down several times at 10-min intervals. QIAzol (700 µl) was then added and the solution was thoroughly mixed. RNA was extracted with an miRNeasy Mini kit (QIAGEN, 217004) according to the manufacturer's instructions. On-column DNase I digestion was carried out with an RNase-free DNase set (QIAGEN, 79254). RNA was eluted in 30 µl RNase-free water, and its quality and quantity were measured with a Qubit RNA HS assay kit (Thermo Fisher Scientific, Q32855) and 2100 BioAnalyzer (Agilent). cDNA was synthesized from 200 ng of nascent RNA. CAGE libraries were generated according to the no amplification non-tagging CAGE libraries for Illumina next-generation sequencers (nAnT-iCAGE) protocol (Murata *et al*, 2014) with PCR amplifications (Takara, R060A). All CAGE libraries were sequenced in 75 bp single-end reads on an Illumina NextSeq 500 platform.

ChIP-seq data processing

Single-end reads were processed using Trim-Galore! v0.4.1/cutadapt v1.9.1 (Krueger *et al*, 2021; Martin, 2011) to remove adaptor sequences. The truncated reads were then aligned to (GRCm38p3) using Bowtie2 v2.3.4.1 (Langmead & Salzberg, 2012) with the "-very-sensitive" option. Reads aligned to chromosomes 1 to 19, X, and Y were converted to the BAM format by SAMtools v1.7 (Li *et al*, 2009). BED files were obtained from the BAM files using the bamtobed command of BEDTools v2.29.2 (Quinlan & Hall, 2010). BigWig files were generated from the BAM files using bamcoverage for raw count with the "--normalizeUsing CPM -bs 25" or bamcompare for IP/Input command with the "--pseudocount 1 -bs 1000" option of deepTools v3.5.0 (Ramirez *et al*, 2016) In both cases, the blacklist regions (Amemiya *et al*, 2019) were excluded.

The regions enriched by epigenetic marks were identified using peak calling tools. For CTCF peaks, MACS v2.1.1 (Zhang *et al*, 2008) was used with the "-q 0.01 --nomodel --keep-dup all --extsize 200" option. For H3K9me3 domains, epic2 v0.0.41 (Stovner & Saetrom, 2019) was used with "-kd -fdr 0.01" option. The number of IP or Input reads in 10/25/50/100 kb genomic windows were counted by the intersect command of BEDTools v2.29.2, and normalized by total million mapped reads (FPM) and transformed to Log2(IP/Input) for the downstream analysis. The bins in which no reads were detected in the Input samples were excluded.

ATAC-seq data processing

ATAC-seq data processing including public data was performed as previously described (Buenrostro *et al.*, 2013) with minor modifications. First, adaptor sequences were trimmed from the reads using TrimGalore! v0.4.1/cutadapt v1.9.1. These reads were aligned using Bowtie2 v2.3.4.1 to GRCm38p3 with the "--very-sensitive -X 2000" option. The properly mapped reads with the flag (99, 147, 83 or 163) were extracted by awk, and mitochondrial reads were excluded. Duplicated reads were removed using the MarkDuplicates command of Picard Tools v2.18.23 (https://broadinstitute.github.io/picard/). These de-duplicated reads were then filtered for high quality (MAPQ≧30). The reads with an insert size of less than 100 bp were extracted as nucleosome free region (NFR) reads. Bed files for downstream analysis were generated by the bamtobed command of BEDTools v2.29.2 with the "-bedpe" option. BigWig files were generated from the BAM files using bamcoverage for raw count with the "--normalizeUsing CPM -bs 25" option of deepTools v3.5.0. The blacklist regions (https://www.encodeproject.org/files/ENCFF999QPV/) were excluded.

Peak calling was performed using MACS v2.1.1 with the "--nomodel --shift -100 --extsize 200 --keep-dup all" option after shifting NFR reads with the offset by +4 bp in

the + strand and by -5 bp in the - strand. Then, confident peak sets in each cell type were obtained by the IDR method (https://www.encodeproject.org/software/idr/) using two replicates.

PBAT data processing

Public read data processing of the methylation levels was performed as described previously (Shirane *et al*, 2016). In brief, all reads were processed with Trim-Galore! v0.4.1/cutadapt v1.9.1 with the "--clip_R1 4," "--trim1" and "-a AGATCGGAAGAGC" options. Output reads were mapped onto the mouse genome, GRCm38.p6, using Bismark v0.22.1 (Krueger & Andrews, 2011)/Bowtie2 v2.3.4.1 with the "--pbat" option. All public WGBS data were obtained from DDBJ or NCBI SRA ftp sites and processed as described above. Conversion rates were calculated as follows: output reads after Trim-Galore were mapped onto the lambda phage DNA sequence using Bismark v0.22.1/Bowtie2 v2.3.4.1 with the "--pbat" option. From the Bismark's statistics, conversion rates were determined as 1 - ([total mC counts] / [total C and mC counts]). All CpG sites with a read depth of between 4 and 200 were used for the %mC calculations.

3-prime RNA sequencing data processing

Raw 3' RNA-seq data were directly used with Salmon v1.4.0 (Patro *et al*, 2017) with default parameters and --noLengthCorrection to quantify the expression of GENCODE vM25 features on GRCm38.p6. Gene-level expression estimates were aggregated from transcript-level abundance using tximport v1.16.1 (Soneson *et al*, 2015).

In situ Hi-C data processing

Sequences were first trimmed using fastp v0.21.0 (Chen *et al*, 2018) with default options and the --detect_adapter_for_pe flag. Trimmed sequences were then processed using HiCUP v0.8.0 (Wingett *et al*, 2015) with default options and the di-tag length range set to 0–800, with bowtie v2.4.2 as the aligner. hicup2juicer was then used to produce pairs files, which were subsequently ingested with Juicer tools v1.22.01 (Durand *et al*, 2016) for the creation of .hic files. The same set of pairs files were also used to create multi-resolution cooler files using cooler v0.8.10 (Abdennur & Mirny, 2020) with default options. Additionally, HiCSR commit b13ac41 (Dimmick *et al*) was used to de-noise 10 kb-resolution contact maps for visualization. In particular, pooled mESC data from (Bonev *et al.*, 2017) after 10× down-sampling were used for training with default parameters; inference was then performed using default parameters. FAN-C v0.9.13 (Kruse *et al*, 2020) was finally used for the normalization (with default parameters) and subsequent visualization of the enhanced 10 kb matrices, including virtual 4C profiles.

NET-CAGE data processing

Sequences were first trimmed using fastp v0.21.0 and then aligned with STAR 2.7.6a (Dobin *et al*, 2013) using default options. Uniquely mapped reads were converted to coverage bigWig tracks with G-bias correction using CAGEr v1.32.0 (Haberle *et al*, 2015) with default options. Tag clusters were identified using CAGEfightR v1.7.6 (Thodberg *et al*, 2019) with pooledCutoff = 0.1 and mergeDist = 20 for unidirectional clusters as well as balanceThreshold = 0.8 for bidirectional clusters. These clusters were subsequently filtered to require at least 1 sample demonstrating an expression level exceeding 1 TPM. Unidirectional clusters (putative promoters) were removed if they overlapped bidirectional clusters (putative enhancers), and the two region sets were subsequently combined to identify coordinately regulation enhancer-promoter co-transcription across stages. In particular, Kendall correlation was used to find putative enhancers within 1 mb of putative promoters that exhibited correlated expression patterns, with TPM as the expression unit.

Global Hi-C metrics

HiCRes v1.1 (Marchal *et al*, 2020) with default parameters was used for the resolution of contact maps following the definition in (Rao *et al.*, 2014). Matrix similarity scores were computed using HiCRep.py v0.2.3 (Lin *et al*, 2021) with --binSize=50000 --dBPMax=5000000 --h=3. Contact probability decay (i.e., the average contact frequency across different genomic separation distances) was assessed using the compute-expected and logbin-expected modules from cooltools v0.4.0 (Venev *et al*, 2021) at all resolutions, in both cis and trans. 3D models of individual chromosomes were produced using CSynth commit 26e21fb (Todd *et al.*, 2021) with balanced 50 kb cis matrices, whose coordinates are normalized to achieve unit backbone length (i.e., the sum of Euclidean distance between adjacent beads being 1); and the size of these predicted structures are taken to be the volume of their 3D convex hulls.

Compartment-related analysis

For analyses involving data across multiple studies, eigendecomposition was performed at 100 kb resolution using the call-compartments module from cooltools v0.4.0 with GC content for orientating the track sign to achieve a positive correlation. For analyses strictly focusing on data generated within this study, dcHiC commit 7b1727f (Wang *et al*, 2021) was used with default parameters to perform simultaneous compartment score calculation across all samples at 50 kb resolution to facilitate statistical comparison across cell types while integrating replicate data. Though the values produced by dcHiC showed high correlation with those generated by cooltools, dcHiC was not applied to public datasets due to a lack of replication in certain datasets. Quantile-binned saddle plots were produced using dcHiC-generated compartment scores and the outputs of compute-expected described above at 50 kb resolution. Binarization of compartment score tracks was carried out using A := score > 0 and B := score < 0. PCA of compartment scores to contrast lineages was done using 100 kb resolution data and bins

non-masked in all samples. The average size of compartments was assessed using an auto-correlation function, where the signal profile is shifted and correlated against the original, using the acf function from R library stats 4.0.3 with na.action = na.pass.

Subcompartment-related analysis

8-state subcompartment labels were assigned to 50 kb bins with balanced contact frequencies using CALDER commit 32220e8 (Liu *et al.*, 2021). The strength of epigenetic signals in each subcompartment was subsequently examined by converting enrichment values to Z-scores genome-wide, after which the average across all bins with the same label was computed. Significant differences in subcompartment proportions were evaluated using the prop.test function from R library stats 4.0.3.

TAD-related analysis

Insulation scores were computed at 10 kb resolution with a window size of 100 kb using the diamond-insulation module of cooltools v0.4.0. Consensus TADs in each dataset were derived by taking the set of bins with boundary prominence scores >0.2 in at least half the cell types present and subsequently pairing neighboring boundaries, with those exceedingly 2mb filtered out, consistently yielding ~4000–5000 domains for each dataset. The significance and strength of TAD-TAD interactions were evaluated using a non-central hypergeometric (NCHG) test implemented as a part of the Chrom3D pipeline (Paulsen *et al*, 2017). Biological replicates (the two deepest ones in case there were more than two) were then used to identify highly reproducible TAD-TAD interactions using IDR2D v1.4.0 (Krismer *et al*, 2020) with default parameters. In particular, TAD-TAD interactions with NCHG p-value > 0.01 were first filtered out, and then the odds ratio was used as the ranking statistic for IDR analysis, with the final filter criteria being IDR p-value < 0.01. Treating significant TAD-TAD interactions as edges of a graph, cliques were identified using the max_cliques function from R library igraph v1.2.6 (Csardi & Nepusz, 2006). The over-representation of A-A vs B-B clique interactions was compared against an expected value based on the proportion of A vs B TADs across all TADs, with the identity of compartment assignment of TADs based on having more 25 kb bins labelled as one compartment versus the other. Confidence intervals were derived from bootstrapping the set of clique interactions. The degree of TAD boundary conservation was evaluated using a permutation test, where the number of boundaries being shared across cell types was compared against a background derived from merging the list of boundaries and shuffling cell type labels. Additionally, 9 other TAD identification algorithms (An *et al*, 2019; Cresswell *et al*, 2020; Dali *et al*, 2018; Levy-Leduc *et al*, 2014; Matthey-Doret *et al*, 2020; Rao *et al.*, 2014; Shin *et al*, 2016; Soler-Vila *et al*, 2020; Xing *et al*, 2021) were used with default parameters to validate trends observed with insulation scores, all at 50 kb resolution.

Histone mass spectrometry analysis

Single histone modification abundances are summed from their individual occurrences as well as co-occurrences (e.g., H3K27me3 = H3K27me3 + H3K27me3&H3K36me1 + H3K27me3&H3K36me2 + H3K27me3&H3K36me3). PCA of these relative abundance measures for all quantifiable H3 modifications (at least one sample exhibiting abundance >0.1%) were used as input for PCA using the prcomp function from the R library stats v4.0.3 with default parameters to assess epigenome-wide tendencies. Abundance measures were further Z-score transformed for hierarchical clustering using the hclust function from R library stats v4.0.3 with default parameters.

Normalization of epigenetic signals

Histone mass spectrometry-derived abundances were used to scale corresponding ChIP-seq tracks by directly multiplying the library-size normalized (counts/million mapped reads) values with the relative abundance. For targets lacking mass spectrometry data (e.g., transcription factors), we applied S3V2-IDEAS commit b7cc2d5 (Xiang *et al*, 2021) to derive scaling factors using default parameters at a bin size of 200 bp.

ATAC-seq analysis

The union set of peaks across all cell types was taken as features against which reads were counted, and the resulting count matrix was further normalized via FPKM to account for variations in peak widths and sequence depth. PCA was then performed on the 10000 most variable peaks to assess global accessome trends. The 2000 most variable peaks were additionally clustered by using the hclust function from R library stats v4.0.3 with default parameters; visual inspection of the resulting dendrogram suggested 7 as a reasonable number of clusters for cutting. Global openness was assessed by first fitting a two-component gaussian mixture model to the log2(FPKM + 1) distribution across the union peak set and then assessing the number of sites exceeding the higher component's mean versus those below the lower component's mean.

Motif enrichment analysis

Over-representation of known transcription factor motifs was assessed in an ensemble manner by combining multiple frameworks (e.g., HOMER, MEME) as implemented in GimmeMotifs v0.15.3 (Bruse & Heeringen, 2018) using default options. Differential enrichment of motifs between different region sets (e.g., open sites with distinct chromatin states) was examined using the maelstrom module of GimmeMotifs with default options.

Enhancer-promoter pairing

Cis-regulatory elements were associated with putative target genes using "activity-by-contact" (ABC) commit 7fd69b0 (Fulco *et al.*, 2019). KR-normalized

matrices at 5 kb resolution were combined with H3K27ac and ATAC-seq data to calculate ABC scores quantile-normalized to K562 data, after which a stringent cut-off of 0.02 was applied — corresponding to 70% recall and 60% precision based on previous CRISPRi-FlowFISH validation (Fulco *et al.*, 2019). Alternatively, enhancer-promoter pairs identified based on co-regulated NET-CAGE tag clusters, as described above, were assessed for their degree of coordination. Specifically, a permutation test was used to compare the number of co-expressed (>1 TPM in a specific cell type) enhancer-promoter pairs versus that of background sets generated by sampling from all tag clusters. Differential interactions between enhancer-promoter pairs identified by ABC scores were investigated using R library HiCDCPlus v0.99.12 (Sahin *et al*, 2021) using default parameters at 10 kb resolution. The degree of coordinated differential promoter interaction and differential expression was quantified through the application of RRHO2 v1.0 (Cahill *et al*, 2018) to gene lists ranked by DESeq2 test statistics; for promoters involved in multiple ABC E-P pairs, the mean test statistic was used for ranking.

ChIP-seq analysis

The domain size distributions of histone modifications were determined using MCORE (Molitor *et al*, 2017) with the maximum shift size set to the chromosome lengths and other parameters kept at their defaults. Resulting cross-correlation values between replicates were averaged using a cubic spline via the function smooth.spline from R library stats v4.0.3 with default parameters, after which Gardner transformations were applied to decompose the decay spectrum into component exponential functions corresponding to different domain sizes and quantify their contribution. Differential ChIP-seq analysis was performed using DiffBind (Ross-Innes *et al*, 2012) for targets with narrow signals and csaw for broad ones. DiffBind v3.0.13 was applied with union peak sets resized to 500 bp around the summits of MACS peak calls and other options kept at their defaults using both edgeR (Robinson *et al*, 2010) and DESeq2 (Love *et al*, 2014) for the underlying statistical framework, after which only concordant results were retained (e.g., up-regulated with both methods). Unless otherwise stated, "constitutive"/"conserved" peaks refer to the intersection of MACS peak calls between cell types. csaw v1.24.3 (Lun & Smyth, 2016) was applied with default settings with edgeR as the underlying statistical framework at both a coarse (2 kbp windows with a 500 bp step size for H3K27me3; 10 kbp windows with a 2 kbp step size for H3K9me2) and a fine resolution (500 bp windows with a 100 bp step size for H3K27me3; 1 kb windows with a 200 bp step size for H3K9me2), after which the results were consolidated, allowing for a gap size of 100 bp. The domain expansion/contraction kinetics were characterized using ChromTime commit a332dbb (Fiziev & Ernst, 2018) with default settings in broad mode, with a post-hoc filter applied to exclude regions <10 kb. Aggregate plots were generated using the module computeMatrix from deepTools v3.5.0 with default options, in scale-regions mode for domains and

reference-point mode for focal features such as peaks. Differential H3K9me3 promoters (+/- 1kb from TSS) were defined using the mass spectrometry-derived coefficient-normalized log2-transformed FPKM signal with the threshold (log2(FPKM) >1 in either cell type and log2(FPKM) difference >1).

Epigenome-based clustering of cis-regulatory elements

The log2(enrichment over input) values of ChIP-seq signals and log2(FPKM + 1) for ATAC-seq signals in promoters (+/- 2.5kb from TSS) or reproducible accessible sites identified using ChromA v2.1.1 (Gabitto *et al*, 2020) (resized to +/- 500 bp surrounding the summit) were used as input for dimension reduction through UMAP v0.5.1 (Mcinnes *et al*, 2018) and subsequently clustered through HDBSCAN v0.8.27 (Campello *et al*, 2013). For UMAP, manhattan distances were used for promoters and correlation distances for open sites; a grid search over min_dist of [0.0, 0.01, 0.1], n_neighbors of [15, 30, 50] and n_components of 2–10 were all subjected to HDBSCAN clustering to identify epigenetically distinct clusters via visual inspection. For HDBSCAN, a grid search over min_cluster_size and min_samples over [50, 100, 200, 500, 1000, 2000, 5000, 10000] were tested. In a semi-supervised fashion, individual clusters were isolated and subjected to further sub-clustering until the embedding no longer exhibited distinct segregation of data points for any individual epigenetic signal.

Pathway enrichment analysis

Associations of specific gene lists with particular biological pathways were evaluated using the gost function from R library gprofiler2 v0.2.0 (Kolberg *et al*, 2020) with default options. The enrichment of pathways towards the extremes of ranked gene lists, on the other hand, was assessed using the fgseaMultilevel function from R library fgsea 1.17.1 (Korotkevich *et al*) with the boundary parameter eps set to 0 and others kept at their default values; redundant terms were collapsed by using collapsePathways with an adjusted p-value threshold of 0.05. To obtain gene lists ranked by multiple metrics (e.g., differential expression and promoter interaction), the mean test statistic was used to rank genes independently for each metric, and an aggregated ranking was then obtained using p-values produced by the aggregateRanks function from R library RobustRankAggreg v1.1 (Kolde *et al*, 2012).

Overlap enrichment analysis

The overlap between genomic regions and annotated intervals was examined using Fisher's exact tests as implemented in the R library LOLA v1.19.1 (Sheffield & Bock, 2016). Ensembl Regulatory build annotations v20180516 were sourced directly from Ensembl; RepeatMasker annotations were obtained from the rmsk table hosted on the UCSC Genome Browser. ENCODE cCRE annotations were downloaded from SCREEN v13 (http://screen.encodeproject.org/).

Pile-up analysis

Interaction between specific regions (e.g., promoters of a similar chromatin state) were quantified using the ObsExpSnipper function from cooltools v0.4.0 with default parameters and using the aforementioned diagonal-wise expected values. For pile-up of domains (e.g., TADs or broad H3K9me3 domains) rescaled to the same size, coolpup.py v0.9.7 (Flyamer *et al*, 2020) was used with the option --rescale and optionally --local when assessing on-diagonal patterns, and with all other options kept at their defaults.

Lamin B1-related analysis

EDD v1.1.19 (Lund *et al*, 2014) was used to identify lamina-associated domains from lamin B1 ChIP-seq with a bin size of 10 kb, gap penalty set to 20, and all others options kept at their defaults. LADetector v8122016 (Harr *et al.*, 2015) was used instead for lamin B1 DamID, with a bin size of 10 kb and max dip size of 25 kb. Generalized linear models with 50 basis functions were used to visualize chromosome-scale patterns using REML for smoothness selection as implemented in the gam function of R library mgcv v1.8-31 (Wood, 2011).

Partially methylated domains-related analysis

PMDs were identified by calculating median mCG/CG values using a 100 kb sliding window and identifying those falling below 85%; after merging adjacent regions, those wider than 500 kb were called as PMDs. The binary status of whether a bin falls within a GSC PMD or not was modelled using three methods: (1) gradient boosted tree (gbm), (2) neural network (nnet), and (3) elastic net (glmnet), each with 10x10 cross validation using a 70/30 train/test split as implemented in the R library caret v6.0-86 (Kuhn, 2008). Model performance for predicting PMDs was then assessed on the held-out test set using the roc function from R library pROC v1.16.2 (Robin *et al*, 2011).

Mapping to the Y chromosome

Ampliconic sequences on the murine Y chromosome were retrieved from an earlier report describing its assembly (Soh *et al.*, 2014), and were directly used as the reference for alignment. Otherwise, data was processed as described in "PBAT data processing".

Statistical considerations

P-values were mapped to symbols as follows: 0 (****) 0.0001 (***) 0.001 (**) 0.01 (*) 0.05 (ns) 1. Wilcoxon rank-sum tests and T-tests were carried out using the functions wilcox.test and t.test, respectively, from the R library stats v4.0.3. Bootstrap confidence intervals were computed using the function boot with 100000 replicates followed by boot.ci from the R library boot 1.3-28 (Davison & Hinkley, 1997) using default options. For all box plots (i.e., box-and-whiskers plots), the lower and upper hinge correspond to

the first and third quartile, and the upper whiskers extend to the largest value % 1.5 * IQR and vice versa for the lower whiskers.

Data Availability

The accession number for all the sequencing data generated in this study is GSE183828 (https://www.ncbi.nlm.nih.gov/geo/query/acc.cgi?acc=GSE183828) (the GEO database). Scripts used to generate the presented results and additional raw data underlying figures are available at https://github.com/bhu/germ_nucleome.

REFERENCES

Abdennur N, Mirny LA (2020) Cooler: scalable storage for Hi-C data and other genomically labeled arrays. *Bioinformatics* 36: 311-316

Alavattam KG, Maezawa S, Sakashita A, Khoury H, Barski A, Kaplan N, Namekawa SH (2019) Attenuated chromatin compartmentalization in meiosis and its maturation in sperm development. *Nat Struct Mol Biol* 26: 175-184

Amemiya HM, Kundaje A, Boyle AP (2019) The ENCODE Blacklist: Identification of Problematic Regions of the Genome. *Scientific reports* 9: 9354

An L, Yang T, Yang J, Nuebler J, Xiang G, Hardison RC, Li Q, Zhang Y (2019) OnTAD: hierarchical domain structure reveals the divergence of activity among TADs and boundaries. *Genome Biol* 20: 282

Anton T, Bultmann S, Leonhardt H, Markaki Y (2014) Visualization of specific DNA sequences in living mouse embryonic stem cells with a programmable fluorescent CRISPR/Cas system. *Nucleus* 5: 163-172

Battulin N, Fishman VS, Mazur AM, Pomaznoy M, Khabarova AA, Afonnikov DA, Prokhortchouk EB, Serov OL (2015) Comparison of the three-dimensional organization of sperm and fibroblast genomes using the Hi-C approach. *Genome Biol* 16: 77

Belaghzal H, Dekker J, Gibcus JH (2017) Hi-C 2.0: An optimized Hi-C procedure for high-resolution genome-wide mapping of chromosome conformation. *Methods* 123: 56-65

Bian Q, Khanna N, Alvikas J, Belmont AS (2013) beta-Globin cis-elements determine differential nuclear targeting through epigenetic modifications. *J Cell Biol* 203: 767-783

Bonev B, Mendelson Cohen N, Szabo Q, Fritsch L, Papadopoulos GL, Lubling Y, Xu X, Lv X, Hugnot JP, Tanay A *et al* (2017) Multiscale 3D Genome Rewiring during Mouse Neural Development. *Cell* 171: 557-572 e524

Borgel J, Guibert S, Li Y, Chiba H, Schubeler D, Sasaki H, Forne T, Weber M (2010) Targets and dynamics of promoter DNA methylation during early mouse development. *Nat Genet* 42: 1093-1100

Boroviak T, Loos R, Bertone P, Smith A, Nichols J (2014) The ability of inner-cell-mass cells to self-renew as embryonic stem cells is acquired following epiblast specification. *Nat Cell Biol* 16: 516-528

Bourque G, Leong B, Vega VB, Chen X, Lee YL, Srinivasan KG, Chew JL, Ruan Y, Wei CL, Ng HH *et al* (2008) Evolution of the mammalian transcription factor binding

repertoire via transposable elements. *Genome Res* 18: 1752-1762

Bruse N, Heeringen SJV (2018) GimmeMotifs: an analysis framework for transcription factor motif analysis. *bioRxiv*: https://doi.org/10.1101/474403

Buenrostro JD, Giresi PG, Zaba LC, Chang HY, Greenleaf WJ (2013) Transposition of native chromatin for fast and sensitive epigenomic profiling of open chromatin, DNA-binding proteins and nucleosome position. *Nat Methods* 10: 1213-1218

Cahill KM, Huo Z, Tseng GC, Logan RW, Seney ML (2018) Improved identification of concordant and discordant gene expression signatures using an updated rank-rank hypergeometric overlap approach. *Scientific reports* 8: 9588

Campello R, Moulavi D, Sander J (2013) Density-Based Clustering Based on Hierarchical Density Estimates. In: *Advances in Knowledge Discovery and Data Mining*, pp. 160-172. Springer:

Chen S, Zhou Y, Chen Y, Gu J (2018) fastp: an ultra-fast all-in-one FASTQ preprocessor. *Bioinformatics* 34: i884-i890

Chen X, Yammine S, Shi C, Tark-Dame M, Gondor A, Ohlsson R (2014) The visualization of large organized chromatin domains enriched in the H3K9me2 mark within a single chromosome in a single cell. *Epigenetics* 9: 1439-1445

Corces MR, Trevino AE, Hamilton EG, Greenside PG, Sinnott-Armstrong NA, Vesuna S, Satpathy AT, Rubin AJ, Montine KS, Wu B *et al* (2017) An improved ATAC-seq protocol reduces background and enables interrogation of frozen tissues. *Nat Methods* 14: 959-962

Cresswell KG, Stansfield JC, Dozmorov MG (2020) SpectralTAD: an R package for defining a hierarchy of topologically associated domains using spectral clustering. *BMC Bioinformatics* 21: 319

Csardi G, Nepusz T (2006) The igraph software package for complex network research. *InterJournal, Complex Systems* 1695

Cuadrado A, Gimenez-Llorente D, Kojic A, Rodriguez-Corsino M, Cuartero Y, Martin-Serrano G, Gomez-Lopez G, Marti-Renom MA, Losada A (2019) Specific Contributions of Cohesin-SA1 and Cohesin-SA2 to TADs and Polycomb Domains in Embryonic Stem Cells. *Cell reports* 27: 3500-3510 e3504

D'Oliveira Albanus R, Kyono Y, Hensley J, Varshney A, Orchard P, Kitzman JO, Parker SCJ (2021) Chromatin information content landscapes inform transcription factor and DNA interactions. *Nat Commun* 12: 1307

Dali R, Bourque G, Blanchette M (2018) RobusTAD: A Tool for Robust Annotation of Topologically Associating Domain Boundaries. *bioRxiv*: https://doi.org/10.1101/293175

Davison AC, Hinkley DV (1997) *Boostrap methods and their application*. Cambridge University Press

Dekker J, Belmont AS, Guttman M, Leshyk VO, Lis JT, Lomvardas S, Mirny LA, O'Shea CC, Park PJ, Ren B *et al* (2017) The 4D nucleome project. *Nature* 549: 219-226

Di Giammartino DC, Kloetgen A, Polyzos A, Liu Y, Kim D, Murphy D, Abuhashem A, Cavaliere P, Aronson B, Shah V *et al* (2019) KLF4 is involved in the organization and regulation of pluripotency-associated three-dimensional enhancer networks. *Nat Cell Biol* 21: 1179-1190

Dimmick MC, Lee LJ, Frey BJ HiCSR: a Hi-C super-resolution framework for producing highly realistic contact maps. *Bioinformatics*

Dobin A, Davis CA, Schlesinger F, Drenkow J, Zaleski C, Jha S, Batut P, Chaisson M, Gingeras TR (2013) STAR: ultrafast universal RNA-seq aligner. *Bioinformatics* 29: 15-21

Du Z, Zheng H, Huang B, Ma R, Wu J, Zhang X, He J, Xiang Y, Wang Q, Li Y *et al* (2017) Allelic reprogramming of 3D chromatin architecture during early mammalian development. *Nature* 547: 232-235

Du Z, Zheng H, Kawamura YK, Zhang K, Gassler J, Powell S, Xu Q, Lin Z, Xu K, Zhou Q *et al* (2020) Polycomb Group Proteins Regulate Chromatin Architecture in Mouse Oocytes and Early Embryos. *Mol Cell* 77: 825-839 e827

Durand NC, Shamim MS, Machol I, Rao SS, Huntley MH, Lander ES, Aiden EL (2016) Juicer Provides a One-Click System for Analyzing Loop-Resolution Hi-C Experiments. *Cell Syst* 3: 95-98

Evans EP, Ford CE, Lyon MF (1977) Direct evidence of the capacity of the XY germ cell in the mouse to become an oocyte. *Nature* 267: 430-431

Farhangdoost N, Horth C, Hu B, Bareke E, Chen X, Li Y, Coradin M, Garcia BA, Lu C, Majewski J (2021) Chromatin dysregulation associated with NSD1 mutation in head and neck squamous cell carcinoma. *Cell reports* 34: 108769

Fiziev P, Ernst J (2018) ChromTime: modeling spatio-temporal dynamics of chromatin marks. *Genome Biol* 19: 109

Flyamer IM, Gassler J, Imakaev M, Brandao HB, Ulianov SV, Abdennur N, Razin SV, Mirny LA, Tachibana-Konwalski K (2017) Single-nucleus Hi-C reveals unique

chromatin reorganization at oocyte-to-zygote transition. *Nature* 544: 110-114

Flyamer IM, Illingworth RS, Bickmore WA (2020) Coolpup.py: versatile pile-up analysis of Hi-C data. *Bioinformatics* 36: 2980-2985

Fukuda K, Shimura C, Miura H, Tanigawa A, Suzuki T, Dohmae N, Hiratani I, Shinkai Y (2021) Regulation of mammalian 3D genome organization and histone H3K9 dimethylation by H3K9 methyltransferases. *Commun Biol* 4: 571

Fulco CP, Nasser J, Jones TR, Munson G, Bergman DT, Subramanian V, Grossman SR, Anyoha R, Doughty BR, Patwardhan TA *et al* (2019) Activity-by-contact model of enhancer-promoter regulation from thousands of CRISPR perturbations. *Nat Genet* 51: 1664-1669

Gabitto MI, Rasmussen A, Wapinski O, Allaway K, Carriero N, Fishell GJ, Bonneau R (2020) Characterizing chromatin landscape from aggregate and single-cell genomic assays using flexible duration modeling. *Nat Commun* 11: 747

Gorkin DU, Barozzi I, Zhao Y, Zhang Y, Huang H, Lee AY, Li B, Chiou J, Wildberg A, Ding B *et al* (2020) An atlas of dynamic chromatin landscapes in mouse fetal development. *Nature* 583: 744-751

Griswold MD (2016) Spermatogenesis: The Commitment to Meiosis. *Physiol Rev* 96: 1-17

Guelen L, Pagie L, Brasset E, Meuleman W, Faza MB, Talhout W, Eussen BH, de Klein A, Wessels L, de Laat W *et al* (2008) Domain organization of human chromosomes revealed by mapping of nuclear lamina interactions. *Nature* 453: 948-951

Guenatri M, Bailly D, Maison C, Almouzni G (2004) Mouse centric and pericentric satellite repeats form distinct functional heterochromatin. *J Cell Biol* 166: 493-505

Gurdon JB, Wilmut I (2011) Nuclear transfer to eggs and oocytes. *Cold Spring Harb Perspect Biol* 3

Haberle V, Forrest AR, Hayashizaki Y, Carninci P, Lenhard B (2015) CAGEr: precise TSS data retrieval and high-resolution promoterome mining for integrative analyses. *Nucleic Acids Res* 43: e51

Hansen KD, Timp W, Bravo HC, Sabunciyan S, Langmead B, McDonald OG, Wen B, Wu H, Liu Y, Diep D *et al* (2011) Increased methylation variation in epigenetic domains across cancer types. *Nat Genet* 43: 768-775

Harr JC, Luperchio TR, Wong X, Cohen E, Wheelan SJ, Reddy KL (2015) Directed targeting of chromatin to the nuclear lamina is mediated by chromatin state and A-type

lamins. *J Cell Biol* 208: 33-52

Hayashi K, Ohta H, Kurimoto K, Aramaki S, Saitou M (2011) Reconstitution of the mouse germ cell specification pathway in culture by pluripotent stem cells. *Cell* 146: 519-532

Hirabayashi S, Bhagat S, Matsuki Y, Takegami Y, Uehata T, Kanemaru A, Itoh M, Shirakawa K, Takaori-Kondo A, Takeuchi O *et al* (2019) NET-CAGE characterizes the dynamics and topology of human transcribed cis-regulatory elements. *Nat Genet* 51: 1369-1379

Hon GC, Hawkins RD, Caballero OL, Lo C, Lister R, Pelizzola M, Valsesia A, Ye Z, Kuan S, Edsall LE *et al* (2012) Global DNA hypomethylation coupled to repressive chromatin domain formation and gene silencing in breast cancer. *Genome Res* 22: 246-258

Ishikura Y, Ohta H, Sato T, Murase Y, Yabuta Y, Kojima Y, Yamashiro C, Nakamura T, Yamamoto T, Ogawa T *et al* (2021) In vitro reconstitution of the whole male germ-cell development from mouse pluripotent stem cells. *Cell Stem Cell* 28: 2167-2179 e2169

Ishikura Y, Yabuta Y, Ohta H, Hayashi K, Nakamura T, Okamoto I, Yamamoto T, Kurimoto K, Shirane K, Sasaki H *et al* (2016) In Vitro Derivation and Propagation of Spermatogonial Stem Cell Activity from Mouse Pluripotent Stem Cells. *Cell reports* 17: 2789-2804

Jameson SA, Natarajan A, Cool J, DeFalco T, Maatouk DM, Mork L, Munger SC, Capel B (2012) Temporal transcriptional profiling of somatic and germ cells reveals biased lineage priming of sexual fate in the fetal mouse gonad. *PLoS Genet* 8: e1002575

Johnstone SE, Reyes A, Qi Y, Adriaens C, Hegazi E, Pelka K, Chen JH, Zou LS, Drier Y, Hecht V *et al* (2020) Large-Scale Topological Changes Restrain Malignant Progression in Colorectal Cancer. *Cell* 182: 1474-1489 e1423

Kanatsu-Shinohara M, Inoue K, Lee J, Yoshimoto M, Ogonuki N, Miki H, Baba S, Kato T, Kazuki Y, Toyokuni S *et al* (2004) Generation of pluripotent stem cells from neonatal mouse testis. *Cell* 119: 1001-1012

Kanatsu-Shinohara M, Ogonuki N, Inoue K, Miki H, Ogura A, Toyokuni S, Shinohara T (2003) Long-term proliferation in culture and germline transmission of mouse male germline stem cells. *Biol Reprod* 69: 612-616

Karimi MM, Goyal P, Maksakova IA, Bilenky M, Leung D, Tang JX, Shinkai Y, Mager DL, Jones S, Hirst M *et al* (2011) DNA methylation and SETDB1/H3K9me3 regulate

predominantly distinct sets of genes, retroelements, and chimeric transcripts in mESCs. *Cell Stem Cell* 8: 676-687

Ke Y, Xu Y, Chen X, Feng S, Liu Z, Sun Y, Yao X, Li F, Zhu W, Gao L *et al* (2017) 3D Chromatin Structures of Mature Gametes and Structural Reprogramming during Mammalian Embryogenesis. *Cell* 170: 367-381 e320

Keough KC, Shah PP, Gjoni K, Santini GT, Wickramasinghe NM, Dundes CE, Karnay A, Chen A, Salomon REA, Walsh PJ *et al* (2021) An atlas of lamina-associated chromatin across twelve human cell types reveals an intermediate chromatin subtype. *bioRxiv*

Kolberg L, Raudvere U, Kuzmin I, Vilo J, Peterson H (2020) gprofiler2 -- an R package for gene list functional enrichment analysis and namespace conversion toolset g:Profiler. *F1000Res* 9

Kolde R, Laur S, Adler P, Vilo J (2012) Robust rank aggregation for gene list integration and meta-analysis. *Bioinformatics* 28: 573-580

Korotkevich G, Sukhov V, Budin N, Shpak B, Artyomov MN, Sergushichev A Fast gene set enrichment analysis.

Krismer K, Guo Y, Gifford DK (2020) IDR2D identifies reproducible genomic interactions. *Nucleic Acids Res* 48: e31

Krueger F, Andrews SR (2011) Bismark: a flexible aligner and methylation caller for Bisulfite-Seq applications. *Bioinformatics* 27: 1571-1572

Krueger F, James F, Ewels P, Afyounian E, Schuster-Boeckler B (2021) FelixKrueger/TrimGalore: v0.6.7. Zenodo.

Kruse K, Hug CB, Vaquerizas JM (2020) FAN-C: a feature-rich framework for the analysis and visualisation of chromosome conformation capture data. *Genome Biol* 21: 303

Kubo N, Toh H, Shirane K, Shirakawa T, Kobayashi H, Sato T, Sone H, Sato Y, Tomizawa S, Tsurusaki Y *et al* (2015) DNA methylation and gene expression dynamics during spermatogonial stem cell differentiation in the early postnatal mouse testis. *BMC Genomics* 16: 624

Kuhn M (2008) Building Predictive Models in R Using the caret Package. *J Stat Soft* 28: 1-26

Kurimoto K, Yabuta Y, Hayashi K, Ohta H, Kiyonari H, Mitani T, Moritoki Y, Kohri K, Kimura H, Yamamoto T *et al* (2015) Quantitative Dynamics of Chromatin Remodeling

during Germ Cell Specification from Mouse Embryonic Stem Cells. *Cell Stem Cell* 16: 517-532

Langmead B, Salzberg SL (2012) Fast gapped-read alignment with Bowtie 2. *Nat Methods* 9: 357-359

Lee HJ, Hore TA, Reik W (2014) Reprogramming the methylome: erasing memory and creating diversity. *Cell Stem Cell* 14: 710-719

Lee TI, Johnstone SE, Young RA (2006) Chromatin immunoprecipitation and microarray-based analysis of protein location. *Nature protocols* 1: 729-748

Levy-Leduc C, Delattre M, Mary-Huard T, Robin S (2014) Two-dimensional segmentation for analyzing Hi-C data. *Bioinformatics* 30: i386-392

Li H, Handsaker B, Wysoker A, Fennell T, Ruan J, Homer N, Marth G, Abecasis G, Durbin R, Genome Project Data Processing S (2009) The Sequence Alignment/Map format and SAMtools. *Bioinformatics* 25: 2078-2079

Lin D, Sanders J, Noble WS (2021) HiCRep.py : Fast comparison of Hi-C contact matrices in Python. *Bioinformatics*

Lister R, Pelizzola M, Dowen RH, Hawkins RD, Hon G, Tonti-Filippini J, Nery JR, Lee L, Ye Z, Ngo QM *et al* (2009) Human DNA methylomes at base resolution show widespread epigenomic differences. *Nature* 462: 315-322

Liu Y, Nanni L, Sungalee S, Zufferey M, Tavernari D, Mina M, Ceri S, Oricchio E, Ciriello G (2021) Systematic inference and comparison of multi-scale chromatin sub-compartments connects spatial organization to cell phenotypes. *Nat Commun* 12: 2439

Love MI, Huber W, Anders S (2014) Moderated estimation of fold change and dispersion for RNA-seq data with DESeq2. *Genome Biol* 15: 550

Lun AT, Smyth GK (2016) csaw: a Bioconductor package for differential binding analysis of ChIP-seq data using sliding windows. *Nucleic Acids Res* 44: e45

Lund E, Oldenburg AR, Collas P (2014) Enriched domain detector: a program for detection of wide genomic enrichment domains robust against local variations. *Nucleic Acids Res* 42: e92

Luo Z, Wang X, Jiang H, Wang R, Chen J, Chen Y, Xu Q, Cao J, Gong X, Wu J *et al* (2020) Reorganized 3D Genome Structures Support Transcriptional Regulation in Mouse Spermatogenesis. *iScience* 23: 101034

Marchal C, Singh N, Corso-Díaz X, Swaroop A (2022) HiCRes: a computational

method to estimate and predict the resolution of HiC libraries. *Nucleic Acids Res* 50: e35

Marks H, Kalkan T, Menafra R, Denissov S, Jones K, Hofemeister H, Nichols J, Kranz A, Francis Stewart A, Smith A *et al* (2012) The transcriptional and epigenomic foundations of ground state pluripotency. *Cell* 149: 590-604

Martin M (2011) Cutadapt removes adapter sequences from high-throughput sequencing reads. *EMBnetjournal* 17: 10

Matthey-Doret C, Baudry L, Breuer A, Montagne R, Guiglielmoni N, Scolari V, Jean E, Campeas A, Chanut PH, Oriol E *et al* (2020) Computer vision for pattern detection in chromosome contact maps. *Nat Commun* 11: 5795

Mcinnes L, Healy J, Saul N, Großberger L (2018) UMAP: Uniform Manifold Approximation and Projection. *Journal of Open Source Software* 3: 861

Miura K (2020) Measurements of Intensity Dynamics at the Periphery of the Nucleus. In: *Bioimage Data Analysis Workflows*, pp. 9-32. Springer International Publishing:

Miyauchi H, Ohta H, Nagaoka S, Nakaki F, Sasaki K, Hayashi K, Yabuta Y, Nakamura T, Yamamoto T, Saitou M (2017) Bone morphogenetic protein and retinoic acid synergistically specify female germ-cell fate in mice. *EMBO J* 36: 3100-3119

Mochizuki K, Sharif J, Shirane K, Uranishi K, Bogutz AB, Janssen SM, Suzuki A, Okuda A, Koseki H, Lorincz MC (2021) Repression of germline genes by PRC1.6 and SETDB1 in the early embryo precedes DNA methylation-mediated silencing. *Nat Commun* 12: 7020

Molitor J, Mallm JP, Rippe K, Erdel F (2017) Retrieving Chromatin Patterns from Deep Sequencing Data Using Correlation Functions. *Biophys J* 112: 473-490

Murata M, Nishiyori-Sueki H, Kojima-Ishiyama M, Carninci P, Hayashizaki Y, Itoh M (2014) Detecting expressed genes using CAGE. *Methods Mol Biol* 1164: 67-85

Nagaoka S, I., Nakaki F, Miyauchi H, Nosaka Y, Yabuta Y, Kurimoto K, Hayashi K, Nakamura T, Yamamoto T, Saitou M (2020) ZGLP1 is a determinant for the oogenic fate in mice. *Science* 367

Ohta H, Kurimoto K, Okamoto I, Nakamura T, Yabuta Y, Miyauchi H, Yamamoto T, Okuno Y, Hagiwara M, Shirane K *et al* (2017) In vitro expansion of mouse primordial germ cell-like cells recapitulates an epigenetic blank slate. *EMBO J* 36: 1888-1907

Ohta H, Yabuta Y, Kurimoto K, Nakamura T, Murase Y, Yamamoto T, Saitou M (2021) Cyclosporin A and FGF signaling support the proliferation/survival of mouse primordial

germ cell-like cells in vitrodagger. *Biol Reprod* 104: 344-360

Ohta H, Yomogida K, Yamada S, Okabe M, Nishimune Y (2000) Real-time observation of transplanted 'green germ cells': proliferation and differentiation of stem cells. *Dev Growth Differ* 42: 105-112

Okamoto I, Arnaud D, Le Baccon P, Otte AP, Disteche CM, Avner P, Heard E (2005) Evidence for de novo imprinted X-chromosome inactivation independent of meiotic inactivation in mice. *Nature* 438: 369-373

Patel L, Kang R, Rosenberg SC, Qiu Y, Raviram R, Chee S, Hu R, Ren B, Cole F, Corbett KD (2019) Dynamic reorganization of the genome shapes the recombination landscape in meiotic prophase. *Nat Struct Mol Biol* 26: 164-174

Patro R, Duggal G, Love MI, Irizarry RA, Kingsford C (2017) Salmon provides fast and bias-aware quantification of transcript expression. *Nat Methods* 14: 417-419

Paulsen J, Liyakat Ali TM, Nekrasov M, Delbarre E, Baudement MO, Kurscheid S, Tremethick D, Collas P (2019) Long-range interactions between topologically associating domains shape the four-dimensional genome during differentiation. *Nat Genet* 51: 835-843

Paulsen J, Sekelja M, Oldenburg AR, Barateau A, Briand N, Delbarre E, Shah A, Sorensen AL, Vigouroux C, Buendia B *et al* (2017) Chrom3D: three-dimensional genome modeling from Hi-C and nuclear lamin-genome contacts. *Genome Biol* 18: 21

Peric-Hupkes D, Meuleman W, Pagie L, Bruggeman SW, Solovei I, Brugman W, Graf S, Flicek P, Kerkhoven RM, van Lohuizen M *et al* (2010) Molecular maps of the reorganization of genome-nuclear lamina interactions during differentiation. *Mol Cell* 38: 603-613

Poleshko A, Shah PP, Gupta M, Babu A, Morley MP, Manderfield LJ, Ifkovits JL, Calderon D, Aghajanian H, Sierra-Pagan JE *et al* (2017) Genome-Nuclear Lamina Interactions Regulate Cardiac Stem Cell Lineage Restriction. *Cell* 171: 573-587 e514

Poleshko A, Smith CL, Nguyen SC, Sivaramakrishnan P, Wong KG, Murray JI, Lakadamyali M, Joyce EF, Jain R, Epstein JA (2019) H3K9me2 orchestrates inheritance of spatial positioning of peripheral heterochromatin through mitosis. *Elife* 8

Polovnikov K, Belan S, Imakaev M, Brand HB, A. ML (2022) Fractal polymer with loops recapitulates key features of chromosome organization. *bioRxiv*

Quinlan AR, Hall IM (2010) BEDTools: a flexible suite of utilities for comparing genomic features. *Bioinformatics* 26: 841-842

Ramirez F, Ryan DP, Gruning B, Bhardwaj V, Kilpert F, Richter AS, Heyne S, Dundar F, Manke T (2016) deepTools2: a next generation web server for deep-sequencing data analysis. *Nucleic Acids Res* 44: W160-165

Rao SS, Huntley MH, Durand NC, Stamenova EK, Bochkov ID, Robinson JT, Sanborn AL, Machol I, Omer AD, Lander ES *et al* (2014) A 3D map of the human genome at kilobase resolution reveals principles of chromatin looping. *Cell* 159: 1665-1680

Robin X, Turck N, Hainard A, Tiberti N, Lisacek F, Sanchez JC, Muller M (2011) pROC: an open-source package for R and S+ to analyze and compare ROC curves. *BMC Bioinformatics* 12: 77

Robinson MD, McCarthy DJ, Smyth GK (2010) edgeR: a Bioconductor package for differential expression analysis of digital gene expression data. *Bioinformatics* 26: 139-140

Robson MI, de Las Heras JI, Czapiewski R, Le Thanh P, Booth DG, Kelly DA, Webb S, Kerr ARW, Schirmer EC (2016) Tissue-Specific Gene Repositioning by Muscle Nuclear Membrane Proteins Enhances Repression of Critical Developmental Genes during Myogenesis. *Mol Cell* 62: 834-847

Ross-Innes CS, Stark R, Teschendorff AE, Holmes KA, Ali HR, Dunning MJ, Brown GD, Gojis O, Ellis IO, Green AR *et al* (2012) Differential oestrogen receptor binding is associated with clinical outcome in breast cancer. *Nature* 481: 389-393

Sahin M, Wong W, Zhan Y, Van Deynze K, Koche R, Leslie CS (2021) HiC-DC+ enables systematic 3D interaction calls and differential analysis for Hi-C and HiChIP. *Nat Commun* 12: 3366

Saitou M, Hayashi K (2021) Mammalian in vitro gametogenesis. *Science* 374: eaaz6830

Salhab A, Nordstrom K, Gasparoni G, Kattler K, Ebert P, Ramirez F, Arrigoni L, Muller F, Polansky JK, Cadenas C *et al* (2018) A comprehensive analysis of 195 DNA methylomes reveals shared and cell-specific features of partially methylated domains. *Genome Biol* 19: 150

Sanulli S, Trnka MJ, Dharmarajan V, Tibble RW, Pascal BD, Burlingame AL, Griffin PR, Gross JD, Narlikar GJ (2019) HP1 reshapes nucleosome core to promote phase separation of heterochromatin. *Nature* 575: 390-394

Sasaki K, Yokobayashi S, Nakamura T, Okamoto I, Yabuta Y, Kurimoto K, Ohta H, Moritoki Y, Iwatani C, Tsuchiya H *et al* (2015) Robust In Vitro Induction of Human Germ Cell Fate from Pluripotent Stem Cells. *Cell Stem Cell* 17: 178-194

Schroeder DI, Blair JD, Lott P, Yu HO, Hong D, Crary F, Ashwood P, Walker C, Korf I, Robinson WP *et al* (2013) The human placenta methylome. *Proc Natl Acad Sci U S A* 110: 6037-6042

Schwarzer W, Abdennur N, Goloborodko A, Pekowska A, Fudenberg G, Loe-Mie Y, Fonseca NA, Huber W, Haering CH, Mirny L *et al* (2017) Two independent modes of chromatin organization revealed by cohesin removal. *Nature* 551: 51-56

Seisenberger S, Andrews S, Krueger F, Arand J, Walter J, Santos F, Popp C, Thienpont B, Dean W, Reik W (2012) The dynamics of genome-wide DNA methylation reprogramming in mouse primordial germ cells. *Mol Cell* 48: 849-862

Sheffield NC, Bock C (2016) LOLA: enrichment analysis for genomic region sets and regulatory elements in R and Bioconductor. *Bioinformatics* 32: 587-589

Shin H, Shi Y, Dai C, Tjong H, Gong K, Alber F, Zhou XJ (2016) TopDom: an efficient and deterministic method for identifying topological domains in genomes. *Nucleic Acids Res* 44: e70

Shirane K, Kurimoto K, Yabuta Y, Yamaji M, Satoh J, Ito S, Watanabe A, Hayashi K, Saitou M, Sasaki H (2016) Global Landscape and Regulatory Principles of DNA Methylation Reprogramming for Germ Cell Specification by Mouse Pluripotent Stem Cells. *Dev Cell* 39: 87-103

Shirane K, Miura F, Ito T, Lorincz MC (2020) NSD1-deposited H3K36me2 directs de novo methylation in the mouse male germline and counteracts Polycomb-associated silencing. *Nat Genet* 52: 1088-1098

Sidoli S, Bhanu NV, Karch KR, Wang X, Garcia BA (2016) Complete Workflow for Analysis of Histone Post-translational Modifications Using Bottom-up Mass Spectrometry: From Histone Extraction to Data Analysis. *Journal of Visualized Experiments*

Soh YQ, Alfoldi J, Pyntikova T, Brown LG, Graves T, Minx PJ, Fulton RS, Kremitzki C, Koutseva N, Mueller JL *et al* (2014) Sequencing the mouse Y chromosome reveals convergent gene acquisition and amplification on both sex chromosomes. *Cell* 159: 800-813

Soler-Vila P, Cusco P, Farabella I, Di Stefano M, Marti-Renom MA (2020) Hierarchical chromatin organization detected by TADpole. *Nucleic Acids Res* 48: e39

Soneson C, Love MI, Robinson MD (2015) Differential analyses for RNA-seq: transcript-level estimates improve gene-level inferences. *F1000Res* 4: 1521

Spiller C, Koopman P, Bowles J (2017) Sex Determination in the Mammalian Germline. *Annu Rev Genet* 51: 265-285

Stadhouders R, Vidal E, Serra F, Di Stefano B, Le Dily F, Quilez J, Gomez A, Collombet S, Berenguer C, Cuartero Y *et al* (2018) Transcription factors orchestrate dynamic interplay between genome topology and gene regulation during cell reprogramming. *Nat Genet* 50: 238-249

Stovner EB, Saetrom P (2019) epic2 efficiently finds diffuse domains in ChIP-seq data. *Bioinformatics* 35: 4392-4393

Surani MA, Hayashi K, Hajkova P (2007) Genetic and epigenetic regulators of pluripotency. *Cell* 128: 747-762

Tang WW, Kobayashi T, Irie N, Dietmann S, Surani MA (2016) Specification and epigenetic programming of the human germ line. *Nat Rev Genet* 17: 585-600

Thodberg M, Thieffry A, Vitting-Seerup K, Andersson R, Sandelin A (2019) CAGEfightR: analysis of 5'-end data using R/Bioconductor. *BMC Bioinformatics* 20: 487

Todd S, Todd P, McGowan SJ, Hughes JR, Kakui Y, Leymarie FF, Latham W, Taylor S (2021) CSynth: an interactive modelling and visualization tool for 3D chromatin structure. *Bioinformatics* 37: 951-955

Vara C, Paytuvi-Gallart A, Cuartero Y, Le Dily F, Garcia F, Salva-Castro J, Gomez HL, Julia E, Moutinho C, Aiese Cigliano R *et al* (2019) Three-Dimensional Genomic Structure and Cohesin Occupancy Correlate with Transcriptional Activity during Spermatogenesis. *Cell reports* 28: 352-367 e359

Venev S, Abdennur N, Goloborodko A, Flyamer I, Fudenberg G, Nuebler J, Galitsyna A, Akgol B, Abraham S, Kerpedjiev P *et al* (2021) open2c/cooltools: v0.4.1. Zenodo.

Wang J, Chakraborty A, Ay F (2021) dcHiC: differential compartment analysis of Hi-C datasets. *bioRxiv*: https://doi.org/10.1101/2021.1102.1102.429297

Wang Y, Wang H, Zhang Y, Du Z, Si W, Fan S, Qin D, Wang M, Duan Y, Li L *et al* (2019) Reprogramming of Meiotic Chromatin Architecture during Spermatogenesis. *Mol Cell* 73: 547-561 e546

Wen L, Tang F (2019) Human Germline Cell Development: from the Perspective of Single-Cell Sequencing. *Mol Cell* 76: 320-328

Western PS, Miles DC, van den Bergen JA, Burton M, Sinclair AH (2008) Dynamic regulation of mitotic arrest in fetal male germ cells. *Stem Cells* 26: 339-347

Wingett S, Ewels P, Furlan-Magaril M, Nagano T, Schoenfelder S, Fraser P, Andrews S (2015) HiCUP: pipeline for mapping and processing Hi-C data. *F1000Res* 4: 1310

Wood SN (2011) Fast stable restricted maximum likelihood and marginal likelihood estimation of semiparametric generalized linear models. *J R Statist Soc B* 73: 3-36

Wutz G, Varnai C, Nagasaka K, Cisneros DA, Stocsits RR, Tang W, Schoenfelder S, Jessberger G, Muhar M, Hossain MJ *et al* (2017) Topologically associating domains and chromatin loops depend on cohesin and are regulated by CTCF, WAPL, and PDS5 proteins. *EMBO J* 36: 3573-3599

Xiang G, Giardine BM, Mahony S, Zhang Y, Hardison RC (2021) S3V2-IDEAS: a package for normalizing, denoising and integrating epigenomic datasets across different cell types. *Bioinformatics*

Xing H, Wu Y, Zhang MQ, Chen Y (2021) Deciphering hierarchical organization of topologically associated domains through change-point testing. *BMC Bioinformatics* 22: 183

Yattah C, Hernandez M, Huang D, Park H, Liao W, Casaccia P (2020) Dynamic Lamin B1-Gene Association During Oligodendrocyte Progenitor Differentiation. *Neurochem Res* 45: 606-619

Ying QL, Wray J, Nichols J, Batlle-Morera L, Doble B, Woodgett J, Cohen P, Smith A (2008) The ground state of embryonic stem cell self-renewal. *Nature* 453: 519-523

Yuan ZF, Sidoli S, Marchione DM, Simithy J, Janssen KA, Szurgot MR, Garcia BA (2018) EpiProfile 2.0: A Computational Platform for Processing Epi-Proteomics Mass Spectrometry Data. *J Proteome Res* 17: 2533-2541

Zhang Y, Li T, Preissl S, Amaral ML, Grinstein JD, Farah EN, Destici E, Qiu Y, Hu R, Lee AY *et al* (2019) Transcriptionally active HERV-H retrotransposons demarcate topologically associating domains in human pluripotent stem cells. *Nat Genet* 51: 1380-1388

Zhang Y, Liu T, Meyer CA, Eeckhoute J, Johnson DS, Bernstein BE, Nusbaum C, Myers RM, Brown M, Li W *et al* (2008) Model-based analysis of ChIP-Seq (MACS). *Genome Biol* 9: R137

Zheng H, Xie W (2019) The role of 3D genome organization in development and cell differentiation. *Nat Rev Mol Cell Biol* 20: 535-550

FIGURE LEGENDS

Figure 1. 3D genome programming.

(A) Scheme for mouse germ-cell development *in vitro* (top) and *in vivo* (bottom), with dynamics of genome-wide DNA methylation levels (middle).

(B) Maximum intensity projections (top) and representative sections (bottom) of typical nuclei of the indicated cell types stained with DAPI. Scale bars, 3 μm.

(C) Areas of DAPI-dense regions (top), distance of DAPI-dense regions from the nuclear periphery (middle), and variance of DAPI signals (bottom). The point marks the median while the thick and thin lines correspond to 66% and 95% intervals, respectively. Number of DAPI dense regions = 950/1450/839/1535/736 and number of slices = 90/115/95/135/110 for mESC/EpiLC/d2/d4c7 mPGCLC/GSC. Significances are computed using Wilcoxon rank-sum tests, p-values from top to bottom 4.37e-3, 1.62e-3, 2.99e-2, 2.03e-10, 4.03e-1, <2.2e-16, 1.31e-3, 8.94e-3, 1.06e-4, 5.62e-2, 4.63e-5, 7.65e-13. P-value symbol brackets: ∗∗∗∗ = [0, 0.0001); ∗∗∗ = [0.0001, 0.001]; ∗∗ = [0.001, 0.01); ∗ = [0.01, 0.05); ns = [0.05, 1].

(D) (left) Fluorescence in situ hybridization (FISH) against chromosome 16 (red) with DAPI staining (grey). Z-stacked representative images are paired with magnified views. (right) Distributions of surface volumes for chr16. The point marks the median while the thick and thin lines correspond to 66% and 95% intervals, respectively. Number of cells = 51/68/53 for mESC/EpiLC/GSC. Scale bars, 5 μm. Significances are computed using Wilcoxon rank-sum tests, p-values from left to right: 4.16e-2, 4.33e-6, 8.68e-9.

(E) Hi-C maps of chromosome 1. (upper right triangle) 250 kb-resolution balanced contact probability matrices; (lower left triangle) matching Pearson's correlation matrices.

(F) Compartmentalization saddle plots for the average interaction frequency between pairs of 50 kb genomic bins belonging to various compartment-score quantiles in cis (upper right triangle) and trans (lower left triangle).

(G) Transitions in euchromatin-vs-heterochromatin bias during the development of different lineages (cardiomyocyte differentiation (Zhang *et al.*, 2019)) at 100 kb resolution. (left axis: violin plots) Distribution of compartment scores; (right axis: dots) ratio of A:B compartment bins.

(H) Enrichment of TAD-TAD interactions involved in max cliques (size ≥3) during the development of different lineages. A dispersal of active hubs was specifically observed during epigenetic reprogramming. Inter-compartmental TAD-TAD interactions are under-represented in all cases.

(I) Network representation of TAD cliques and their compartment identity during germ cell and cardiomyocyte differentiation.

Figure 2. Epigenome profiles and CTCF insulation.

(A) Relative abundance (%) of key histone modifications as measured by mass spectrometry. The point marks the mean while error bars indicate standard errors. Three biological replicates in each cell type were analyzed.
(B) UHC of H3 modification abundances. Numeric suffixes indicate biological replicates.
(C) PCA of average H3 modifications abundances in each cell type.
(D) Chromatin accessibility landscape throughout germline development. (left) ATAC-seq coverage tracks at a representative locus, with peaks highlighted; (second left) distribution of read counts per each in the union peak set; (second right) H3K4me1 ChIP-seq coverage tracks at the same locus; (right) Distribution of domain widths for H3K4me1-enriched regions based on cross-correlation, as implemented in MCORE.
(E) Partial Pearson correlation matrix for inter-cell type ATAC-seq differences against d4c7 mPGCLCs versus differences in other epigenetic signals.
(F) Number of E-P pairs with ABC score > 0.02 (Fulco *et al.*, 2019). Two biological replicates in each cell type were analyzed.
(G) Cell type insulation ranking. 10 different TAD-calling algorithms were used to determine the cell types rank in terms of insulation (gold: most insulated; silver: 2nd most insulated; bronze: 3rd most insulated).
(H) Slope of contact decay (P(s)) curves as a function of genomic separation in log-log space for the germline, neural induction (Bonev *et al.*, 2017), B cell reprogramming (Stadhouders *et al.*, 2018), and cardiomyocyte differentiation (Zhang *et al.*, 2019) datasets.

Figure 3. Open-site characterizations and CTCF release.
(A) 2D UMAP embedding based on epigenetic signals in ATAC-seq peaks for each cell type, with labels derived from semi-supervised HDBSCAN.
(B) Association between open-site clusters and cell types. (top) Number of open sites per cell type in each cluster (left axis: bars) and their enrichment as odds ratios (right axis: dots); (bottom) enrichment of epigenetic signals in each cluster.
(C) Dynamics of open site classes. Classification of the same open sites peak are compared between adjacent stages and shown as flows. Open sites that could not be reliably clustered or were not called as peaks are labelled as “Missing.”
(D) ChIP-seq coverage tracks of CTCF in each cell type.
(E) Number of CTCF peaks called in each cell type. GSCs have considerably fewer CTCF peaks. Two biological replicates in each cell type were analyzed.
(F) Correlograms of CTCF binding in the union peak set. (Upper right panels) Pearson’s correlation coefficients between log2 transformed signals. (Diagonal) Histograms of CTCF signal intensity in the union peak set. (Lower left panels) 2D density plots of CTCF binding in pairs of cell types.
(G) Aggregate plots of ChIP-seq enrichment for various targets and insulation score (IS) around CTCF-binding sites depleted in GSCs as compared to d4c7 mPGCLCs. n =

39408.
(H) 3D epigenetic landscape re-wiring near *Ddx4*. Observed/expected contact maps at 10 kb resolution for d4c7 mPGCLCs and GSCs are shown alongside select ChIP-seq and NET-CAGE coverage tracks. A strong insulating CTCF peak (highlighted in red) upstream of the *Ddx4* TSS (upstream blue highlight) is lost in GSCs, facilitating the interaction between the *Ddx4* promoter and an active enhancer (downstream blue highlight) demonstrating pronounced bidirectional nascent transcription (bottom).
(I) GSEA using genes ranked by concomitant differential expression and promoter interaction. (left) ABC-defined E-P pairs overlapping GSC-depleted CTCF peaks are used to rank genes based on coordinated E-P interaction and expression differences; (right) $\log_2$ fold changes for leading-edge genes of enriched gene sets. Significances computed using pre-ranked multilevel GSEA, p-values from top to bottom: 0.00106, 0.00343, 0.0173, 0.0269, 0.0382, 0.0439, 0.0109, 0.0439, 5.19e-6, 6.26e-5, 1.79e-6, 1.91e-6, 0.00931, 0.0454, 0.0125, 6.24e-10, 2.17e-11, 6.24e-10, 6.18e-12.

Figure 4. Generation of minimal LADs.
(A) Correlation between compartment score and ChIP-seq enrichment at 50 kb resolution.
(B) Correlation between differential compartment score and differential ChIP-seq enrichment between mESCs and GSCs at 50kb resolution.
(C) Representative chromosome-wide distributions of compartment score and lamin B1 enrichment for mESCs and GSCs.
(D) LAD occupancies in different cell types (Peric-Hupkes *et al.*, 2010; Poleshko *et al.*, 2017; Robson *et al.*, 2016; Yattah *et al.*, 2020).
(E) Venn diagram of LADs called in GSCs, union of LADs called in all other cell types in this study, and union of LADs identified from all other studies (Peric-Hupkes *et al.*, 2010; Poleshko *et al.*, 2017; Robson *et al.*, 2016; Yattah *et al.*, 2020).
(F) UpSet plot for the union set of LADs in different studies (Peric-Hupkes *et al.*, 2010; Poleshko *et al.*, 2017; Robson *et al.*, 2016; Yattah *et al.*, 2020). A majority of regions correspond to constitutive LADs.
(G) IF analysis for lamin B1 in (left) EpiLCs and d4c7 mPGCLCs, as well as (right) EpiLCs and GSCs. Symbols for each cell type are as indicated. Scale bars, 10 μm.
(H) Western blot for lamin B1 in different cell types (bottom) and quantification normalized by β-actin (top).
(I) Average distributions of lamin B1 enrichment across all chromosomes (1–19, X). Ribbons correspond to 95% confidence intervals of fitted GAMs.
(J) Lamin B1 ChIP-seq enrichment in the first (left/p-ter) and the last (right/q-ter) 300 Kb of each chromosome. The point marks the median while the thick and thin lines correspond to 66% and 95% intervals, respectively. Number of chromosomes = 20 (autosomes and chromosome X).
(K) Representative chromosome-wide distributions of ChIP-seq enrichment for lamin B1

and H3K9me3/me2.
(L) (top) Representative images of FISH against major satellite repeats in EpiLCs and GSCs. Scale bars, 10 μm; (bottom) percentage of the pericentromeres detached from the nuclear lamina in EpiLCs and GSCs. The point marks the median while the thick and thin lines correspond to 66% and 95% intervals, respectively. Number of cells = 18/22 for EpiLC/GSC.

Figure 5. Heterochromatin re-organization.
(A) (left) H3K9me3 ChIP-seq tracks, with TEs in different classes shown below; (right) Distribution of domain widths for H3K9me3-enriched regions based on cross-correlation, as implemented in MCORE.
(B) Spatial-temporal dynamics of H3K9me3 domains (>10 Kb) analyzed using ChromTime.
(C) (Top) Enrichment of interaction between (upper) and within (lower) broad H3K9me3 domains (>50 Kb; identified in GSCs and overlap peaks in all other cell types).
(D) Correlation between H3K9me2/3 and lamin B1 ChIP-seq enrichment.
(E) IF analysis for H3K9me3 (left) and H3K9me2 (right) in EpiLCs and GSCs. Arrowheads: GFP^+ GSCs; arrows: EpiLCs. Scale bars, 10 μm.
(F) Odds ratio and significance of overlap between H3K9me3 domains conserved across all cell types and different repeat families. Error bars denote 95% confidence intervals.
(G) Scatter plot of lamin B1 enrichment in GSCs vs the aggregated density of select TEs (L1, ERV1 and ERVK) in 1mb bins, with points colored by H3K9me3 enrichment in GSCs.
(H) Expression of H3K9 methyltransferases as measured by RNA-seq (Ishikura *et al.*, 2016; Ohta *et al.*, 2021; Sasaki *et al*, 2015). Two biological replicates in each cell type were analyzed.
(I) (left) Western blot for G9a, GLP, Setdb1 and α-tubulin; (right) quantification normalized by α-Tubulin.
(J) (left) Scatter plot of H3K9me3 enrichment across all promoters in d2 mPGCLCs and d4c7 mPGCLCs, with 728 genes (red) showing substantially higher H3K9me3 levels in d2 mPGCLCs than d4c7 mPGCLCs; (right) pathway enrichment of the 728 genes using g:Profiler.
(K) Aggregate plot of H3K9me3 around the TSSs of *Setdb1*-repressed germline genes (Karimi *et al*, 2011). The thick line marks the mean while the upper and lower limits indicate standard errors.
(L) Normalized H3K9me3 tracks around the TSSs of *Dazl* and *Ddx4*.
(M) Distribution of differences in promoter H3K9me3 between d2 and d4c7 mPGCLCs for germline genes (Kurimoto *et al.*, 2015), *Setdb1*-repressed germline genes (Karimi *et al.*, 2011) and other genes. The point marks the median while the thick and thin lines correspond to 66% and 95% intervals, respectively. From top to bottom, Number of

genes = 19559, 21, 99. Significances are computed using Wilcoxon rank-sum tests, p-values from top to bottom: 2.36e-3, 1.14e-9, 4.43e-1.

Figure 6. Mechanism of PMD formation via balancing H3K36me2 vs H3K9me-marked LADs and Y chromosome hypomethylation.

(A) (top) Overlap of PMDs between spermatogonia (Kubo *et al.*, 2015) and GSCs; (bottom) Representative locus demonstrating colocalization of H3K9me3 and lamin B1 enrichment wit DNA hypomethylation.

(B) The area under the receiver operating characteristic (AUROC) of classifiers predicting 50 kb bins as either PMD or not in GSCs using each cell type's own epigenome. Error bars denote 95% confidence intervals.

(C) Correlation of GSCs' DNA methylation levels in GSC LADs with epigenetic signals in different cell types.

(D) Aggregate plots of H3K36me2, H3K9me2, H3K9me3, and lamin B1 enrichment as well as DNA methylation around PMDs in GSCs. The thick line marks the mean while the upper and lower limits indicate standard errors.

(E) Scatter plot of d4c7 mPGCLCs' H3K9me3 and H3K27me3 enrichment in 50 kb bins colored by differential H3K36me2 (EpiLCs−d4c7 mPGCLCs).

(F) Representative chromosome-wide distributions of compartment score, lamin B1 enrichment, and H3K36me2 coverage.

(G) Correlation between H3K36me2 and compartment scores or lamin B1 enrichment in 50 kb bins.

(H) Relationship between the max clique size involving a given TAD and the average H3K9me3 enrichment in that TAD in d4c7 mPGCLCs. Number of TADs with specific max clique sizes, from left to right: 798/269/94/35/18/11. The central band of boxplots indicate median values, while the lower and upper hinge correspond to the first and third quartile, and the upper whiskers extend to the largest value % 1.5 * IQR and vice versa for the lower whiskers.

(I) IP/input ratio of H3K9me3 and lamin B1 alignments per chromosome.

(J) Enrichment tracks of H3K9me3 and lamin B1 as well as DNA methylation in EpiLCs and d4c7 mPGCLCs on chromosome Y.

(K) (top) FISH against the Y chromosome; (bottom) sphericity of the Y chromosome FISH signals; (right) distributions Y chromosome surface volumes. The point marks the median while the thick and thin lines correspond to 66% and 95% intervals, respectively. Number of cells = 89/76/69 for mESC/EpiLC/GSC. Scale bar, 10 μm. Significances are computed using Wilcoxon rank-sum tests, p-values from

(L) Proportion of the genome occupied by PMDs in GSCs with stratification by chromosome.

(M) 2D density plots of DNA methylation level (mCG/CG) between EpiLCs and GSCs in 10 kb bins.

Figure 7. Nucleome differences between GSCs and GSCLCs.
(A) Scheme for the derivation of GSCs and GSCLCs.
(B) Maximum intensity projections (top) and representative sections (bottom) of typical nuclei of GSCs and GSCLCs stained with DAPI. Scale bars, 3 μm.
(C) Areas of DAPI-dense regions (left), distance of DAPI-dense regions from the nuclear periphery (middle), and variance of DAPI signals (right). The point marks the median while the thick and thin lines correspond to 66% and 95% intervals, respectively. Number of DAPI dense regions = 1535/736/1227 and number of slices = 135/110/120 for d4c7 mPGCLC/GSC/GSCLC. Significances are computed using Wilcoxon rank-sum tests, p-values from left to right: 2.03e-10, 1.69e-9, 0.123, 0.00894, 8.02e-8, 0.0707, 7.65e-13, 0.417, 2.07e-12.
(D) (bottom) 250 kb resolution balanced contact probability matrices of chromosome 1 in GSCs (upper) and GSCLCs (lower); (top) fold change (GSCLCs/GSCs) of contact probability, showing an attenuation of distal interactions in GSCLCs.
(E) Distribution of compartment scores (bottom axis: violin plots) and ratio of A:B compartment bins (top axis: dots) at 100 kb resolution.
(F) Differential subcompartmentalization between GSCs and GSCLCs at 50 kb resolution. (top) Jaccard index between genomic bins belonging to each subcompartment in GSCs vs GSCLCs. (bottom) Comparison of subcompartment labels between cell types reveals a greater proportion of the genome belongs to the upper triangle, in line with GSCLCs being more repressive. (right) Quantification of matched bins in the upper vs lower triangle.
(G) Comparison of overall subcompartment proportions in GSCs vs GSCLCs. Most significant changes are again observed mostly for the intermediate states and not active euchromatin (A.1) or constitutive heterochromatin (B.2). Significances are computed using two-proportions z-tests, p-values from left to right: 0.0829, 0.107, 0.0169, 3.32e-5, 0.683, 1.09e-16, 7.46e-9, 0.0112.
(H) (left) Fold change (GSCLCs/GSCs) of different H3 modifications as measured by mass spectrometry, with confidence intervals denoting standard errors; (right) full data for select modifications. Three biological replicates in each cell type were analyzed.
(I) Normalized H3K27me3 coverage tracks around *Dmrt1* and *Dmrt3*.
(J) GSEA results for promoters ranked by preferential enrichment in GSCLCs as compared to GSCs. Significances computed using pre-ranked multilevel GSEA, p-values from top to bottom: 7.11e-5, 3.31e-6, 5.15e-8, 1.44e-5, 9.71e-5, 3.06e-6, 0.000159, 1.42e-6, 0.000513, 3.66e-7, 0.000185, 8.43e-6, 3.31e-6, 3.7e-7, 0.000194.
(K) Number of CTCF peaks in each cell type. Two biological replicates in each cell type were analyzed.
(L) Pile-up plots of intra-TAD interactions in GSCs and GSCLCs.
(M) 3D epigenetic landscape rewiring near *Ddx4*. Differential (GSCLCs/GSCs) contact maps and ChIP-seq coverage at the *Ddx4* locus are shown. The insulating CTCF peak separating *Ddx4* from one of its enhancers is not completely removed in GSCLCs.

Figure 8. A model for the nucleome programming during mouse germ-cell development.

Unlike somatic fates, germline nucleome programming entails extensive euchromatization, which is associated with radial re-positioning of pericentromeres and peripheral de-attachment elsewhere. Augmented insulation helps to maintain transcriptional fidelity during global DNA hypomethylation in PGCs (PGCs bear oogenic potential as well (represented by a dashed arrow)). Insulators are subsequently erased en masse to activate gametogenic program during the PGCs-to-spermatogonia/SSC development. Faulty nucleome maturation involving intermediate compartment states leads to impaired spermatogenic capacity (represented by a thin arrow).

LEGENDS TO EXPANDED VIEW FIGURES

Figure EV1. Investigation of global nuclear architecture dynamics through Hi-C and FISH.

(A) Fluorescence in situ hybridization (FISH) against chromosome 1 (red) with DAPI counterstaining (grey). (Left) Z-stacked representative images (top left) are paired with magnified views (bottom left). (Right) The distribution of "surface" volumes for chr1, as seen for chr16, validates chromosomal decondensation in GSCs. Number of cells = 51/68/53 for mESC/EpiLC/GSC. Wilcoxon rank-sum test p-values (left to right): 4.16e-2, 4.33e-6, 8.68e-9. P-value symbol brackets: ∗∗∗∗ = [0, 0.0001); ∗∗∗ = [0.0001, 0.001]; ∗∗ = [0.001, 0.01); ∗ = [0.01, 0.05); ns = [0.05, 1].

(B) Hierarchical clustering of stratum-adjusted correlation coefficients (SCC) between samples validating the reproducibility of biological replicates.

(C) Contact probability decay across different inter-loci separation distances for various cell types throughout *in vivo* and in vitro germ cell differentiation, demonstrating a gain of distal interactions along differentiation, especially at distances >50 Mb.

(D) Sankey diagram of compartment identities in 50 kb bins across cell types. Compartment A regions newly acquired by GSCs are formed through a unidirectional switch of B-A with relatively little reversal.

(E) 25 kb-resolution balanced contact maps spanning chr3:5–12.5 mb.

(F) Degree of TAD boundary conservation in different lineages. Consistent across different lineages, more than 40% TAD boundaries are significantly conserved across differentiation. One-sided permutation tests were carried out by shuffling sample labels 100000 times, with p-values (left to right, top to bottom): 1, 1, 1e-5, 1, 1, 1e-5.

(G) Convex hull volumes of CSynth-produced chromosome 3D models during the development of different lineages, after normalization to unit backbone length. n = 22/19 for cardiac/germline. Wilcoxon signed-rank test p-values (left to right): 1.91e-6, 1.89e-1, 1.69e-3, 2.61e-4, 4.77e-6, 1.86e-3, 2.93e-4.

(H) UHC based on Euclidean distance between 100 kb compartment score tracks for cell types from in vitro and *in vivo* germ cell differentiation, with comparable stages consistently grouped together.

(I) PCA of compartment scores at 100 kb resolution for various cell types throughout *in vivo* and in vitro germ cell differentiation, with comparable stages consistently grouped together.

Figure EV2. Quantitative epigenome analysis by mass spectrometry and chromatin accessibility analysis by ATAC-seq.

(A) (Top) Immunofluorescence against H3K27me3 in mESCs and GSCs; the shaftless arrow marks a GFP+ GSCs and the shaftless arrowhead indicates mESCs. (Bottom) Immunofluorescence against H3K9me2 in EpiLCs and d4c7 mPGCLCs; the shaftless

arrowhead marks a Blimp1-mVenus+ d4c7 mPGCLCs and the arrow indicates EpiLCs. Scale bars = 10 μm.
(B) Western blot against H3K9me3, H3K9me2, and histone H3 in each cell type (bottom) and H3-normalized quantification (top).
(C) Coefficients of variation across replicates of histone modification abundance as measured by quantitative histone mass spectrometry versus western blot for H3K9me2, H3K9me3, and H3K27me3. Mass spectrometry measurements consistently exhibit higher reproducibility. Number of biological replicates = 15/21 for mass spectrometry/western blot. Wilcoxon rank-sum test p-value: 5.34e-5.
(D) Schematic of normalizing histone modification ChIP-seq via mass spectrometry-derived coefficients. With only depth-normalization (left), EpiLCs and d4c7 mPGCLCs appear to have comparable H3K9me2 profiles both in terms of coverage tracks (top) and in a pairwise scatter plot comparing the two cell types (bottom); after multiplication of their relative abundances based on mass spectrometry, the comparatively lower levels of H3K9me2 in d4C7GCLCs become apparent (right).
(E) Comparison of regions with greater ("more open") and reduced ("less open") accessibility in the union peak set of germline samples and E14.5 mouse fetal tissues (Gorkin *et al.*, 2020) (left). Through fitting two-component gaussian mixture models, d4c7 mPGCLCs stand out as possessing the most permissive genome (right).
(F) PCA of ATAC-seq signals in the top 10,000 most variable peaks from the union peak set including MEFs (Di Giammartino *et al*, 2019).
(G) UHC of the top 2,000 most variable ATAC-seq peaks in the union peak set including MEFs. (left) Clustered ATAC-seq enrichment heatmap; (right) overrepresented TF-binding motifs in each cluster.

Figure EV3. Exploration of cis-regulatory element by NET-CAGE combined with Hi-C and comparison against public Hi-C datasets.
(A) An example of enhancer-promoter interactions for Nanog in mESCs as predicted by ABC, all of which correspond to known associations including super-enhancers.
(B) (Top) Distribution of distances separating ABC-predicted enhancer-promoter pairs in each replicate. The central band of boxplots indicate median values, while the lower and upper hinge correspond to the first and third quartile, and the upper whiskers extend to the largest value % 1.5 * IQR and vice versa for the lower whiskers. Notches correspond to 1.58 * interquartile range of distances / (# of E-P pairs)$^{1/2}$, comparable to 95% confidence intervals around the median. d4c7 mPGCLCs' E-P pairs are significantly shorter in range than those of other cell types. (Bottom) Magnified view from 60 kb to 100 kb. Number of ABC E-P pairs from left to right: 60535, 59312, 59116, 59075, 58702, 58704, 53092, 52074, 60867, 58858.
(C) (Top) Co-transcription of enhancer-promoter pairs with correlated NET-CAGE expression. The observed number of correlated E-P pairs involving tag clusters transcribed (TPM > 1) in a given cell type (points) are compared against a permuted

background in which tag clusters are sampled from the union tag cluster set. (Bottom) Observed / expected number of E-P pairs with correlated NET-CAGE expression and co-expressed (>1 TPM) in a given cell type. Two-sided permutation tests were carried out by sampling 100000 times from the set of elements expressed in at least 1 cell type, with p-values (left to right): 2e-5, 2e-5, 2e-5, 2e-5, 2e-5, 2e-5, 6.44e-3, 7.64e-2. Two biological replicates in each cell type were analyzed.
(D) Number of TAD boundaries in each cell type across 10 different algorithms. Dots correspond to values produced by a specific algorithm for a given cell type and are grouped into lines by algorithm.
(E) Auto-correlation of compartment scores (25 kb bins), with a slower decay indicative of broader compartments.
(F) Aggregate plots of S3V2-normalized ChIP-seq profiles for CTCF and Rad21 around the union set of TAD boundaries.
(G) Mean f-VICE across replicates (error bars indicate standard errors) for CTCF motifs overlapping both Rad21 and CTCF peaks within the union set of TAD boundaries. Two biological replicates per cell type were analyzed.
(H) representative locus demonstrating the emergence of smaller insulated domains in d4c7 mPGCLCs within otherwise homogeneous wider TADs observed in earlier stages.
(I) Proposed mechanism for elevated insulation via the reduction of loop extrusion factor's residence time, leading to shorter loops and domains.
(J) (Top) Slope of contact decay (P(s)) curves as a function of genomic separation in log-log space for *in vivo* germline development (Du *et al.*, 2017; Du *et al.*, 2020); (bottom) genomic separation with the most negative second derivative of P(s) in log-log space, corresponding to distance of fastest decline in contact frequency.
(K) Genomic separation with fastest decline in contact frequency for cell types across *in vivo* and *in vitro* germ cell differentiation.

Figure EV4. Open site chromatin state dynamics and differential CTCF binding throughout germ cell differentiation.
(A) Overlap enrichment analysis of consolidated open site clusters against annotations from the Ensembl Regulatory build. P-values computed using Fisher's exact tests.
(B) Select ChIP-seq coverage tracks around a representative cluster 2 loci.
(C) Western blot against CTCF in the chromatin-bound fraction (top row) and whole cell lysate (middle row) as well as α-tubulin (bottom row) in each cell type. The signals of CTCF from whole cell lysates were normalized by α-Tubulin, while those of the chromatin-bound fraction were normalized by the mean across all cell types (top panel).
(D) 2D UMAP embedding based on epigenetic signals in promoters for each cell type, with labels derived from semi-supervised HDBSCAN.
(E) Enrichment of epigenetic signals in each promoter cluster and expression of the cognate gene.

(F) Association between promoter clusters and cell types. Number of open sites per cell type in each cluster (top axis: bars) and their enrichment as odds ratios (bottom axis: dots). Error bars indicate 95% confidence intervals.

(G) Pile-up plots of intra-class promoter-promoter interactions.
(H) Contributors of differential CTCF binding. The aggregate plot of various ChIP-seq enrichment signals (left) as well as the insulation score (right) near CTCF-binding sites found both in cell types ("constitutive") or only GSCs but not in d4c7 mPGCLCs ("GSC-high") appear largely identical in their chromatin state yet distinct from those lost in GSCs. n = 35692/13364 for constitutive/GSC-high peaks.
(I) 3D epigenetic landscape rewiring near Ddx4. Observed/expected contact maps at 10 kb resolution for mESCs, EpiLCs and d2 mPGCLCs are shown alongside select ChIP-seq coverage tracks. A strongly insulating CTCF peak (highlighted in red) upstream of Ddx4's TSS is found in all earlier stages and prevents spurious activation.
(J) Coordinated differential expression and E-P looping between d4c7 mPGCLCs and GSCs. Strong correlation was observed when applying stratified rank-rank hypergeometric overlap to genes ranked by differential expression versus differential E-P interactions straddling sites depleted of CTCF binding in GSCs. While increased E-P looping is correlated with elevated expression regardless of whether the interaction spans differential CTCF-bound sites, the degree of coordination is stronger (i.e., more significant / brighter) for those that do straddle GSC-depleted sites.

Figure EV5. Inter-species comparison of germ-cell specific chromatin structure and characterization of H3K9me3-enriched repeats.
(A) Average distributions of differential (GSC – EpiLC) lamin B1 enrichment (top) or compartment score (bottom) across all chromosomes (1–19, X). Ribbons correspond to 95% confidence intervals of fitted GAMs.
(B) Average distributions of compartment score (spermatogonia – fibroblast) across all chromosomes (excluding Y) for *Macaca mulatta* (top) and *Mus musculus* (bottom).
(C) Estimated age of families overlapping H3K9me3 domains based on age = divergence/substitution rate with 4.5×10^{-9} as the rate and milliDiv from RepeatMasker as the divergence (Bourque *et al*, 2008). Wilcoxon rank-sum tests p-values, from left to right: 0, 0, 0. Number of TE instances, from left to right: 227732, 982369, 2671107.
(D) Correlation between lamin B1 enrichment and density for different repeat families.

LEGENDS TO EXPANDED VIEW TABLES AND MOVIES

Dataset EV1. Sequencing summary.

Dataset EV2. Histone modification abundances.

Dataset EV3. Motif enrichment results.

Dataset EV4. Cluster annotations.

Dataset EV5. Annotation overlap results.

Dataset EV6. Pathway association results.

Movie EV1. 3D re-organization of chromosome 16 during germ cell development.

Nagano et al., figure 1

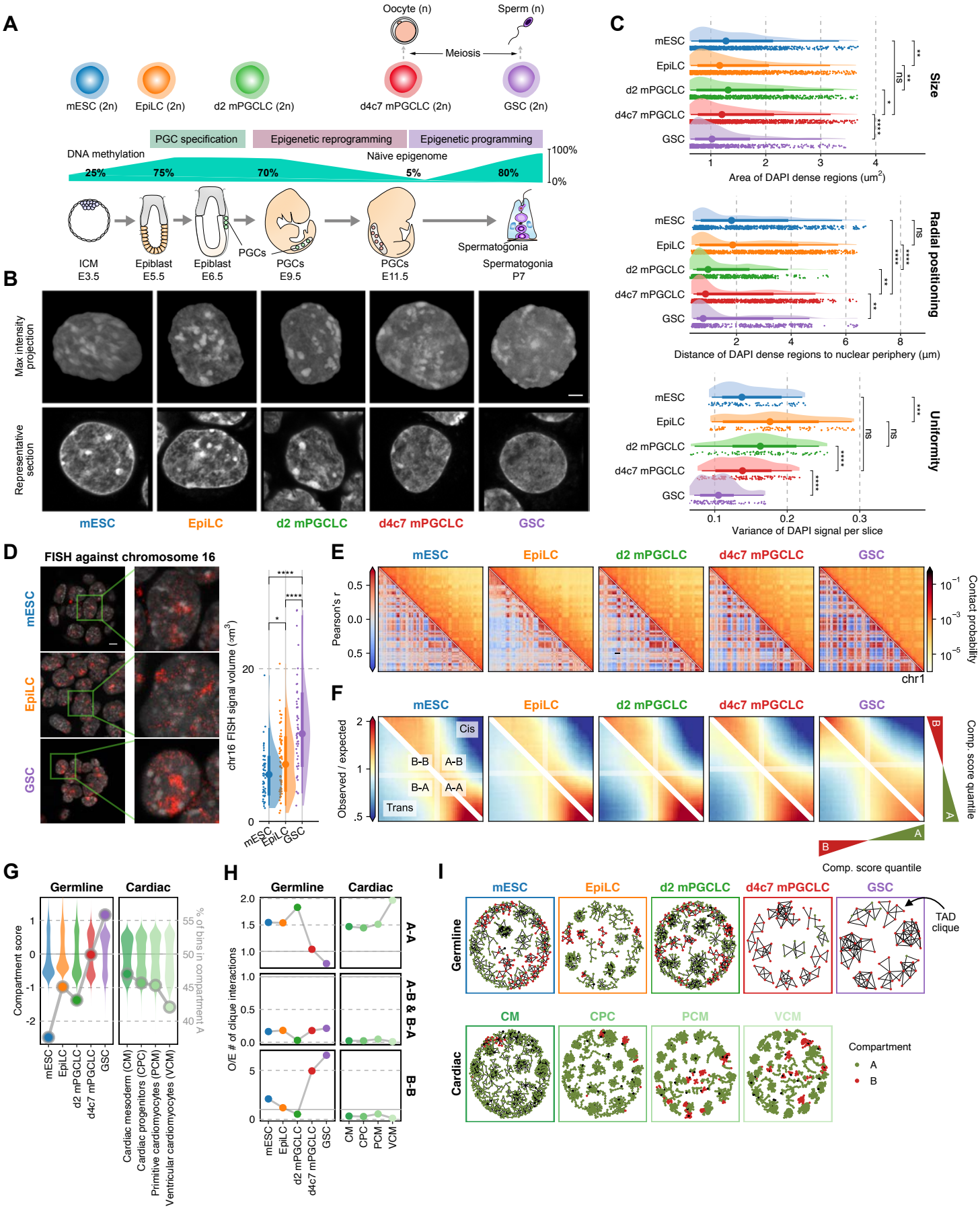

Nagano et al., figure 2

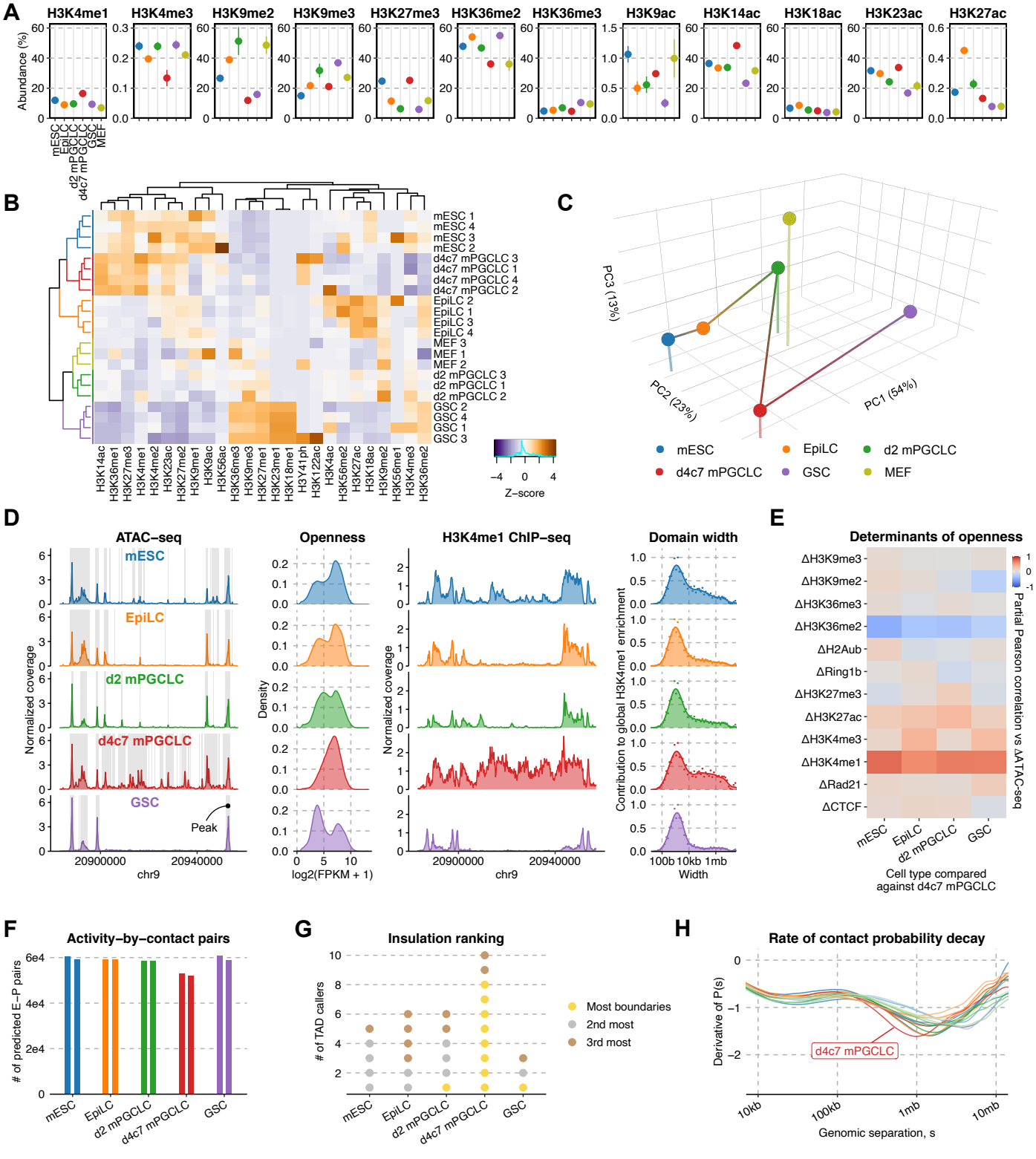

Nagano et al., figure 3

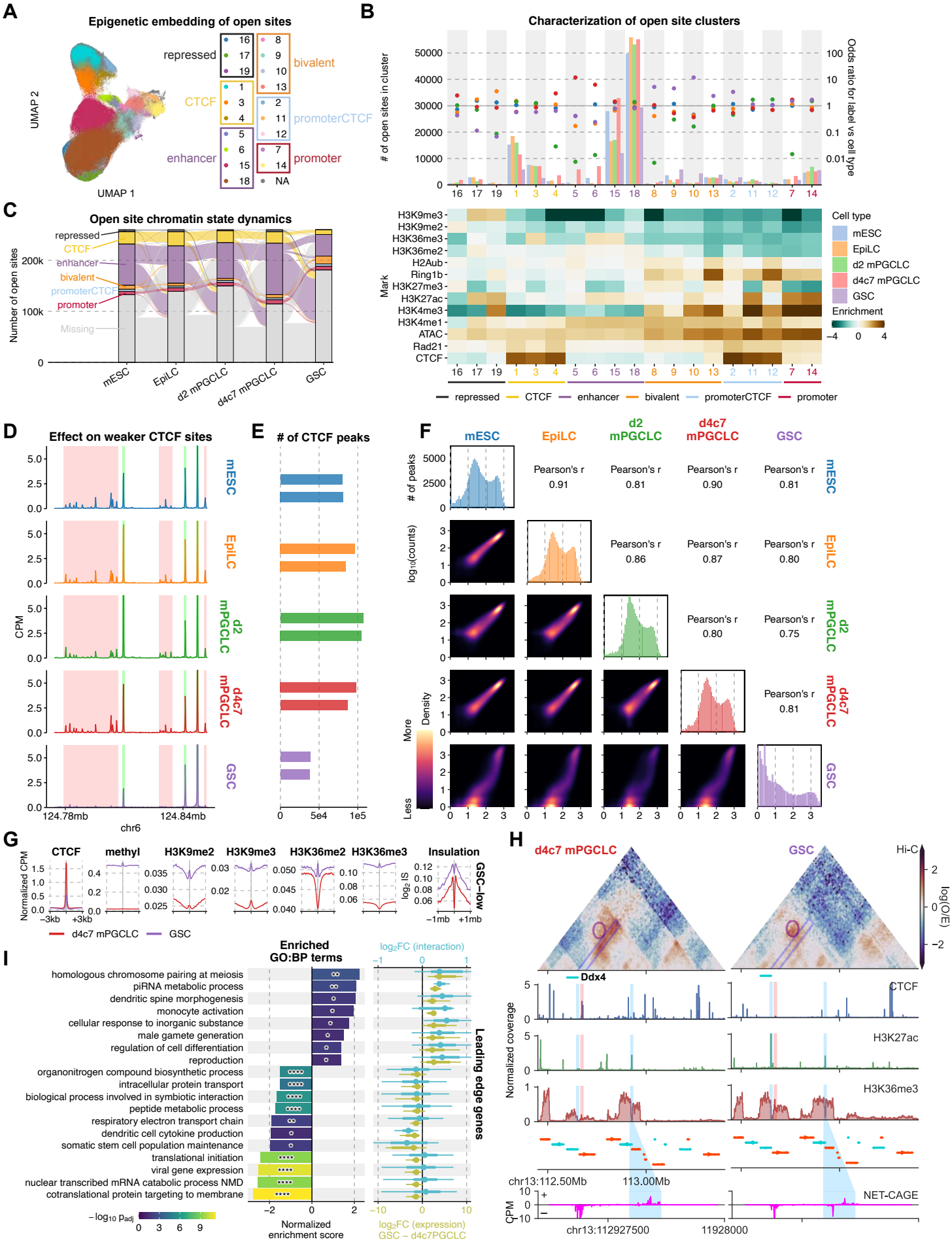

Nagano et al., figure 4

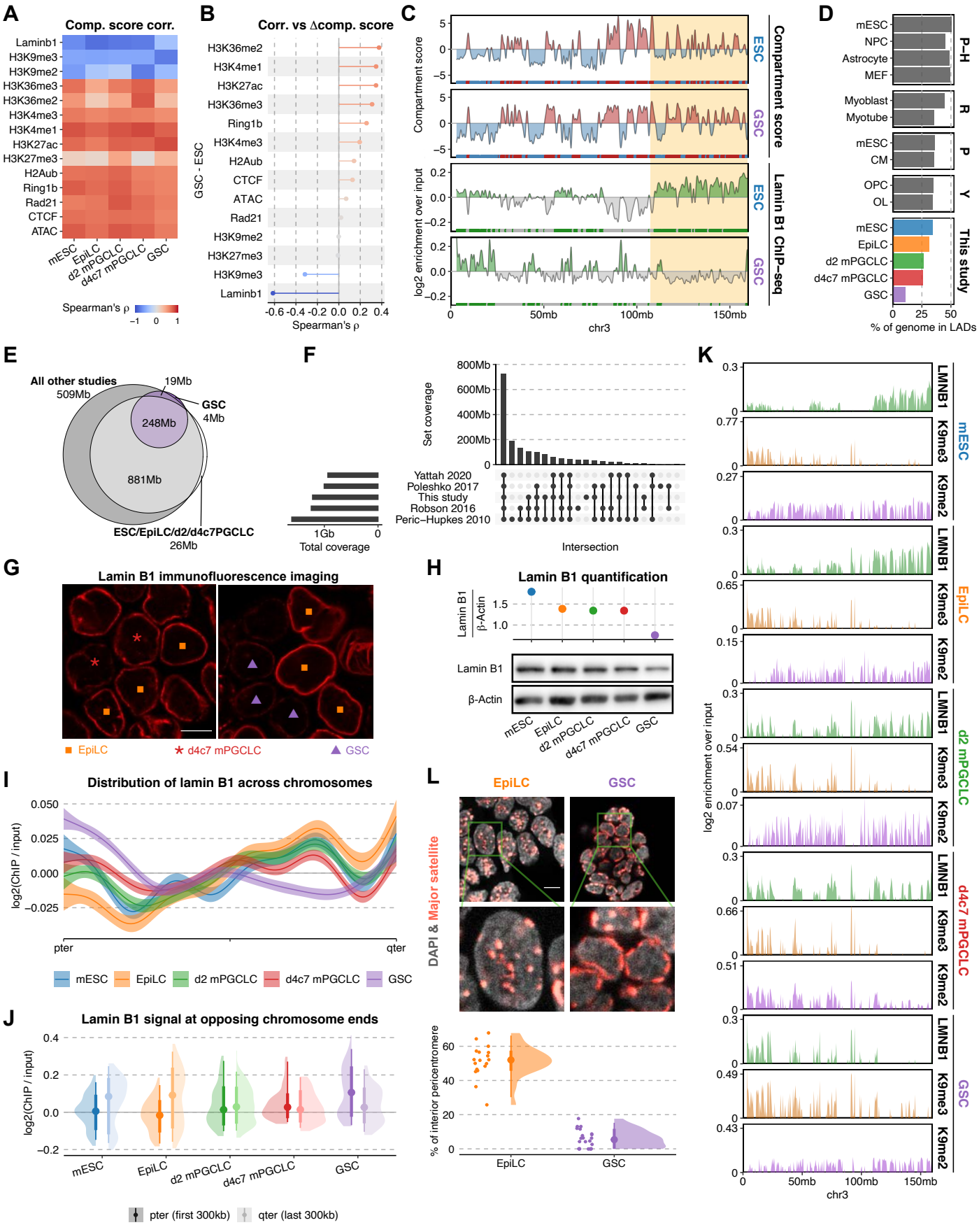

Nagano et al., figure 5

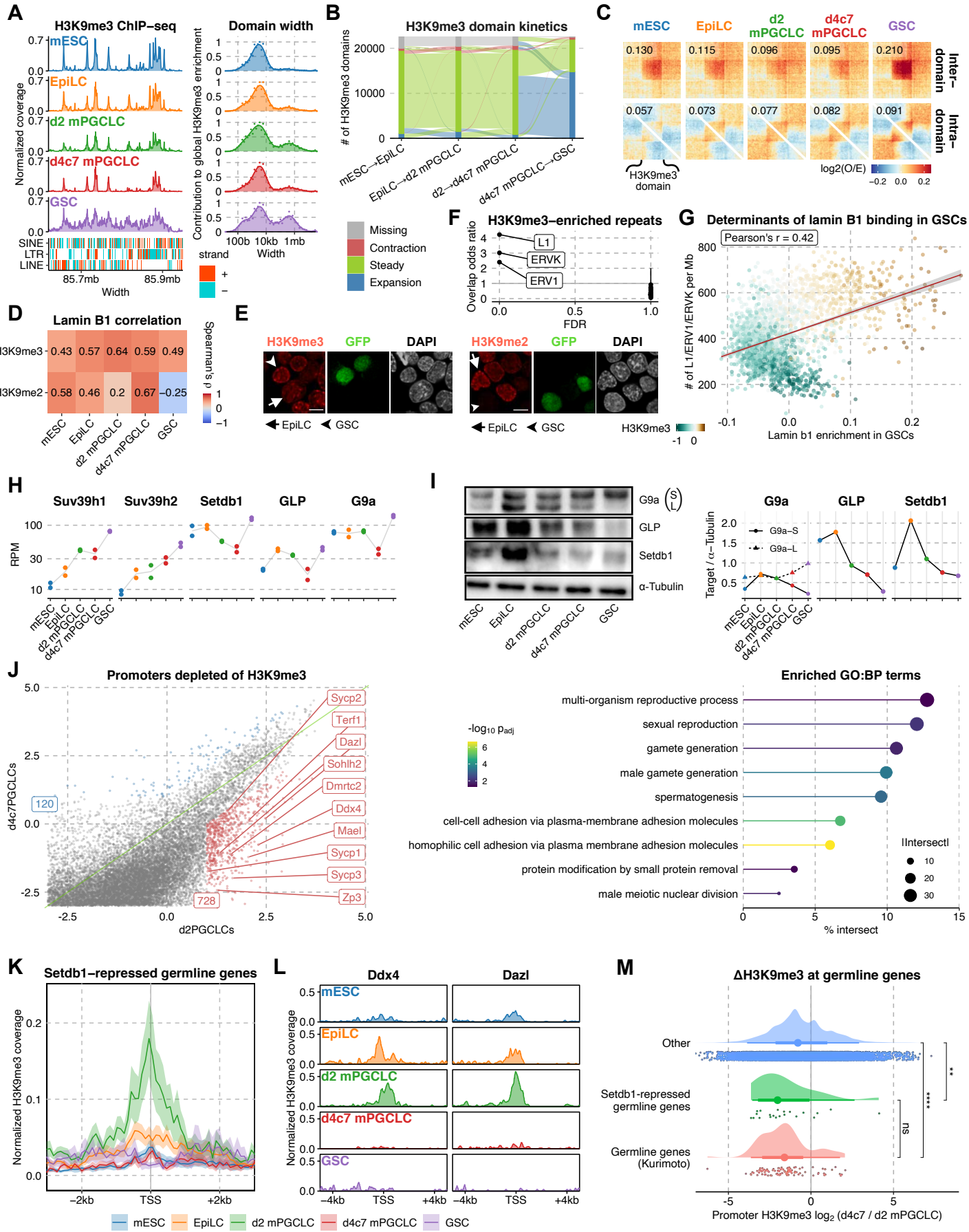

Nagano et al., figure 6

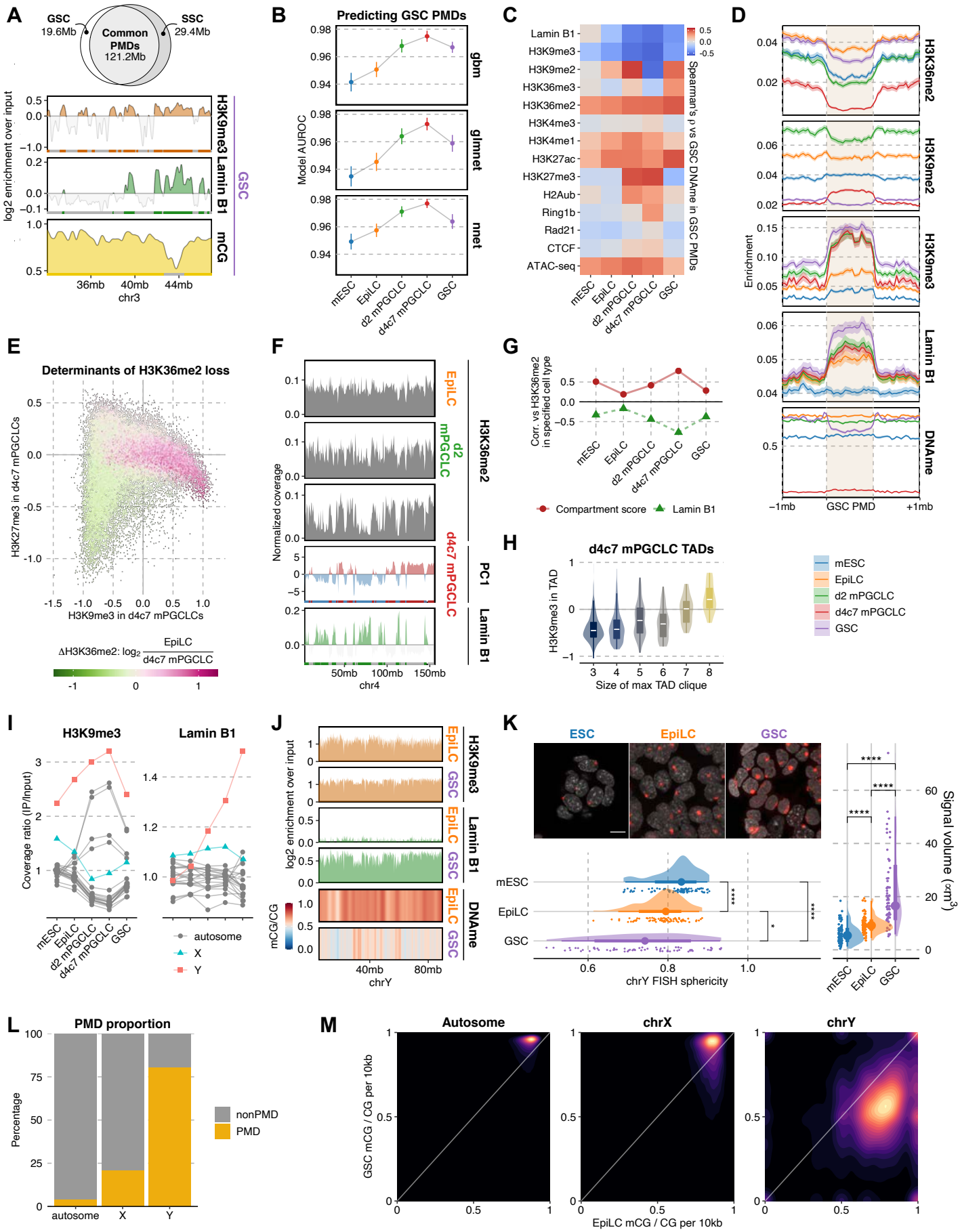

Nagano et al., figure 7

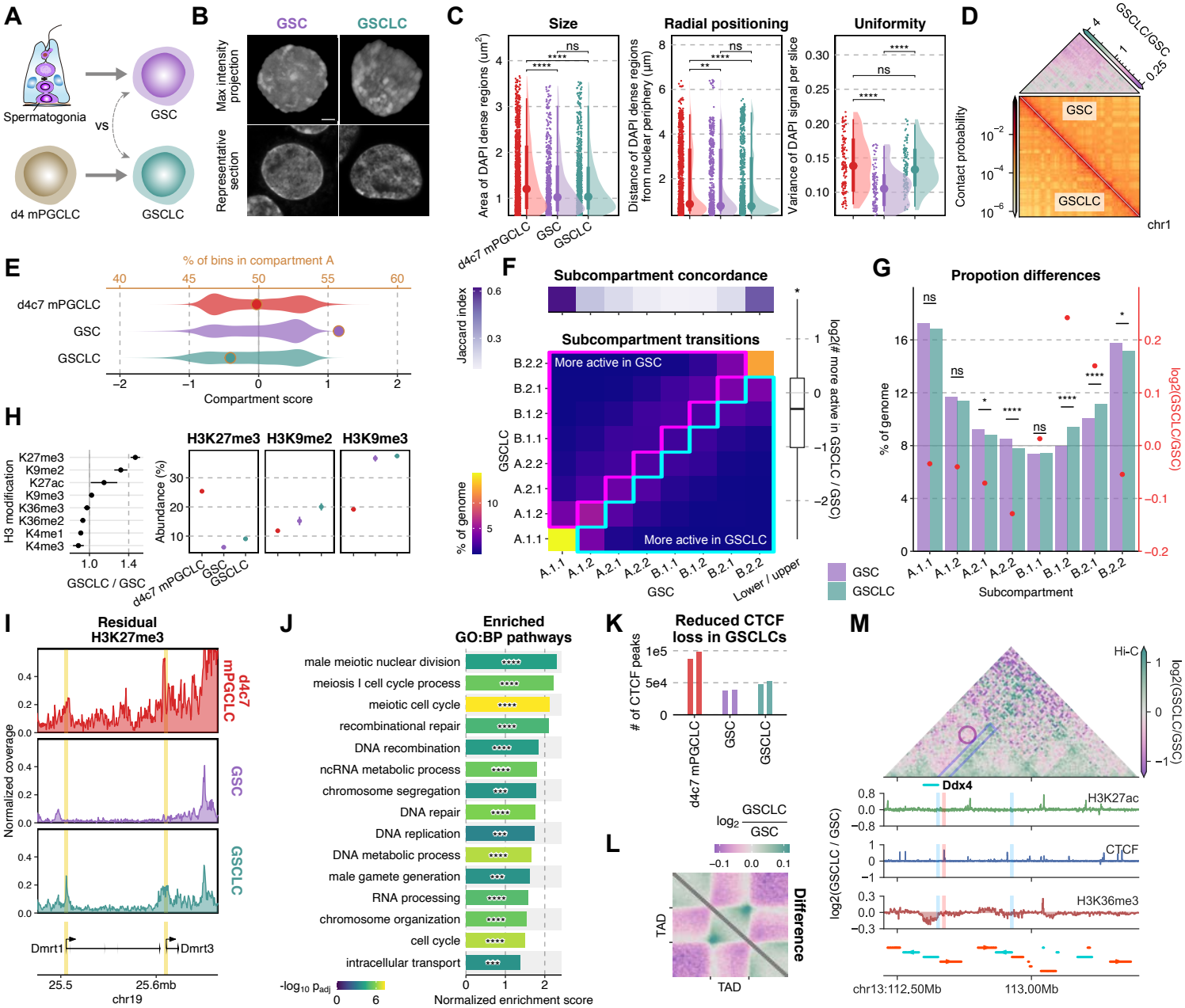

Nagano et al., figure 8

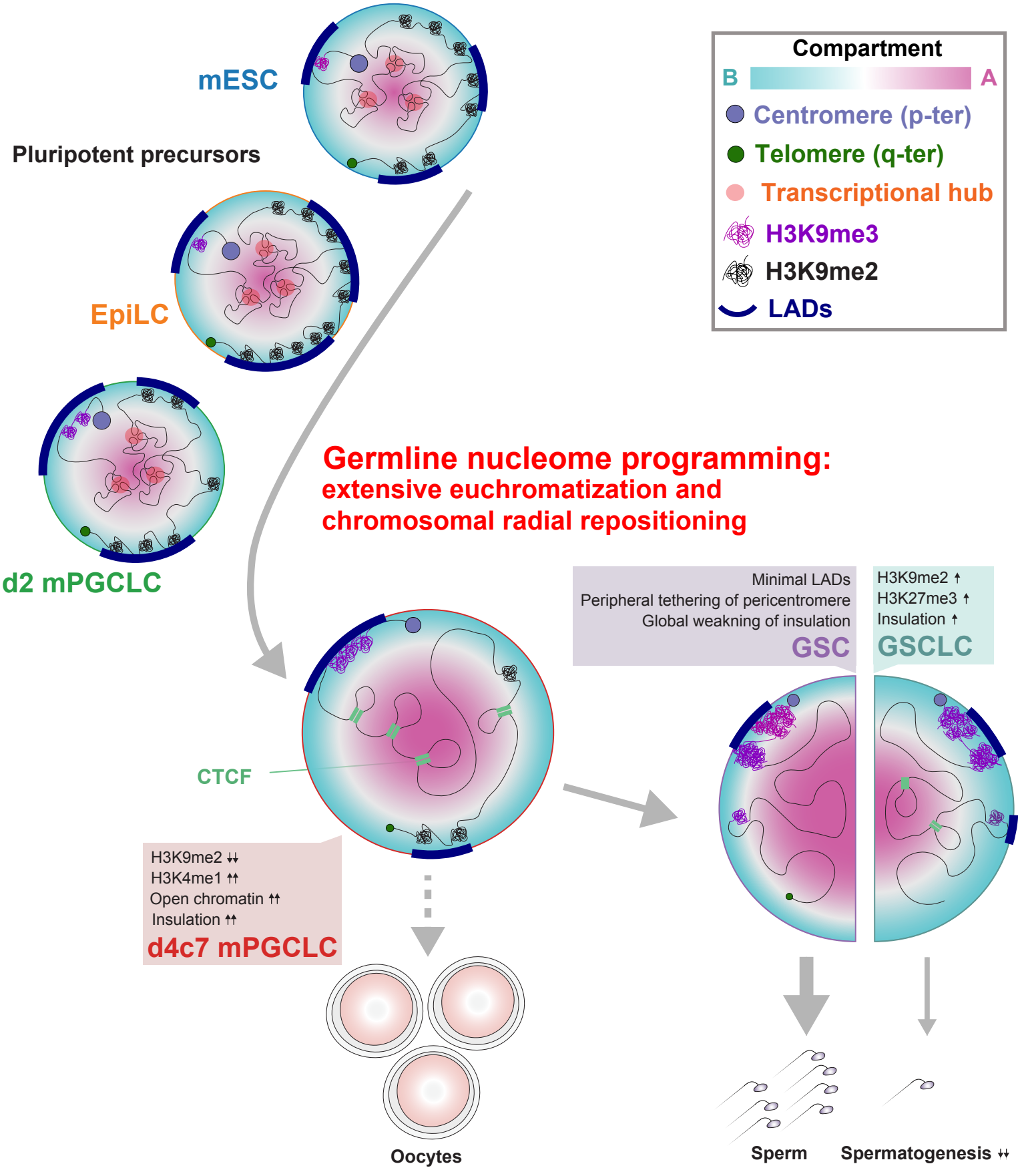

Nagano et al., figure EV1

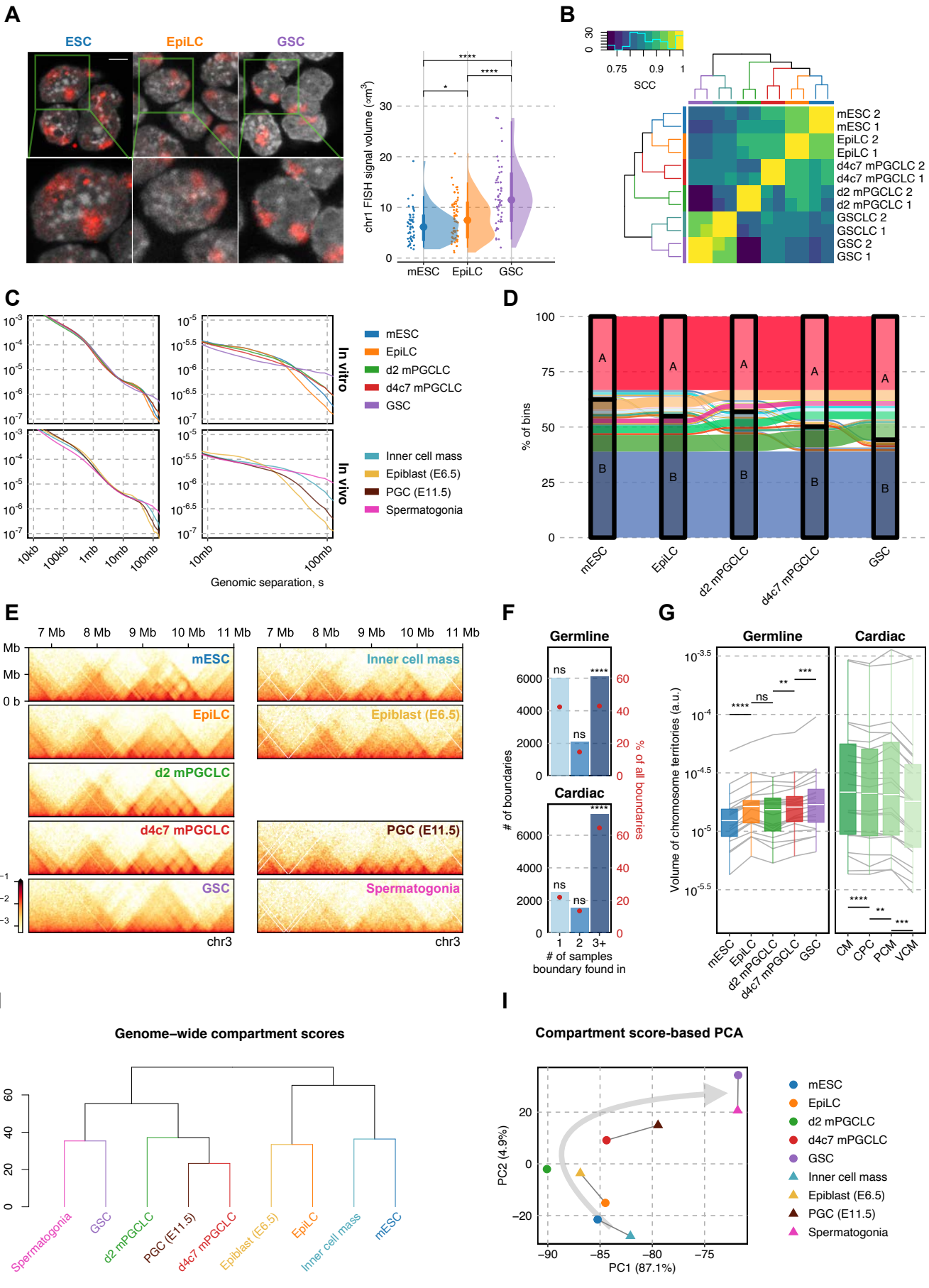

Nagano et al., figure EV2

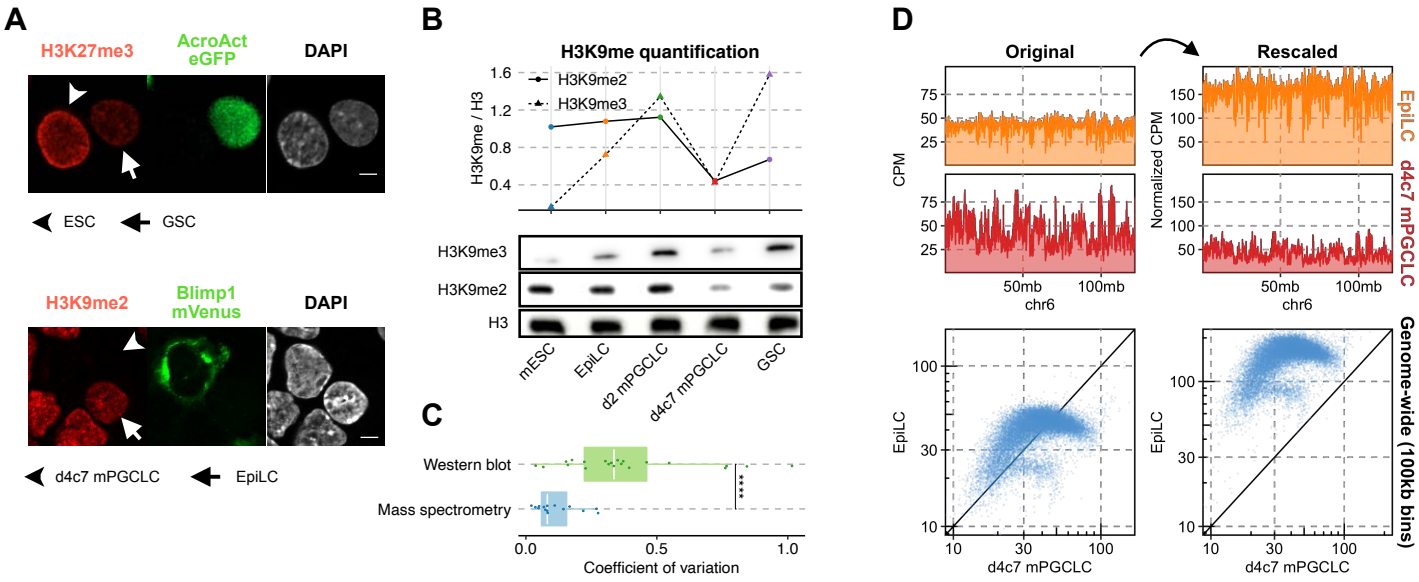

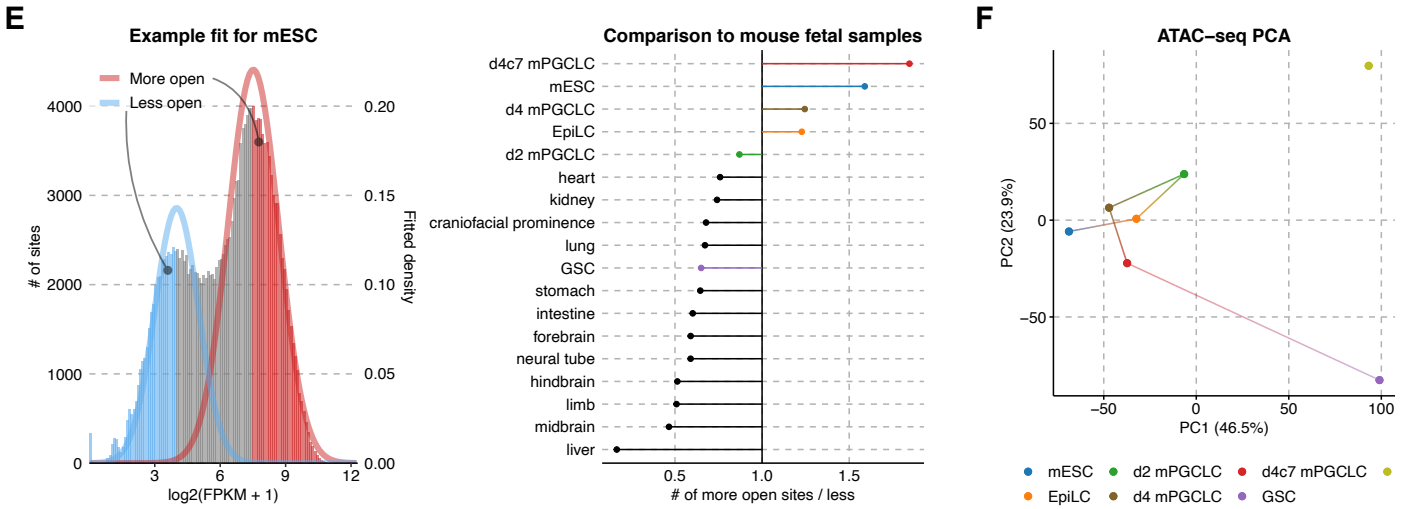

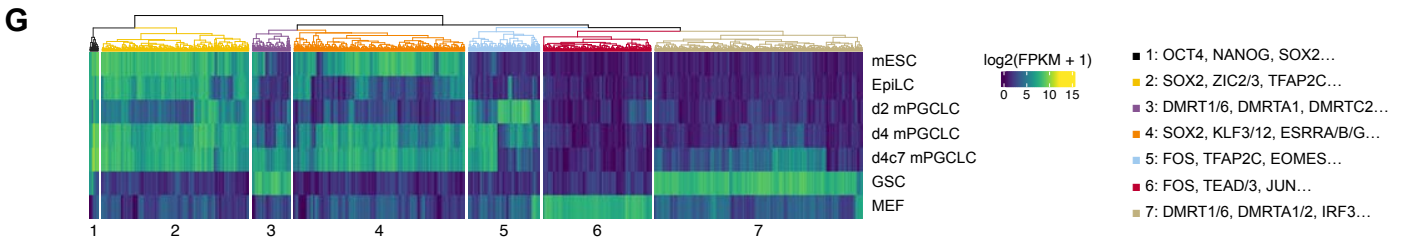

Nagano et al., figure EV3

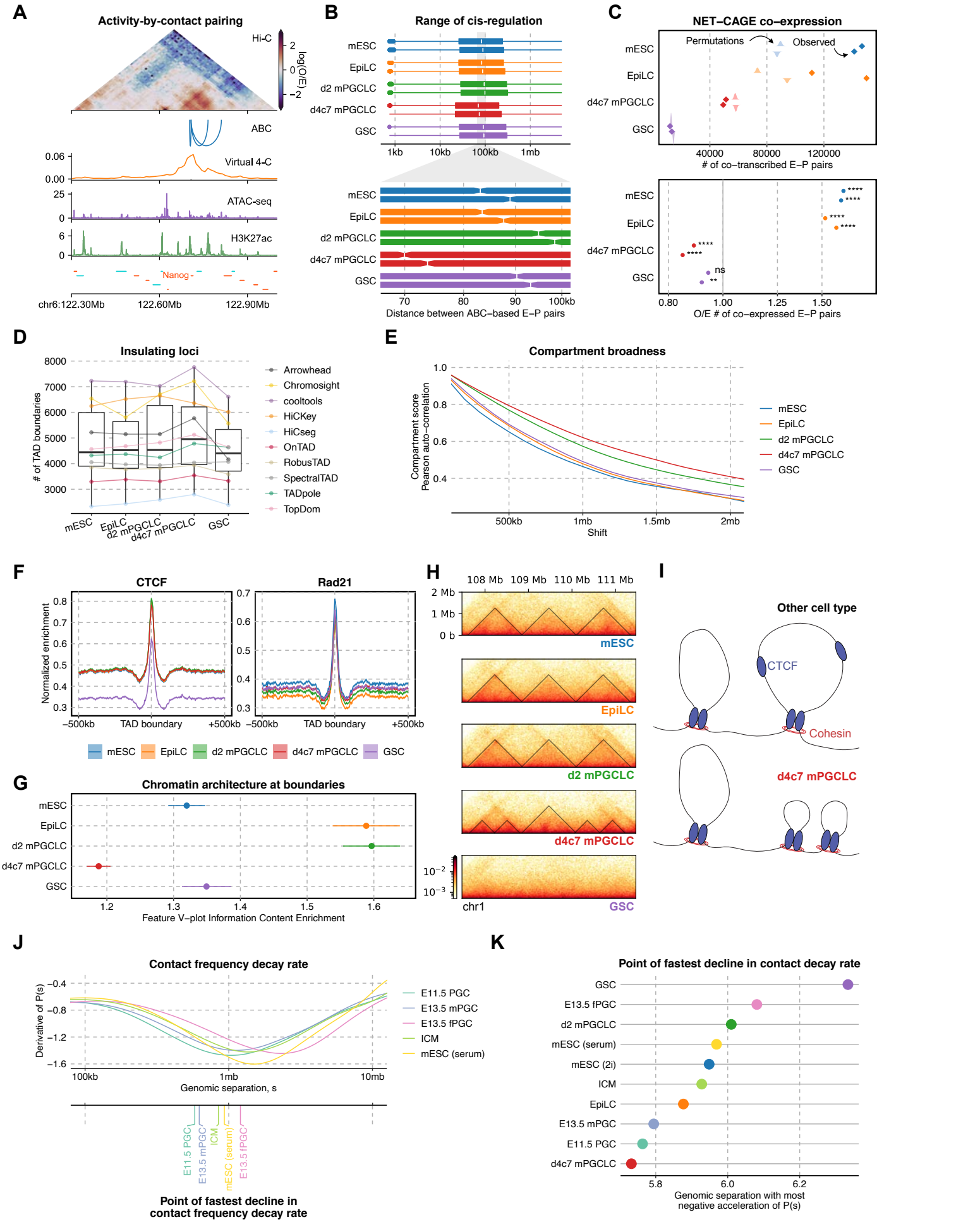

Nagano et al., figure EV4

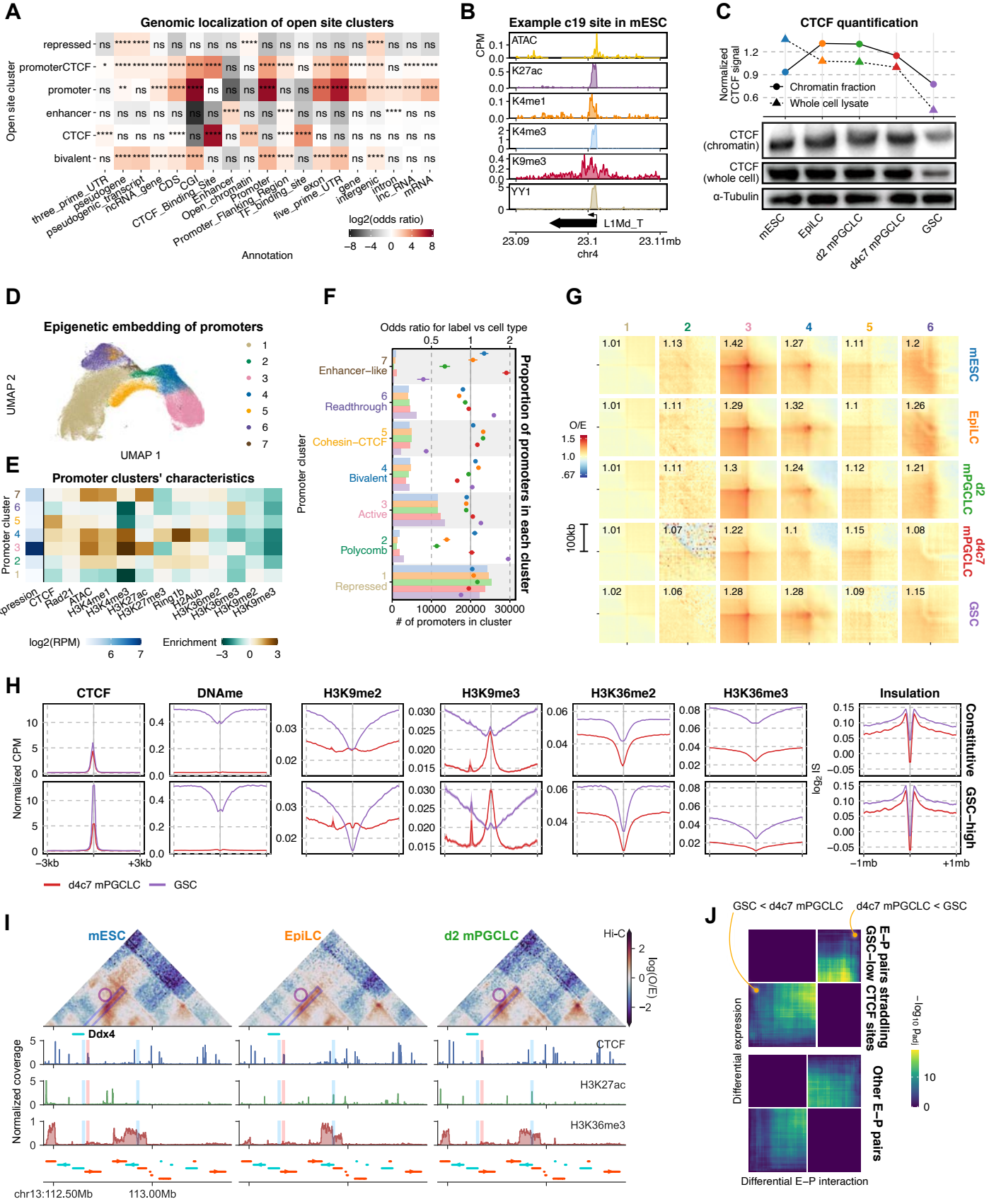

Nagano et al., figure EV5